

Transport and mixing by artificial cilia

Citation for published version (APA):

Baltussen, M. G. H. M. (2012). *Transport and mixing by artificial cilia*. [Phd Thesis 1 (Research TU/e / Graduation TU/e), Mechanical Engineering]. Technische Universiteit Eindhoven.
<https://doi.org/10.6100/IR724502>

DOI:

[10.6100/IR724502](https://doi.org/10.6100/IR724502)

Document status and date:

Published: 01/01/2012

Document Version:

Publisher's PDF, also known as Version of Record (includes final page, issue and volume numbers)

Please check the document version of this publication:

- A submitted manuscript is the version of the article upon submission and before peer-review. There can be important differences between the submitted version and the official published version of record. People interested in the research are advised to contact the author for the final version of the publication, or visit the DOI to the publisher's website.
- The final author version and the galley proof are versions of the publication after peer review.
- The final published version features the final layout of the paper including the volume, issue and page numbers.

[Link to publication](#)

General rights

Copyright and moral rights for the publications made accessible in the public portal are retained by the authors and/or other copyright owners and it is a condition of accessing publications that users recognise and abide by the legal requirements associated with these rights.

- Users may download and print one copy of any publication from the public portal for the purpose of private study or research.
- You may not further distribute the material or use it for any profit-making activity or commercial gain
- You may freely distribute the URL identifying the publication in the public portal.

If the publication is distributed under the terms of Article 25fa of the Dutch Copyright Act, indicated by the "Taverne" license above, please follow below link for the End User Agreement:

www.tue.nl/taverne

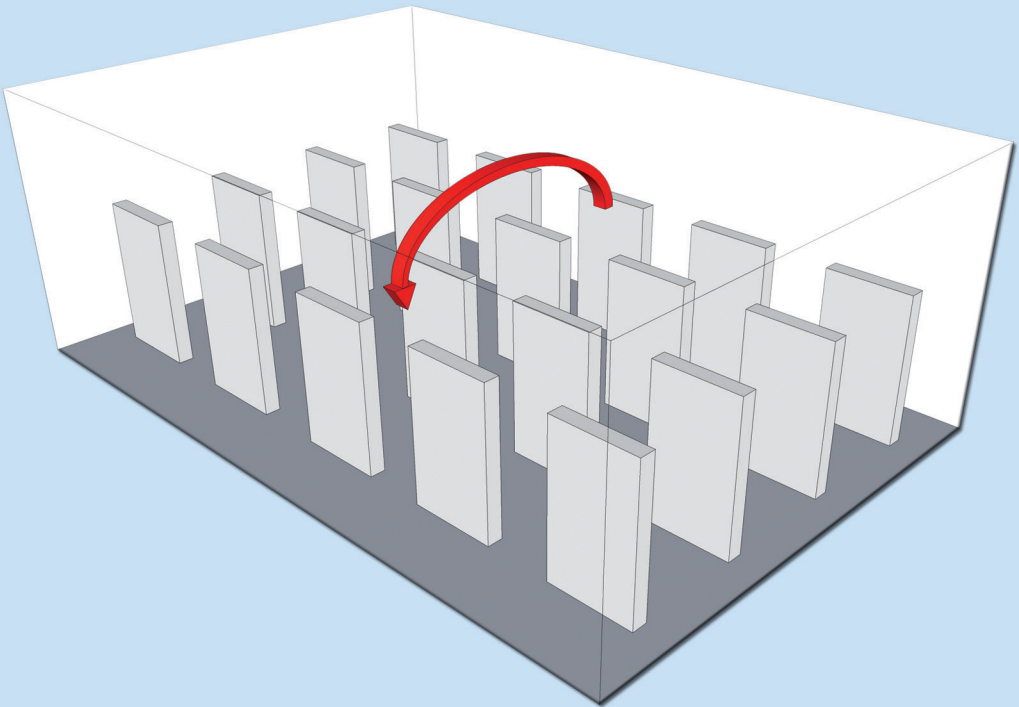
Take down policy

If you believe that this document breaches copyright please contact us at:

openaccess@tue.nl

providing details and we will investigate your claim.

Transport and Mixing by Artificial Cilia



Michiel Baltussen

Transport and Mixing by Artificial Cilia

M.G.H.M. Baltussen

CIP-DATA LIBRARY TECHNISCHE UNIVERSITEIT EINDHOVEN

Baltussen Michiel Gerardus Henricus Maria

Transport and mixing by artificial cilia.

Eindhoven University of Technology, 2012.

Proefschrift.

A catalogue record is available from the Eindhoven University of Technology library:

ISBN: 978-90-386-3085-4

This thesis was prepared with L^AT_EX2e

Cover design: Paul Verspaget (www.verspaget-bruinink.nl)

Printed by the Universiteitsdrukkerij Technische Universiteit Eindhoven, Eindhoven, The Netherlands

Transport and Mixing by Artificial Cilia

PROEFSCHRIFT

ter verkrijging van de graad van doctor aan de
Technische Universiteit Eindhoven, op gezag van de
rector magnificus, prof.dr.ir. C.J. van Duijn, voor een
commissie aangewezen door het College voor
Promoties in het openbaar te verdedigen
op donderdag 26 januari 2012 om 16.00 uur

door

Michiel Gerardus Henricus Maria Baltussen

geboren te Tilburg

Dit proefschrift is goedgekeurd door de promotor:

prof.dr.ir. J.M.J. den Toonder

Copromotoren:

prof.dr.ir. P.D. Anderson

en

dr.ir. M.A. Hulsen

Summary

Microfluidic analysis devices are becoming more common as a tool for clinical analysis. In these devices, fluid transport and mixing of multiple components are common tasks. A possible way of achieving these tasks can be found in nature, where small hairs, named cilia, are found on micro-organisms and surfaces. These hairs move the surrounding fluid, or move the micro-organism through the fluid. As in micro-fluidics, the generated flows are inertialess in general. By mimicking natural cilia, several successful microfluidic actuators for pumping and mixing have been developed recently [1–8].

In order to understand the working principles of these devices and improve their design, a numerical model is presented in this thesis. With this model, we study the fluid-structure interaction of the cilium with the surrounding fluid. Since cilia are very thin structures which show large deformations, a model which can cope with large deformations is required. We therefore choose to model the fluid on a fixed Eulerian grid and the solid on a moving Lagrangian grid. Initially we used a fictitious domain/Lagrange multiplier technique to couple both domains. Simulations showed however, that this technique is inaccurate near the moving interface between the fluid and the cilium. This inaccuracy stems from two causes, namely the fictitious fluid domain and the discretization of the Lagrange multiplier. The first cause is eliminated by replacing the fictitious domain with the eXtended Finite Element Method (XFEM). The second cause is removed by applying coupling in a weak manner, without the need for a Lagrange multiplier. This method gives accurate results for Newtonian, generalized Newtonian and viscoelastic fluids in combination with an elastic solid. The major advantages of this method are its accuracy and optimal convergence rates, without including problem dependent parameters.

In Chapter 4, the new numerical model is used to study the influence of the actuation frequency on the transport and mixing efficiency of one or two artificial cilia. It is shown that there exists a frequency for which the flow rate

is maximum. The reason for this maximum is that a fluid-structure interaction problem has an intrinsic time-scale. This makes the system frequency dependent, even if fluid and solid inertia are negligible. At the highest flow rate, the amount of displaced fluid per cycle is not the highest. So using the amount of displaced fluid as an objective may not lead to the largest flow rate possible in the system. For the mixing analysis two cilia are modeled, each having a different intrinsic time-scale. Both are actuated by the same actuation force, thus showing different motion. This leads to a phase difference between the two cilia, which has been shown to enhance mixing [9]. The mixing performance is measured by tracking a blob in time, which was initially placed in between the cilia. The stretch of this blob is a measure for the local mixing efficiency, and an exponential increase indicates chaotic mixing. A length stretch increase is observed in all cases. Changing the cilium thickness of one of the cilia has a clear beneficial effect on mixing. For mixing, the amount of fluid moved by the cilia is also important, as the mixing performance at low actuation frequency is much better than at high actuation frequency, where the movement of the cilia, and hence the induced flow, is less.

In order to perform simulations of artificial cilia in a non-Newtonian fluid, the numerical model proposed in Chapter 4 is extended in Chapter 6. In addition, a local mesh refinement scheme is developed in order to make accurate simulations within a shorter time-frame feasible. Both the mesh refinement scheme and the viscoelastic fluid-structure interaction scheme are tested, and shown to be stable and accurate.

This extended numerical model is used in Chapter 7 for the simulation of generalized Newtonian and viscoelastic fluid flow by artificial cilia. It is shown that by making use of the typical time-scale of the cilia system and the time-scale of the generalized Newtonian fluid, the net fluid flow of a generalized Newtonian fluid has a higher dependence on the actuation force than a Newtonian fluid.

In the final chapter conclusions and recommendations for future work are given.

Contents

Summary	i
1 Introduction	1
1.1 Challenges	3
1.2 Outline of the thesis	4
2 Modeling of flow generated by artificial cilia	5
2.1 Balance equations	7
2.2 Boundary, interface and initial conditions	11
2.3 Solid actuation	12
2.4 Dimensional analysis	14
2.5 Transport and mixing analysis	15
2.6 Conclusions	19
3 Inertial effects in a micromixer based on artificial cilia	21
3.1 Modelling	23
3.2 Numerical methods	25
3.3 Experiments	27
3.4 Results	28
3.5 Conclusions	32
4 XFEM and weak interface conditions	33
4.1 XFEM	35
4.2 Weakly-applied Dirichlet boundary conditions	41
4.3 Mesh moving schemes	47
4.4 Solution procedure	51
4.5 Test problems	53
4.6 Conclusions	58

5	Simulation of transport and mixing by artificial cilia: Newtonian fluid	63
5.1	Transport	64
5.2	Mixing	71
5.3	Chaotic cilium motion	77
5.4	Conclusions	79
6	Numerical tools for modeling of cilia driven flow of non-Newtonian fluids	81
6.1	Saliva rheology	82
6.2	Fluid-structure interaction with a non-Newtonian fluid	83
6.3	Validation	94
6.4	Conclusion	95
7	Simulation of transport by artificial cilia: non-Newtonian fluids	101
7.1	Transport of a generalized Newtonian fluid	101
7.2	Conclusions	107
8	Conclusions and recommendations	109
8.1	Recommendations	110
A	Time integration and linearization	121
A.1	Time integration	121
A.2	Linearization	122
B	Intersecting and Delaunay triangulation	123
B.1	Intersecting	123
B.2	Delaunay triangulation	125
C	Weakly-imposed Dirichlet boundary conditions for the Poisson equation	127
	Samenvatting	129
	Curriculum Vitae	133
	List of Publications	135

Chapter 1

Introduction

Since the invention of the transistor in 1923, the size of a transistor changed from several centimeters to tens of nanometers nowadays. This continuing miniaturization has led to the development of integrated circuits (IC's) with increasing complexity and, more importantly, increasing functionality. IC's allow people to communicate whenever and wherever they want, navigate through foreign countries and share information with the whole world at the blink of an eye. So the development of a technical device, the humble transistor, and its miniaturization, has changed not only today's technology but also our society.

By using production techniques developed for IC fabrication, a new branch of fluid dynamics was formed in the 1980's: microfluidics. It focuses on flow in channels with dimensions between 100 nanometer and 1 millimeter. By integrating more and more building blocks such as valves, patterned surfaces and moving structures, fluids could be manipulated.

In the early 1990's the idea of adding sensing and control capabilities to the microfluidic device, yielding a fully integrated system for chemical analysis, which became known as micro Total Analysis System (μ TAS) was introduced. Even a step further is the integration of processes not directly related to the chemical analysis itself, such as fluid storage, transport and mixing, which is known as a Lab-on-a-Chip (LOC) device. The main advantages of these LOC devices versus the conventional laboratory tests are the low amounts of fluids used [10], the reduction of hands-on-time of lab technicians, faster analysis times reached, small devices sizes reached and the possibility to parallelize tests. Some of the applications are DNA-amplification, bacteria and virus detection in water and artificial organs for drug testing [11]. Although most of these devices are still not commercially available they show the potential of a low-cost portable fluid testing device, which could change our lives quite significantly in the near future.

Although there is a lot of attention in the LOC community for miniaturizing the chemical analysis steps, the integration of the more basic task of

manipulating fluids [12–14] in a LOC device is still not trivial. Whereas one branch focusses on the manipulation of individual droplets [15], others focus on the motion of bulk fluids. Channels can be filled by capillary forces alone. Mixing of two fluids can be accomplished by diffusion if the lengthscales are small enough [16–18], inertial effects, a static mixer [19, 20] or accoustically [21]. Opposed to these static ways (static in the sence that only the fluid moves) of manipulating a fluid, are the active microfluidic actuators which move fluid around. One of the most common active actuators are valves [22], which are used for pumping and mixing, and can be pneumatically or electrically actuated. A new development in active microfluidic manipulation is formed by actuators inspired by nature, namely artificial cilia. Due to their resemblance with and derivation from the small hairs which nature uses for fluid transport on the sub-millimeter length-scale, these actuators are known as artificial cilia. The artificial cilia can either be actuated by electrostatic forces [1], magnetic forces [2, 4–8, 23, 24], light [25] or, in case of simplified biological system, biochemically [26].

Although these systems indeed generate flow and mix fluids, still many questions about the working principles behind cilia driven flow remain unanswered. The working principles can be revealed both experimentally as well as numerically. On the experimental side several different systems are used. Here we will model a system for electrostatic cilia as was developed by Den Toonder *et al.* [1], or a magnetic system as was developed and used in the European ARTIC project [4, 5]. In both cases polymer rectangular beams were produced. Since several other groups have been working on magnetically actuated cilia, information about their devices is also given.

Den Toonder *et al.* [1] used electrostatic actuation to actuate polyimide flaps of 100 μm length, 20 μm width and 2 μm thickness. These cilia were placed in a channel in groups of 100 (5 rows of 20 artificial cilia). By actuation at 100 Hz they showed improved mixing performance. Due to the high electric fields, silicone oil was used.

The magnetically actuated cilia which were developed in the ARTIC program [4, 5], have a length of 70 μm , width of 20 μm and thickness of 0.9 μm and consist of a rubber or hydrogel matrix filled with magnetic particles and yield velocities up to 2 mm s^{-1} [4].

In the group of prof. Superfine, artificial cilia have been developed which are polymer rods with magnetic particles inside [2, 7]. These rods are 25 μm long and have a radius of 700 nm. When actuated with a rotating magnetic field, these system achieve flows of 280 nl min^{-1} .

Vilfan *et al.* [23] used superparamagnetic particles, aligned them in trenches and applied a rotating magnetic field. The cilia had a length of 45 μm and a width of 5 μm . They obtained fluid velocities up to 4 $\mu\text{m s}^{-1}$ at an actuation frequency of 0.5 Hz.

The cilia made by Oh *et al.* [27] are 400 μm long, 75 μm wide and 10 μm thick. They are excited by a piezoactuator to beat at frequencies of 30 to 100

Hz in water, and velocities up to $180 \mu\text{m s}^{-1}$ were observed.

In addition to the fabrication and experimental investigation of artificial cilia, numerical models are developed, modelling the motion of the cilia and the surrounding fluid. In order to accurately compute the flow field near the cilia, the interaction of the moving cilium with the surrounding fluid has to be taken into account. This requires a fluid-structure interaction (fsi) model, which find many applications, such as modelling flow through hart valves [28] and blood vessels [29, 30], and modelling flow over objects such as wings or flags. Methods for solving these problems can be split into two groups: one where the discretised fluid grid moves along the solid [29–32] and one where this fluid grid is fixed [28, 33–35]. The first group of methods are known as Arbitrary Lagrange Euler (ALE) methods, and work fine for small deformation of the solid. For larger deformations the fluid grid becomes degenerated and a new grid has to be made in order to keep the method accurate. The second group does not have this disadvantage, so it can easily be used for problems having large solid deformations. The disadvantage of these methods is that it is difficult to accurately enforce the interface conditions in the fluid domain, since the interface is not nicely aligned with the fluid grid.

Using these models several research groups have investigated the flow generated by artificial cilia [9, 23, 36, 37]. In these models the cilia are modeled as an elastic beam or rod or as a string of magnetic particles and the fluid is either modeled as a drag force [23] or the complete flow field of a Newtonian fluid is computed in addition to the cilium motion.

The numerical model used by Khataavkar *et al.* and Khaderi *et al.* [9, 36, 37] is based on a fixed fluid grid, where a fictitious fluid body is present underneath the solid and the interface conditions are enforced with a Lagrange multiplier. This method is known as a fictitious domain Lagrange multiplier technique. It has the advantage that it is easy to use, since the fluid is computed on a fixed grid and the solid on a moving grid. The accuracy of the flow field near the cilia is not accurate however, due to the fictitious fluid domain and the used discretization of the Lagrange multiplier. This is also shown in recent work on the simulation of twin-screw extruders where this method has been used for describing the moving rotors [38]. Especially the errors in the velocity gradients are large. In order to perform more detailed transport and mixing studies in the vicinity of the cilia and possibly use non-Newtonian fluids, this method is probably not accurate enough. Especially for non-Newtonian fluids, large errors in the velocity gradients should be avoided, since this quickly leads to numerical instabilities.

1.1 Challenges

One of the major application areas of Lab-on-a-Chip devices is medical diagnostics. In medical diagnosis biological fluids such as blood, urine or saliva

are analyzed. As the artificial cilia are a building block of these LOC devices, they have to propel these fluids. Biological fluids are water based, but they may contain cells and large protein molecules; these fluids therefore show different rheological properties than the matrix fluid (water) and they are often heterogeneous at the micrometer length-scale. The current experimental and numerical studies almost always use a Newtonian fluid like water or a silicon oil as medium, however. In order to validate whether the results obtained in water can also be extrapolated to the more complex biological fluids, which may show non-Newtonian behavior, the influence of the rheology on flows generated by artificial cilia has to be investigated.

Since the current numerical models do not give accurate results near the cilia, a model has to be developed which accurately represents the flow field near the cilia. Some recent developments which enable the accurate capturing of discontinuities in flows (eXtendend Finite Element Method [35]) and other ways of imposing interface conditions (weak Dirichlet boundary conditions [39–41]) have opened up the road to the development of such a models.

Hence the objective of this thesis is the development of such a model and the application of this model to transport and mixing problems involving both Newtonian and non-Newtonian fluids. This requires an accurate representation of the velocity (gradients), in particular near the cilia surface.

1.2 Outline of the thesis

In this thesis a model is developed for the simulation of the mixing and pumping behavior of one or more cilia in a microfluidic device. In the following Chapter 2, the model domain, the governing equations and the boundary conditions are given and after a dimension analysis the important dimensionless groups are identified. In Chapter 3 the mixing performance of a microfluidic mixer which is electrostatically actuated is both simulated and measured. On the basis of the numerical results in this chapter, a more detailed numerical model for fluid-structure interaction is introduced in Chapter 4. With this model the transport and mixing performance of a system containing a Newtonian fluid is analyzed in Chapter 5. In the following chapter, the numerical model of Chapter 4 is expanded for non-Newtonian fluids. In this chapter the rheology of saliva is also assessed and appropriate models are selected. Using these models simulations of transport and mixing of a non-Newtonian fluid are performed and results are shown in Chapter 7. Finally conclusions and recommendations are given in Chapter 8.

Chapter 2

Modeling of flow generated by artificial cilia

In this chapter a model for flow that is induced by artificial cilia will be introduced. In the subsequent chapters, this model will be used as a starting point for developing numerical tools for studying this flow. Although the model is developed with this purpose in mind, it can be used for studying a broader class of problems in which fluid-structure interaction plays a role.

The most basic microfluidic device is a simple rectangular channel, through which one or more fluids are transported. By adding small structures, extra functions can be included. If for instance grooves are made in the channel walls or other passive structures are added, efficient mixing can be accomplished [19, 42]. These structures have that advantage that they are robust since there are no moving parts. On the other hand they have the disadvantage that they require an external pump which generates the flow over these structures. The fact that mixing cannot be switched on and off during flow can, in certain cases, also be an disadvantage. By adding active structures, the flow can be locally actuated however. With locally actuated flaps or rods, the artificial cilia, embedded pumps and mixers can be fabricated [1–4, 6, 7, 24]. The main difference between these transport and mixing devices is the configuration and direction of actuation of the cilia with respect to the channel direction. If the cilia are placed perpendicular to the channel and actuated in the channel direction, they can be used for pumping. If they are placed parallel to the channel and actuated perpendicular to the channel they can be used for mixing. In Figure 2.1 the pumping and mixing configurations along with the main fluid transport directions are shown. In Figure 2.2 the two-dimensional cross-section of the transport and mixing configuration is shown, again with the main flow direction generated by the cilia indicated. The only difference between modeling a pump and a mixer is the boundary condition at the left and

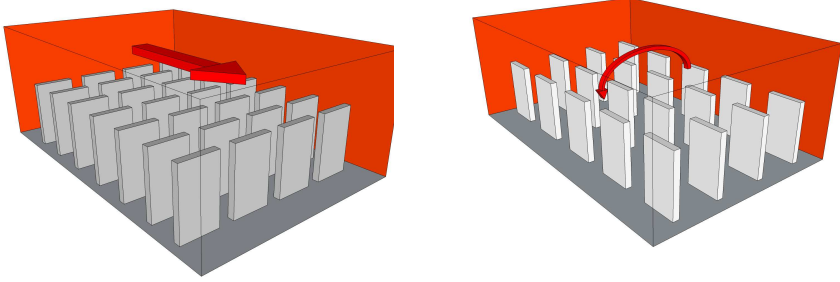


Figure 2.1: Left: The channel geometry in which the cilia are used for transport. The cilia are placed perpendicular to the channel and the generated flow direction, given by the red arrow, is in the channel direction. Right: The channel geometry in which the cilia are used for mixing multiple fluids. The cilia are placed in the channel direction and are actuated perpendicular to the channel direction. The generated flow is therefore also in the latter direction, and due the fixed walls causes a vortex, which is indicated by the red arrow.

right channel wall. Although the main flow direction in the mixing geometry is indicated by a vortex, this does not mean that the generation of such a vortex also leads to good mixing. For good mixing symmetry breaking is also required, which will be discussed in later chapters. In this thesis, we will only consider a two-dimensional model of artificial cilia. The main reason for that is, that computation times become excessively long for three dimensional calculations and may even be impossible with the numerical methods at hand. The 2D model is only valid if the cilia and channel are much longer in the third dimension than in the modeled two dimensions. Therefore the cilia have either to be very wide, or placed relatively close together thus forming one virtual cilium. With the devices of Den Toonder *et al.* [1] and Hussong *et al.* [4] in mind as typical systems this holds, since here arrays of closely packed cilia are placed in the channel.

The goal of this chapter is to develop a model of artificial cilia for the geometry given above. This model will then be used in subsequent chapters, where numerical tools for computing solutions to this model will be introduced and subsequently used in simulations.

This chapter is set up as follows: In Section 2.1 the equations of motion of the artificial cilia will be introduced. In Section 2.2 the interface conditions for fluid-structure interaction, contact problems and solid actuation are given, after which a scaling analysis is performed in Section 2.4. Finally, Section 2.5 will be on the quantification of the performance of the transport and mixing devices.

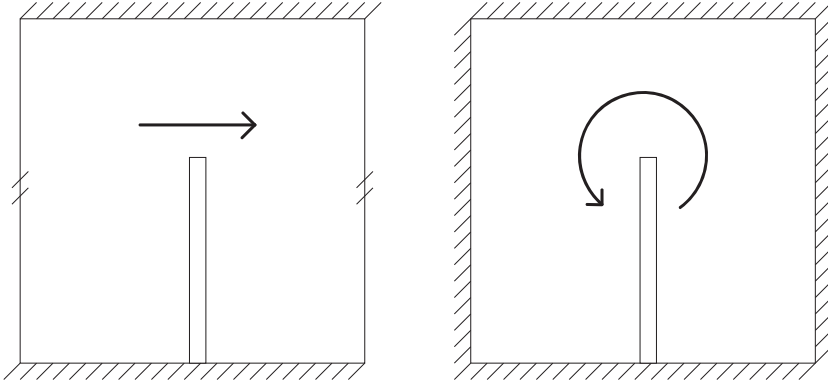


Figure 2.2: Left: The cross-section of Figure 2.1 (left), with only a single cilium. The top and bottom walls have no-slip boundary conditions and the channel is periodic in horizontal direction. Hence, the flow is mainly in horizontal direction, as indicated by the arrows. Right: A cross-section of the mixing configuration of Figure 2.1 (right), with only a single cilium. Here all walls have no-slip boundary conditions, thus the cilium generates a rotational flow, as given by the arrow.

2.1 Balance equations

We model a single cilium in a microfluidic channel as depicted in Figure 2.3, where the fluid domain is given by Ω_f , the solid domain by Ω_s and their mutual interface by Γ_{fs} . The height H and width W of the domain and the length L and thickness T_c of the cilium are still to be specified. Since both natural as well as artificial cilia are small, with lengths between $10 \mu\text{m}$ and 1mm , and thicknesses between tens and hundreds of nm 's, one could wonder whether they can be treated as homogeneous continua. The same question holds for the transported fluid, which is usually water, or a water-based biological fluid such as mucus or saliva. The polymer molecules in these solution have a size of about $10\text{-}50 \text{nm}$. The applicability of continuum mechanics can be answered by comparing the typical length-scales of the system to the typical structural and molecular length-scales. If the length-scales of the system are much larger than the latter length-scales, the system can be considered a homogeneous continuum, otherwise it should be treated either as a heterogeneous continuum or a group of molecules. For artificial cilia which are placed in a channel, the channel dimensions are also of importance and they are of the order of a millimeter for the height and width and several centimeters for the length. As indicated in the introduction, we are interested in the flow phenomena induced by a single cilium and a group of cilia. In addition to that, we are also interested in the local flow around a cilium. This means, that we have to model our domain

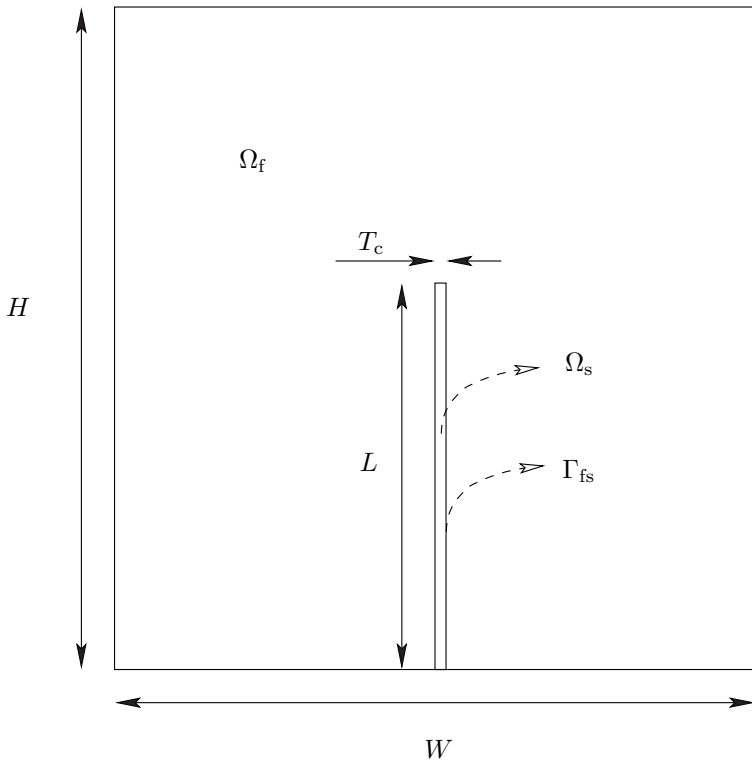


Figure 2.3: The model domain, with a channel of width W , and height H , the cilium length L and thickness T_c . The fluid domain Ω_f and solid domain Ω_s have the common interface Γ_{fs}

at a level which describes both effects at the channel size dimension, induced flow for example, as well as effects at the cilium thickness, local shear-rates for example. Since the length-scales in our system are much smaller than our macroscopic length-scales, the question can be raised whether the governing equations of motion used for describing motion at the macroscopic level are still valid for our system. In other words: Can we use continuum mechanics? The macroscopic equations are based on the assumption that a small change in size of the system under consideration should not alter the properties of the matter. We therefore compare specific sizes of the cilium, channel and fluid with the size of the molecules of which they are comprised. The artificial cilia under consideration are made out of a polymer material [1] which can be filled with magnetic particles [5], in case of magnetic actuation. The particles themselves have a radius of about 10 nm [5], and like to cluster. The size of these clusters is in the order of (50 – 100 nm) which is about the thickness of the

cilium. Hence their influence on mechanical and magnetic properties must be taken into account. The molecular weight of the polymers forming the matrix (Poly(butyl acrylate)) is $4 \cdot 10^4 \text{ g mol}^{-1}$, with a polydispersity index of about 3 [5]. This results in a radius of gyration in the order of tens of nanometers, hence for the thinnest cilia $T_c < 500 \text{ nm}$, there are still more than ten chains in the thickness. So the cilia can be considered as a continuum. The transported fluid is either water or a macromolecular solution in water. Since the size of a water molecule is 200 pm, and the cilium thickness is 500 nm, water can be considered a continuum in this case. For a macromolecular solution however, the size of a molecule (Xanthan gum) is 350 nm [43] or 150-250 nm for corn starch [44]. Which is comparable to the thickness of the cilium, so for the thinnest cilia the macromolecular solution cannot be treated as a continuum.

From the analysis of the previous paragraphs it is clear that we may consider the modeled system as a continuum and use the macroscopic equations of motion, except for very thin cilia where the thickness is of the same order as the size of the polymers comprising them or surrounding them. Since we want to avoid non-continuum mechanical modeling, we will only use cilia with a thickness larger than 500nm. Now it is established that the cilium and fluid domain both can be considered homogeneous continua, for these choice of the problem dimensions, the reference frame has to be chosen. Here we choose to model the fluid domain in a fixed Eulerian framework and the solid in a moving Lagrangian frame, which is most appropriate for the individual problems. If fluid and solid domains are coupled however this causes some difficulties which will be identified and overcome later in this chapter. The governing equations of motion consist of the conservation equations of mass and momentum, the boundary and initial conditions and the constitutive relations for fluid and solid stress. Since the boundary and initial conditions are problem dependent, they will be stated for each problem separately. We will model this problem isothermally, since no external heat sources or sinks are present and the internal heat source are either absent (reactions) or considered to be low (mechanical dissipation). Since we consider the flow of a water based fluid at relatively low pressures, we will assume the fluid to be incompressible. We will also assume the solid to be incompressible, and initially stress-free. After these assumptions the conservation and constitutive relations are given by:

Fluid:

$$\nabla \cdot \mathbf{u} = 0 \quad \text{in } \Omega_f, \quad (2.1)$$

$$\rho_f \left(\frac{\partial \mathbf{u}}{\partial t} + \mathbf{u} \cdot \nabla \mathbf{u} \right) = \nabla \cdot \boldsymbol{\sigma}_f + \mathbf{f}_f \quad \text{in } \Omega_f, \quad (2.2)$$

Solid:

$$\det(\mathbf{F}) - 1 = 0 \quad \text{in } \Omega_s, \quad (2.3)$$

$$\rho_s \frac{D^2 \mathbf{d}}{Dt^2} = \nabla \cdot \boldsymbol{\sigma}_s + \mathbf{f}_s \quad \text{in } \Omega_s, \quad (2.4)$$

where \mathbf{u} is the fluid velocity, ρ_f is the fluid density, $\boldsymbol{\sigma}_f$ is the Cauchy stress in the fluid, \mathbf{f}_f are body forces on the fluid, \mathbf{F} is the deformation gradient tensor, ρ_s is the density of the solid, \mathbf{d} is the displacement of the solid, $\boldsymbol{\sigma}_s$ is the Cauchy stress in the solid, \mathbf{f}_s are the body forces on the solid. The interface conditions coupling the two domains Ω_f and Ω_s at Γ_{fs} will be given in Subsection 2.2.1.

2.1.1 Constitutive Relations

In the momentum equations of the fluid and solid and in the interface condition for fluid-structure interaction, the fluid and solid stress still need to be specified. For viscous fluids the stress is related to the rate of deformation, whilst for solids it is related to the deformation. The most simple model for fluids is the Newtonian model, which is given by:

$$\boldsymbol{\sigma}_f = 2\eta\mathbf{D} - p_f\mathbf{I}, \quad (2.5)$$

with η the viscosity, \mathbf{D} the rate-of-deformation tensor and p_f the fluid pressure. If the fluid is in-elastic non-Newtonian (*e.g.* the viscosity is not constant), the constitutive relation for the fluid stress is often described by a generalized Newtonian fluid model, for example the Carreau model:

$$\begin{aligned} \boldsymbol{\sigma}_f &= 2\eta(\dot{\gamma})\mathbf{D} - p_f\mathbf{I}, \\ \eta(\dot{\gamma}) &= \eta_\infty + \frac{\eta_0 - \eta_\infty}{\sqrt{(1 + (\lambda\dot{\gamma})^{(1-n)/2})^2}}, \end{aligned} \quad (2.6)$$

where η_0 and η_∞ are the viscosities at zero and infinite shear rate, λ is the timescale at which the viscosity starts to decrease with slope $1 - n$. The generalized Newtonian model describes the shear thinning behaviour, which is the steady decrease of the steady state shear viscosity above a certain shear rate. This model does not show stress build up and relaxation, which are common to many elastic non-Newtonian fluids.

Apart from flows dominated by steady shear, the generalized Newtonian model differs from the behaviour of real non-Newtonian fluids. Hence, a more elaborate model is needed in these cases. Since we are interested in the behavior of biological non-Newtonian fluids, which are often macromolecular solutions, the Oldroyd-B model is used:

$$\begin{aligned} \boldsymbol{\sigma}_f &= 2\eta_\infty\mathbf{D} + \boldsymbol{\tau} - p_f\mathbf{I}, \\ \boldsymbol{\tau} &= G(\mathbf{c} - \mathbf{I}), \end{aligned} \quad (2.7)$$

$$\lambda_{OB} \overset{\nabla}{\mathbf{c}} + \mathbf{c} - \mathbf{I} = \mathbf{0} \quad (2.8)$$

where η_∞ is the solvent viscosity, $\boldsymbol{\tau}$ is the extra stress tensor, G is the modulus of the viscoelastic fluid and \mathbf{c} the conformation tensor giving the average stretch

and orientation of the polymer molecules. The upper-convected time derivative of \mathbf{c} is defined as: $\overset{\nabla}{\mathbf{c}} = \frac{\partial \mathbf{c}}{\partial t} + \mathbf{u} \cdot \nabla \mathbf{c} - \mathbf{L} \cdot \mathbf{c} - \mathbf{c} \cdot \mathbf{L}^T$ and λ_{OB} is the relaxation time. Here also a solvent is included by adding the Newtonian fluid stress of the solvent with viscosity η_{∞} . Another widely used viscoelastic model is the Giesekus model, for which the evolution equation of the conformation tensor is given by:

$$\lambda_G \overset{\nabla}{\mathbf{c}} + (\mathbf{c} - \mathbf{I}) + \alpha (\mathbf{c} - \mathbf{I})^2 = \mathbf{0}, \quad (2.9)$$

where α is a parameter describing the anisotropic friction between a polymer and the surrounding, and λ_G is a relaxation time, similar to λ_{OB} .

Since the cilium is basically a slender beam, with bending as the main mode of deformation, a simple elastic model suffices to describe this. Here we use the Mooney-Rivlin model:

$$\boldsymbol{\sigma}_s = G_{sI} (\mathbf{B} - \mathbf{I}) G_{sII} (\mathbf{B}^{-1} - \mathbf{I}) - p_s \mathbf{I}, \quad (2.10)$$

where G_{sI} and G_{sII} are the moduli of the solid, $\mathbf{B} = \mathbf{F} \cdot \mathbf{F}^T$ is the Finger tensor, or left Cauchy-Green deformation tensor, $\mathbf{B}^{-1} = \mathbf{F}^{-T} \cdot \mathbf{F}^{-1}$ and p_s is the solid pressure. In many simulations $G_{sII} = 0$ and the Mooney-Rivlin model reduces to the neo-Hookean model. In cases where large compressive stresses are encountered, the Mooney-Rivlin model is used, since it shows a increasing stiffness in compression, which stabilizes the numerical simulations.

2.2 Boundary, interface and initial conditions

At the boundaries of the fluid and solid domain boundary conditions have to be specified. At the fluid-structure interface these boundary conditions couple both domains. Since both the fluid and solid momentum equation contain time-dependent terms, initial conditions have to be specified. As will be shown, the interface conditions for fluid-structure interaction will also give rise to a time-dependent term, which also requires an initial condition for the displacement of the solid. Since the cilium is connected to the bottom of the channel, the possibility exists that the free end will touch the bottom of the channel. This means that solid-rigid contact takes place and this has to be modeled accordingly.

2.2.1 Interface conditions

At the fluid-solid interface Γ_{fs} , no-slip boundary conditions are assumed. This means that all components of the velocity and traction are continuous over the interface, which results in the following conditions:

$$\mathbf{u} - \frac{\partial \mathbf{d}}{\partial t} = \mathbf{0} \quad \text{on } \Gamma_{\text{fs}}, \quad (2.11)$$

$$\mathbf{n}_f \cdot \boldsymbol{\sigma}_f + \mathbf{n}_s \cdot \boldsymbol{\sigma}_s = \mathbf{0} \quad \text{on } \Gamma_{\text{fs}}, \quad (2.12)$$

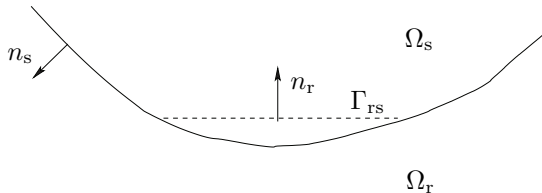


Figure 2.4: Contact of the cilium Ω_s with the rigid wall Ω_r on the contact line Γ_{rs} .

where the normals \mathbf{n}_f and \mathbf{n}_s are pointing outward of the respective body, hence $\mathbf{n}_s = -\mathbf{n}_f$. The first interface condition (2.11) is a kinematic interface condition, while the second (2.12) is a dynamic interface condition. Both can be adapted easily to allow for slip between the two materials.

2.2.2 Solid rigid contact

For certain initial shapes of the cilia and types of actuation, the cilia can contact the wall of the channel. The solid body Ω_s comes into contact with the rigid body Ω_r on the common boundary Γ_{rs} , see Figure 2.4. The position of a material point in the solid with respect to the rigid boundary is defined as δ . Assuming no-slip conditions at contact, the equations which hold at contact are:

$$\delta \cdot \mathbf{n}_r \leq 0, \quad (2.13)$$

$$\boldsymbol{\lambda}_s \cdot \mathbf{n}_r \geq 0, \quad (2.14)$$

$$\delta \cdot \boldsymbol{\lambda}_s = 0, \quad (2.15)$$

where \mathbf{n}_r is the normal pointing outward of the rigid body and $\boldsymbol{\lambda}_s$ is the contact force. These two inequalities and one equality are known as the Karush-Kuhn-Tucker (KKT) conditions [45].

2.3 Solid actuation

The cilia are actuated by an external magnetic field or by electrostatic actuation. Magnetically actuated cilia are studied by Khaderi *et al.* [36, 37], where either permanently magnetic or super-paramagnetic particles are embedded in the polymer matrix which comprises the cilium. Other research groups are also studying magnetic actuation, mainly because it circumvents the largest drawback of electrostatic actuation: most fluids are affected by the electrostatic field because they are conductive, which may even lead to deterioration of molecules and cells present in the fluid (*e.g.* electrophoretic effects). On the other hand the conductivity of the fluid will screen the electric field, leading

to decreased electrostatic forces. Most biological fluids do not, or only slightly, interact with a magnetic field however. The main drawback of magnetic actuation is the fact that it is a volume force, while the fluid drag is a surface force. Thus upon miniaturization, scaling is less favorable to magnetic actuation. Since the electrostatic force is also a surface force, it scales the same as the fluid drag. Hence from this respect it is favorable over the magnetic force. We will consider both electrostatically and magnetically actuated cilia. In case of magnetic actuation, the magnetic forces and moments on the cilium are modeled as a body force.

2.3.1 Electrostatic actuation

The artificial cilia fabricated by den Toonder *et al.* [1], were actuated electrostatically. Since we want to study the flow in this device in the next chapter, an accurate description of the actuation is required. For this the governing equations for the electric field have to be introduced as well as corresponding interface conditions. The slowly varying electric field in $\Omega = \Omega_f \cup \Omega_s$ is given by the Maxwell equations:

$$\nabla \times \mathbf{E} = 0 \quad \text{in } \Omega, \quad (2.16)$$

$$\nabla \cdot \mathbf{D}_e = 0 \quad \text{in } \Omega, \quad (2.17)$$

where \mathbf{E} is the electric field, and \mathbf{D}_e the electric displacement, given for a linear isotropic dielectric medium by the constitutive relation $\mathbf{D}_e = \epsilon \mathbf{E}$, where ϵ is the dielectric constant. The electric field is solely determined by an electric field potential ϕ , the electric field can be written as: $\mathbf{E} = -\nabla \phi$, which satisfies Equation (2.16). Thus the problem can be reduced to:

$$-\nabla \cdot (\epsilon \nabla \phi) = 0 \quad \text{in } \Omega. \quad (2.18)$$

This problem has the following boundary conditions:

$$\phi = \phi_D \quad \text{on } \Gamma_D, \quad (2.19)$$

$$\mathbf{n} \cdot \mathbf{D}_e = \epsilon \frac{\partial \phi}{\partial \mathbf{n}} = \mathbf{j}_N \quad \text{on } \Gamma_N, \quad (2.20)$$

where ϕ_D is value for the Dirichlet boundary condition on Γ_D , \mathbf{n} is the outward facing normal of Ω , \mathbf{j}_N is the value for the Neumann boundary condition on Γ_N and $\Gamma = \Gamma_D \cup \Gamma_N$.

The stress in a volume of material due to the applied electric field is given by the Maxwell stress tensor [46]:

$$\boldsymbol{\sigma}_M = \epsilon \left(\mathbf{E}\mathbf{E} - \frac{\mathbf{E} \cdot \mathbf{E}}{2} \mathbf{I} \right). \quad (2.21)$$

Since the cilium and the fluid are two different dielectric materials, the dielectric constant ϵ differs and at the interface Γ_{fs} the following conditions hold:

$$\phi_f = \phi_s, \quad (2.22)$$

$$\mathbf{n}_f \cdot \mathbf{D}_{e,f} = -\mathbf{n}_s \cdot \mathbf{D}_{e,s}. \quad (2.23)$$

In case the cilium is approximated as a perfect conductor, with $\epsilon_s = \infty \text{N V}^{-2}$, and taking into account the requirement that \mathbf{D}_e remains finite, the electric field $\mathbf{E}_s = \mathbf{0}$. If the fluid is a dielectric, the electrostatic traction vector on the solid at Γ_{fs} can be written as:

$$\mathbf{t}_M = \mathbf{n}_s \cdot (\boldsymbol{\sigma}_{M,f} - \boldsymbol{\sigma}_{M,s}) = -\mathbf{n}_f \cdot \boldsymbol{\sigma}_{M,f} = -\mathbf{n}_f \cdot \left[\epsilon_f \left(\mathbf{E}_f \mathbf{E}_f - \frac{\mathbf{E}_f \cdot \mathbf{E}_f}{2} \mathbf{I} \right) \right]. \quad (2.24)$$

Thus the electrostatic traction at the conductor is solely determined by the electric field in and the permittivity of the fluid. Note that this electrostatic traction creates a jump between the two traction vectors of the fluid and the solid, thus yielding an adapted dynamic interface Equation (2.12) condition:

$$\mathbf{n}_f \cdot \boldsymbol{\sigma}_f + \mathbf{n}_s \cdot \boldsymbol{\sigma}_s = \mathbf{t}_M \quad \text{on } \Gamma_{fs}, \quad (2.25)$$

which can be used instead of Equation (2.12).

2.3.2 Initial conditions

The momentum equations of the solid and fluid contain time dependent terms, hence initial conditions have to be specified. In case a viscoelastic model is used, initial conditions have to be specified too. In all cases the fluid and solid are considered to be at rest, and the conformation tensor to be in equilibrium initially:

$$\mathbf{u}(\mathbf{x}, t = t_0) = \mathbf{0} \quad \forall \mathbf{x} \in \Omega_f, \quad (2.26)$$

$$\mathbf{d}(\mathbf{x}, t = t_0) = \mathbf{0} \quad \forall \mathbf{x} \in \Omega_s, \quad (2.27)$$

$$\mathbf{c}(\mathbf{x}, t = t_0) = \mathbf{I} \quad \forall \mathbf{x} \in \Omega_f. \quad (2.28)$$

2.4 Dimensional analysis

In this section we rewrite the governing equations of motion in a dimensionless form, which reveals the dimensionless groups governing the problem. Since the cilia are driven by a body force, the displacement and the velocity are not known a priori, as they are part of the solution. We therefore also give expressions for their dimension full form. The fluid is considered to be Newtonian for the moment. The variables are scaled as follows, where (\cdot) denotes the

dimensionless variable: $\nabla = \frac{1}{L}\hat{\nabla}$, $\mathbf{u} = U\hat{\mathbf{u}}$, $\mathbf{d} = D\hat{\mathbf{d}}$, $p_f = \frac{\eta U}{L}\hat{p}_f$, $p_s = \frac{GD}{L}\hat{p}_s$, $\mathbf{f} = f_0\hat{\mathbf{f}}$. Here U is the typical velocity, D the typical displacement and f_0 the typical body force on the cilium. The modulus of the solid $G_s = G_{sI} + G_{sII}$. Omitting all $\hat{\cdot}$ for readability, we obtain the following dimensionless form of the governing equations:

Fluid:

$$\nabla \cdot \mathbf{u} = 0 \quad \text{in } \Omega_f, \quad (2.29)$$

$$\text{St} \frac{\partial \mathbf{u}}{\partial t} + \text{Re} \mathbf{u} \cdot \nabla \mathbf{u} = 2\nabla \cdot \mathbf{D} - \nabla p_f \quad \text{in } \Omega_f, \quad (2.30)$$

Solid:

$$\det(\mathbf{F}) = 1 \quad \text{in } \Omega_s, \quad (2.31)$$

$$\text{El} \frac{\partial^2 \mathbf{d}}{\partial t^2} = \nabla \cdot (\mathbf{B} - \mathbf{I}) - \nabla p_s + \text{R}_1 \mathbf{f} \quad \text{in } \Omega_s, \quad (2.32)$$

Interface conditions:

$$\text{R}_2 \mathbf{u} - \frac{\partial \mathbf{d}}{\partial t} = \mathbf{0} \quad \text{on } \Gamma_{fs}, \quad (2.33)$$

$$\text{R}_3 \mathbf{n}_f \cdot (\mathbf{D} - p_f \mathbf{I}) + \mathbf{n}_s \cdot (\mathbf{B} - \mathbf{I} - p_s \mathbf{I}) = \mathbf{0} \quad \text{on } \Gamma_{fs}, \quad (2.34)$$

in which a number of dimensionless groups appear, which are listed in Table 2.1. Since the interface conditions always balance, the last two groups must always be unity, resulting in a time-scale $t_3 = \frac{\eta}{G_s}$. Note that even if inertia of both fluid and solid are unimportant the system is time-dependent with a typical time-scale t_3 . Although the slenderness of the cilium certainly plays a role in the deformation it is not included in the scaling.

2.5 Transport and mixing analysis

Artificial cilia are used for transport and mixing in microfluidic devices. In order to show how different fluids and cilium properties change the transport and mixing in these devices, it is important to quantify transport and mixing performance.

If the cilia are used for the transport of fluid the most obvious variable to compare with, is the average flow rate, which is defined as the total flow during a cycle divided by the cycle time. The higher the average flow rate the better the cilia perform.

In mixing, the performance of a device can be measured in different ways. In order to explain them, a short introduction to mixing is necessary.

Two fluids which have a common interface, interact with each other at the interface via diffusion. The transport is then given by the instationary

Table 2.1: The dimensionless groups in a fluid-structure interaction problem.

Re	$\frac{\rho_f U L}{\eta}$	The Reynolds number, which is the ratio between the convective inertial and viscous forces.
St	$\frac{\rho_f L^2}{\eta t_1}$	The Stokes number defining the ratio between instantaneous inertial forces and viscous forces. t_1 is either an actuation time-scale, or $t_1 = \frac{L}{U}$, in which case the Stokes number is equal to the Reynolds number.
El	$\frac{\rho_s L^2}{G_s t_2^2}$	The elasticity number, giving the ratio between inertial and elastic forces in the solid. t_2 is either the actuation time-scale or $t_2 = \sqrt{\frac{\rho_s L^2}{G}}$, in which case $\text{El} = 1$.
R_1	$\frac{f_0 L^2}{G_s D}$	The ratio between the applied force and the elastic force.
R_2	$\frac{U t_3}{D}$	The ratio between the fluid velocity and the solid velocity at the interface, where t_3 is the typical time-scale of the system, which is yet to be determined.
R_3	$\frac{\eta U}{G_s D}$	The ratio between the fluid and solid traction at the interface.

convection diffusion equation:

$$\frac{\partial c}{\partial t} + \mathbf{u} \cdot \nabla c = k \nabla^2 c, \quad (2.35)$$

where c is the concentration of one of the fluids, t is time, \mathbf{u} is the external velocity field and k is the diffusion constant. By scaling this equation with $c = c_0 \hat{c}$, $t = t_{\text{mix}} \hat{t}$, $\mathbf{u} = U \hat{\mathbf{u}}$ and $\nabla = \frac{1}{L_{\text{int}}} \hat{\nabla}$, where L_{int} is the distance between two interfaces,

$$\text{St} \frac{\partial \hat{c}}{\partial \hat{t}} + \text{Pe} \hat{\mathbf{u}} \cdot \hat{\nabla} \hat{c} = \nabla^2 \hat{c}, \quad (2.36)$$

two dimensionless groups appear: The Strouhal number $\text{St} = \frac{L_{\text{int}}^2}{k t_{\text{mix}}^2}$ and the Péclet number $\text{Pe} = \frac{U L_{\text{int}}}{k}$, see Equation 2.36. In this equation the hats are omitted to increase readability. In case there is no convection, $\text{Pe} = 0$, the typical timescale becomes: $t_{\text{mix}} = \frac{L_{\text{int}}^2}{k}$. So for large L_{int} and low k it takes very long for diffusion to mix the two fluids. Since the diffusion constant k cannot be changed in general, the only option to decrease t_{mix} is to decrease L_{int} . This can be achieved by setting up a flow in which alternative layers of each fluid are formed, thus decreasing L_{int} . In the other limit where $\text{Pe} = \infty$, the mixing is completely convection dominated, and the molecules to be mixed move affinely with the flow. Hence the evolution of the position of a material point \mathbf{x} is given by $\frac{d\mathbf{x}}{dt} = \mathbf{u}$, which means that the mixing time becomes $t_{\text{mix}} = \frac{L_{\text{int}}}{U}$. So for high Péclet numbers, the mixing time scales linearly with the interface thickness, whereas for low Péclet numbers it scales quadratically. For convection dominated mixing problems, the mixing performance can directly be quantified by integrating $\frac{d\mathbf{x}}{dt} = \mathbf{u}$ for a given initial condition $x(t=0) = x_0$ and a given period of time. By measuring the initial distance l_0 between two points at $t=0$ and at the end l_1 of the given period, the stretch is defined as $\lambda = \frac{l_1}{l_0}$. Instead of defining a global average stretch, we compute the local stretch by placing a drop in the flow and recording its circumferential length in time. The rate at which the interface length increases quantifies the effectiveness of the flow for mixing. If the mixing length increases exponentially, as for instance in elongational flow, the mixing is said to be optimal. The main disadvantage of this mixing measure is the fact that it depends on the initial placement of the drop, so it is a local mixing measure. An example of the initial drop and its shape after flow is applied is shown in Figure 2.5.

In order to ascertain whether mixing occurs in every part of the domain, a more global mixing measure has to be used. One is the intensity of segregation,

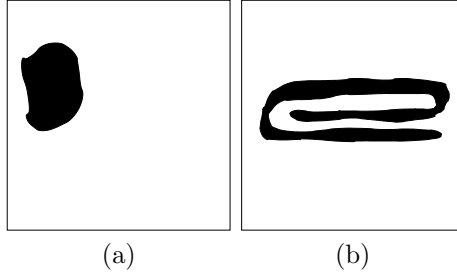


Figure 2.5: The shape of the drop before flow is applied (a) and after flow is applied (b). It is clear that the circumferential length has increased due to flow.

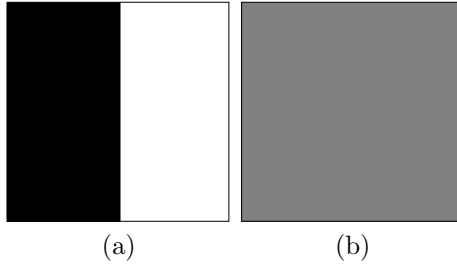


Figure 2.6: The intensity of segregation \mathcal{I} for two different situations: (a) $\mathcal{I} = 1$ and (b) $\mathcal{I} = 0$.

which is the second order moment of the concentration distribution [47]:

$$\mathcal{I} = \frac{\int_{\Omega_f} (c(\mathbf{x}) - \bar{c})^2 dx}{\int_{\Omega_f} \bar{c}(1 - \bar{c}) dx}, \quad (2.37)$$

where \mathcal{I} is the intensity of segregation, $c(\mathbf{x})$ is the concentration in \mathbf{x} and \bar{c} is the average concentration defined as $\bar{c} = \frac{\int_{\Omega_f} c(\mathbf{x}) dx}{\int_{\Omega_f} dx}$. If $\mathcal{I} = 1$ the mixture is completely segregated, see Figure 2.6(a), and $\mathcal{I} = 0$ means a fully homogeneous mixture, see Figure 2.6(b). It is clear that it quantifies mixing globally, since it requires averaging over the whole domain, so the whole domain contributes to \mathcal{I} .

Mixing can also be quantified by the Shannon entropy of mixing [48], or better the rate at which this mixing entropy changes. In order to compute both of them, the domain is subdivided into a number of cells n_c and particles are tracked under influence of the flow. At each time-step the number of particles n_i in cell i is counted and stored. The discrete entropy of mixing \mathcal{S} and its

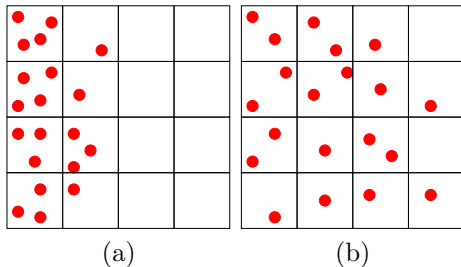


Figure 2.7: The Shannon mixing entropy \mathcal{S} for two different situations: (a) $\mathcal{S} = \text{low}$ and (b) $\mathcal{S} = \text{high}$.

increase rate κ_S are then computed from this information as follows:

$$\mathcal{S} = \frac{-1}{n_{\text{part}}} \sum_{i=1}^{n_c} n_i \log \frac{n_i}{n_{\text{part}}}, \quad (2.38)$$

$$\kappa_S = \frac{\mathcal{S} - \mathcal{S}_0}{\mathcal{S}_{\text{max}} - \mathcal{S}_0}, \quad (2.39)$$

where n_{part} is the total number of particles in the entire domain, \mathcal{S}_0 is the initial mixing entropy and \mathcal{S}_{max} is the maximal mixing entropy. An illustration of the distribution of particles in cells for a low (Figure 2.7(a)) and high (Figure 2.7(b)) mixing entropy is given in Figure 2.7.

The Shannon entropy is cell size dependent, hence the mixing effectiveness can be assessed on different length-scales by changing the amount of cells. Both \mathcal{S} and κ_S are global mixing measures, since \mathcal{S} is an average over all cells.

2.6 Conclusions

We model the flow induced by artificial cilia by using continuum mechanics. Two different cases will be studied: A transport geometry where the cilia are actuated in the direction of the channel and a mixing geometry in which the cilia are actuated perpendicular to the channel direction. The kinematic and dynamic interface conditions coupling the solid cilium domain to the fluid domain are also determined. After scaling the equations of motion the important dimensionless groups are defined. The actuation of the cilia is also treated and performance measures for the transport and mixing geometries are defined as well. In the process of deriving the model the following important observations were made:

- Both fluid and artificial cilium can be treated as an homogeneous continuum, except when the cilia contain magnetic particles and are thinner than 50 nm.

- The only difference in the transport and mixing geometry is the boundary condition for the fluid, the rest is the same.
- Every fluid-structure interaction problem, involving a non-rigid solid, is time dependent, since the fluid velocity is coupled to the solid deformation, which yields a typical time scale t_3 .
- In a transport geometry the net flow per cycle is our performance measure, in a mixing geometry it can either be the length stretch of a drop, the intensity of segregation or the entropy increase rate.

Chapter 3

Inertial effects in a micromixer based on artificial cilia ¹

In this chapter the flow in a microfluidic mixer is studied with the models presented in the previous chapter. Since this chapter is largely based on our paper [49] on this mixer, we will follow the structure of this paper.

The analysis of bio-fluids in lab-on-chip devices involves fluid transport and fluid mixing in micro-channels. Due to the small length scales, viscous forces gain importance with respect to inertial forces, rendering turbulent mixing impossible. The ratio between inertial and viscous forces is characterized by the Reynolds number (Re), so for microfluidic devices Re is usually smaller than 1. Diffusive mixing on the other hand, is slow, even at these small length scales, since material transport is still convection dominated. The ratio between convective and diffusive mass transport is given by the Péclet number (Pe), which is generally large for microfluidic devices. Therefore novel mixing concepts have to be developed leading to chaotic advection at low Re , but high Pe .

Among them are active mixers [1] and passive mixers [19, 20]. For active micro-mixers operating in cycles, net flow can only be induced through temporal or spatial asymmetry. If $Re \ll 1$, *i.e.* under Stokes flow conditions, only spatial asymmetry remains to achieve a net flow effect. By mimicking fluid transport at the sub-millimeter scale from nature, more in particular from ciliated Paramecia, Den Toonder *et al.* [1] have created a micro-mixer with artificial cilia. The electrostatically actuated artificial cilia were polymer based micro-actuators coated with an ultra thin conductive film, see Figure 3.1. The

¹This chapter is largely based on: M. Baltussen, P. Anderson, F. Bos, and J. den Toonder. Inertial effects in a micro-mixer based on artificial cilia. *Lab Chip*, 9:2326 – 2331, 2009

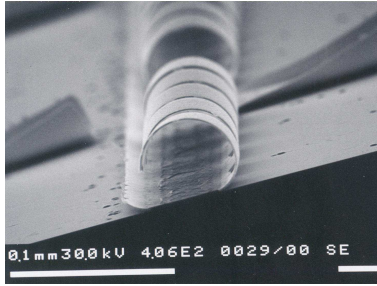


Figure 3.1: A micrograph of the curled polymer MEMS in its non-actuated shape.

cilia are actuated in a cycle which consists of two phases:

- A constant voltage difference between the substrate and the film is applied, causing the film to roll out fully onto the substrate.
- The potential difference is switched off and the cilium recovers elastically back to its initial configuration.

Unit cells of 1 mm^2 containing 100 of these cilia were placed in arrays at the bottom of the micro-channel, see Figure 3.2(a), and integrated into a microfluidic device Figure 3.2(b). This micromixer generated substantial flow velocities. The mixing as observed from a top view of the channel was good, but above all very fast. Over the length of two unit cells (of 1 mm each), the fluid is mixed, which was not expected for a micro-mixer in Stokes flow. A closer look reveals however that the local velocities U of the cilia are in the order of $0.1 - 1 \text{ m s}^{-1}$, hence the local Reynolds number, $\text{Re} = \frac{\rho U L}{\eta} = 1 - 10$, with density $\rho = 9.3 \cdot 10^2 \text{ kg m}^{-3}$, cilium length $L = 100 \mu\text{m}$ and viscosity $\eta = 9.3 \text{ mPa s}$, based on the silicone oil used in experiments. Therefore, the flow on the length scale of the cilia is dominated by inertia, for at least part of the actuation cycle. The mixing quality was assessed by taking images from a top view of the channel, hence the flow in a cross-section of the channel is unknown, so it could be that large structured layers exist in the cross-sectional plane. In this case the fluid is highly segregated in the cross-sectional plane, while it seems fully mixed from the top. Also the role of inertia on the generated flow remains unsure. Therefore the objective is to study the mixing patterns in the cross-sections of this micro-mixer with a both a numerical model and experiments, and assess the role of inertia.

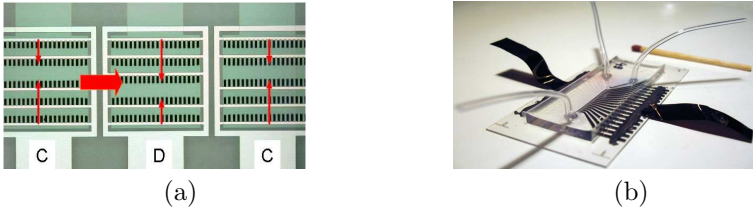


Figure 3.2: (a) The actual mixing channel viewed from the top showing three unit cells in alternating order. The large arrow indicates the imposed flow direction, and the small arrows indicate the actuation direction of the row of cilia. (b) The Y-channel with two inputs and one output. The artificial cilia are integrated on the bottom of the channel.

3.1 Modelling

The mixing device of den Toonder *et al.* [1] is modelled. This device consists of a Y-shaped channel with two inflows and one outflow, see Figure 3.2b. The bottom of the channel is covered with curled actuators, the artificial cilia, see Figure 3.1. These cilia are electrostatically actuated polymer MEMS. Sixteen mixing units of $1 \times 1 \text{ mm}^2$ each with 5×20 artificial cilia are placed on the bottom of the channel, see Figure 3.2a for a top view of the mixing units. The two-dimensional cross-section of the channel is modeled. So the cilia

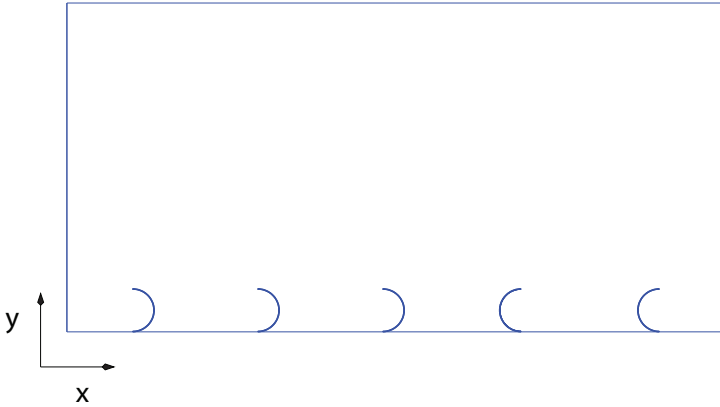


Figure 3.3: The modeled cross-sectional domain with five cilia on the bottom of the channel.

are assumed infinitely long in the imposed flow direction. The channel and the modeled domain are depicted in Figure 3.3. The channel has a height of 0.5 mm , and a width of 1.0 mm . Each cilium has a thickness T_c of $2 \mu\text{m}$, and length L of $100 \mu\text{m}$. Although the artificial cilia are layered structures, with

different mechanical properties, the entire cilium is modeled as a single solid with the properties of the thickest layer, which is polyimide. The initial curled shape with radius $R = 32 \mu\text{m}$ of the cilia is shown in Figure 3.3. The cilia are attached to the channel floor at one end. The fluid domain Ω_f is modeled as an incompressible Newtonian fluid, and the solid domain as an incompressible, inertialess, neo-Hookean solid. The fluid is modeled in an Eulerian manner, the solid in a Lagrangian manner. This leads to the following conservation equations of mass and momentum, see Equations (2.1) and (2.4):

$$\begin{aligned} \text{Fluid:} \\ \nabla \cdot \mathbf{u} &= 0 && \text{in } \Omega_f, \end{aligned} \quad (3.1)$$

$$\rho_f \left(\frac{\partial \mathbf{u}}{\partial t} + \mathbf{u} \cdot \nabla \mathbf{u} \right) = \nabla \cdot \boldsymbol{\sigma}_f \quad \text{in } \Omega_f, \quad (3.2)$$

$$\begin{aligned} \text{Solid:} \\ \det(\mathbf{F}) - 1 &= 0 && \text{in } \Omega_s, \end{aligned} \quad (3.3)$$

$$-\nabla \cdot \boldsymbol{\sigma}_s = \mathbf{f}_s \quad \text{in } \Omega_s, \quad (3.4)$$

where the variables are defined as in Section 2.1 and \mathbf{f}_s is the actuation force on the solid.

No-slip boundary conditions are taken on the channel walls and the cilia are attached to the wall at the lowest vertical boundary, *i.e.* the channel floor. On the fluid/solid boundary, the interface conditions Equations (2.11) and (2.12) hold.

3.1.1 Actuation

The cilium is actuated electrostatically. The electrostatic surface force is modelled by assuming a parallel plate capacitor geometry, where the upper plate with potential ΔV is the cilium and the lower, grounded plate the channel floor. An electric field $\mathbf{E} = -\Delta V/h\mathbf{e}_y$ exists between the upper and lower plate, with h the distance between the upper and lower plate. Since the cilia move, the distance between the cilium and the wall also changes. Hence the local electric field changes through a change in h . This electric field causes a traction on both conducting plates, which attracts the cilium towards the bottom of the channel so that it rolls out onto the bottom. By making use of the Gauss divergence theorem and the Maxwell stress tensor this traction on the upper plate is given by [46], see Section 2.3.1:

$$\mathbf{t} = -\mathbf{n} \cdot \boldsymbol{\sigma}_M = -\mathbf{e}_y \cdot \epsilon \left(\mathbf{E}\mathbf{E} - \frac{\mathbf{E} \cdot \mathbf{E}}{2} \mathbf{I} \right), \quad (3.5)$$

where ϵ is the dielectric constant of the fluid between the two plates, $\mathbf{n} = -\mathbf{e}_y$ the vector normal to the upper plate. For numerical reasons, the traction on

the boundary is transformed into a body force \mathbf{f}_s by assuming a averaging \mathbf{t} over the cilium thickness T_c , leading to:

$$\mathbf{f}_s = \frac{-\epsilon}{2T_c} \left(\frac{\Delta V}{h} \right)^2 \mathbf{e}_y. \quad (3.6)$$

One full cycle of the cilium motion will be simulated. The actuation force will be applied until the cilia are fully unrolled, so flat against the lower wall. Then the force is released and the cilia recover elastically to their initial shape. The cycle is finished when the fluid has come to a rest. The velocity field obtained from this cycle is used as input for particle tracking for 50 cycles.

3.1.2 Scaling

The problem is governed by two dimensionless groups, see Section 2.4, namely the Reynolds number (Re) and R_1 defined as the ratio between elastic and applied forces in the cilium $R_1 = \frac{L^2 f_0}{D}$, where the typical displacement D is taken equal to L and $f_0 = 1.75 \cdot 10^9 \text{ N m}^{-3}$ is the typical force computed from the following parameters used in experiments [1]: $\epsilon = 8.854 \cdot 10^{-12} \text{ A}^2 \text{ s}^4 \text{ kg}^{-1} \text{ m}^{-3}$, $\Delta V = 100 \text{ V}$, $h = 1 \mu\text{m}$ and $T_c = 2 \mu\text{m}$. The typical length scale h for the applied force is taken equal to the dielectric layer thickness of the experimental device [1]. The fluid has a viscosity of 9.3 mPa s . The Reynolds number is varied from 0 to 10 by changing the density between 0 and 9300 kg m^{-3} . The solid has a modulus of 1 GPa , hence $R_1 = 5.7 \cdot 10^3$ throughout all calculations.

3.2 Numerical methods

The set of Equations (3.1)-(3.4) is solved with a finite element method (FEM). A fictitious domain method [50] is used where the solid “floats” inside the fluid domain, which comprises both the fluid and solid domain:

$$\hat{\Omega}_f = \Omega_f \cup \Omega_s, \quad (3.7)$$

where $\hat{\Omega}_f$ is the total fluid domain, containing the fictitious part Ω_s . This fictitious part leads to additional physical effects, which may be neglected if the momentum of the fictitious fluid is lower than the momentum of the solid. Here we assume that this is the case. This method has been successfully used for the simulation of particle suspensions [51, 52] and fluid-structure interaction [28, 33, 53]. The corresponding weak form of Equations (3.1)-(3.4), after introducing test functions $\mathbf{v}, q, \mathbf{w}, r$, integration over the entire domain and applying partial integration reads: Find $\mathbf{u} \in \mathcal{U}, p_f \in \mathcal{P}_f, \mathbf{d} \in \mathcal{D}, p_s \in \mathcal{P}_s$ such

that:

$$\begin{aligned}
& (q, \nabla \cdot \mathbf{u})_{\hat{\Omega}_f} = 0, \\
& \left(\mathbf{v}, \operatorname{Re} \left(\frac{\partial \mathbf{u}}{\partial t} + \mathbf{u} \cdot \nabla \mathbf{u} \right) \right)_{\hat{\Omega}_f} + \\
& (\mathbf{D}_v, \mathbf{D})_{\hat{\Omega}_f} - (\mathbf{v}, \mathbf{n} \cdot 2\mathbf{D} - p_f \mathbf{I})_{\Gamma_f} + (\mathbf{v}, \nabla p_f)_{\hat{\Omega}_f} = 0, \\
& (r, \det(\mathbf{F}) - 1)_{\Omega_s} = 0, \\
& (\mathbf{D}_w, \mathbf{B} - \mathbf{I})_{\Omega_s} - (\mathbf{w}, \mathbf{n} \cdot (\mathbf{B} - \mathbf{I} - p_s \mathbf{I}))_{\Gamma_s} - \\
& (\mathbf{w}, \mathbf{f}_s)_{\Omega_s} = 0, \\
& \forall \mathbf{v} \in \mathcal{U}, q \in \mathcal{P}_f, \mathbf{w} \in \mathcal{D}, r \in \mathcal{P}_s,
\end{aligned} \tag{3.8}$$

where $(a, b)_\Omega$ denotes the proper inner product of functions a and b on the domain Ω and $\mathbf{D}_a = \frac{1}{2}(\nabla \mathbf{a}^T + \nabla \mathbf{a})$. In this weak form boundary terms arise due to partial integration. These terms represent the traction on the fluid and solid boundaries Γ_f and Γ_s respectively. These boundaries can be split into a part where Dirichlet and Neumann boundary conditions are applied, such that $\Gamma = \Gamma_D \cup \Gamma_N$. Since no Neumann conditions are present in this problem, the entire boundary is Dirichlet.

The interface conditions are applied with a Lagrange multiplier method [50, 54] which adds the kinematic interface condition as a constraint to the weak form (3.8) leading to the following additional terms:

$$\left(\mathbf{s}, \mathbf{u} - \dot{\mathbf{d}} \right)_{\Gamma_{fs}} + (\mathbf{v}, \boldsymbol{\lambda})_{\Gamma_{fs}} - (\mathbf{w}, \boldsymbol{\lambda})_{\Gamma_{fs}} \quad \forall \mathbf{s} \in \mathcal{L}, \tag{3.9}$$

where $\dot{\mathbf{d}} = \frac{d\mathbf{d}}{dt}$, $\boldsymbol{\lambda} \in \mathcal{L}$ is the Lagrange multiplier and $\mathbf{s} \in \mathcal{L}$ is the test function for the weak form of the kinematic interface condition. The Lagrange multiplier is identified to be the traction on Γ_{fs} : $\boldsymbol{\lambda} = \mathbf{n} \cdot (2\mathbf{D} - p_f \mathbf{I}) = -\mathbf{n} \cdot (\mathbf{B} - \mathbf{I} - p_s \mathbf{I})$. Thus the dynamic interface condition is also fulfilled since the tractions on the fluid and the solid are, apart from the sign, the same, namely $\boldsymbol{\lambda}$.

Since the set of equations is timedependent and nonlinear, appropriate timestepping and linearization have to be applied, in order to solve them. Using first-order implicit Euler for the time-dependent terms and Newton-Raphson iteration for the non-linear terms, the final set of equations to be solved is:

Find $\mathbf{u}_{j+1}^{i+1} \in \mathcal{U}, p_{f,j+1}^{i+1} \in \mathcal{P}_f, \delta \mathbf{d}_{j+1}^{i+1} \in \mathcal{D}, p_{s,j+1}^{i+1} \in \mathcal{P}_s, \boldsymbol{\lambda}_{j+1}^{i+1} \in \mathcal{L}$ such that:

$$\begin{aligned}
& - (q, \nabla \cdot \mathbf{u}_{j+1}^{i+1})_{\hat{\Omega}_f} = 0, \\
& \left(\mathbf{v}, \operatorname{Re} \left(\frac{\mathbf{u}_{j+1}^{i+1} - \mathbf{u}^i}{\Delta t} + \mathbf{u}_{j+1}^{i+1} \cdot \nabla \mathbf{u}_{j+1}^{i+1} \right) \right)_{\hat{\Omega}_f} + \\
& (\mathbf{D}_v, \mathbf{D}_{j+1}^{i+1})_{\hat{\Omega}_f} - (\mathbf{v}, \nabla p_{f,j+1}^{i+1})_{\hat{\Omega}_f} + (\mathbf{v}, \boldsymbol{\lambda})_{\Gamma_{fs}} = 0 \\
& (r, \det(\mathbf{F}_{j+1}^{i+1}) - 1)_{\Omega_s} = 0, \\
& (\mathbf{D}_w, \operatorname{R}_1(\mathbf{B}_{j+1}^{i+1} - \mathbf{I}))_{\Omega_s} - (\mathbf{w}, \nabla p_{s,j+1}^{i+1})_{\Omega_s} + \\
& (\mathbf{w}, \mathbf{f}_{s,j+1}^{i+1})_{\Omega_s} - (\mathbf{w}, \boldsymbol{\lambda})_{\Gamma_{fs}} = 0, \\
& \left(\mathbf{s}, \mathbf{u}_{j+1}^{i+1} - \frac{\mathbf{d}_j^{i+1} + \delta \mathbf{d} - \mathbf{d}^i}{\Delta t} \right)_{\Gamma_{fs}} = 0, \\
& \forall \mathbf{v} \in \mathcal{U}, q \in \mathcal{P}_f, \mathbf{w} \in \mathcal{D}, r \in \mathcal{P}_s, \mathbf{s} \in \mathcal{L}, \tag{3.10}
\end{aligned}$$

where $i+1$ and i denote the value at the current and previous time $t^{i+1} = t^i + \Delta t$, $j+1$ and j the current and previous iterative step and $\delta \mathbf{d}$ is the iterative displacement step. Details about the time integration and linearization can be found in Appendix A, Sections A.1 and A.2.

The shape functions for the trial functions $(\mathbf{u}, p_f, \delta \mathbf{d}, p_s, \boldsymbol{\lambda})$ and their corresponding weight functions $(\mathbf{v}, q, \mathbf{w}, r, \mathbf{s})$ are $(Q_2^9, Q_1^4, Q_2^9, Q_1^4, P_1^2)$. The combination $Q_2^4 Q_1^4$ is a stable element for incompressible problems from the Taylor-Hood family.

The final set of equations will be solved with a direct solver (HSL MA41 [55]) in a fully coupled manner.

3.3 Experiments

The distributive mixing flow is visualized by optical coherence tomography (OCT) [56, 57]. In this procedure particles are illuminated by a low coherent light source. From the reflected light beam and a reference beam a interference pattern can be drawn which shows the particle positions. The main advantage of this technique is that it can measure particle positions very deep in translucent objects, which is ideal for this micro-mixer since the channel is made from PDMS. OCT generated time-dependent images of the flow pattern evolution within the same cross-sectional plane as the simulations are recorded.

3.3.1 Materials

The experimental device and set-up as described in detail in Den Toonder *et al.* [1] was used in this experiment. The channel is Y-shaped, with two fluid

inlets and one outlet. The width of the channel is 1 mm, the height 0.5 mm and the length 2 cm respectively. The floor of the channel is covered with 16 adjacent areas of 1 mm \times 1 mm squares with 5 rows of 20 cilia each, see Figure 3.2a. Both of the entrances were connected to a syringe pump (Harvard Apparatus, Model 11- plus, single syringe pump). One syringe contained silicone oil (Wacker AK10) with a viscosity of 9.3 mPa s with a density of 930 kgm⁻³, the other syringe contained the same oil seeded with TiO₂ particles, with a density of 4500 kgm⁻³.

Due to the density difference between the particles and the oil, sedimentation occurs. The sedimentation velocity [58] of particles with a radius of 10 μ m under Stokes conditions is 80 μ ms⁻¹, which is much lower than the typical velocity in the cross-sectional plane of 1 ms⁻¹, hence particles follow the flow sufficiently to characterize the flow. In the axial channel direction however the velocity is only 0.2 mm s⁻¹, so the influence of gravity and pumping are of the same order and the particles do not follow the flow. Therefore sedimentation takes place while particles move through the channel, but the particle motion in the cross-sectional plane represents the fluid motion.

The Spectral Radar Optical Coherence Tomography System of Thorlabs GmbH was used, which has a depth resolution of 3.5 μ m, an in-plane resolution of 10 μ m, and which can capture eight frames per second. Although 3D visualizations are possible, only the cross-sectional flow at a single axial position in the channel was captured.

3.3.2 Methods

The experiments were conducted as follows: First the two pumps and the OCT set-up were switched on. After two distinct separate flows were observed, the artificial cilia were actuated at 80 Hz and a recording was started. After about 15 minutes the heavier TiO₂ particles sedimented on the cilia, resulting in cilia malfunction and the experiment was stopped. Since the OCT sampling frequency is only 8 Hz, while the cilia actuation frequency is 80 Hz, individual cycles cannot be distinguished. Due to the high electric fields 100 V/1 μ m = 100 MV m⁻¹, electrokinetic effects are expected, but the use of an AC field at 1 kHz prevented these effects.

3.4 Results

Net fluid motion for Stokes flow only happens if the cilia motion is asymmetric. The asymmetry of the cilia movement can be visualized by plotting the path of the very tip of the cilium over one cycle. If the rolling path and rolling-back path do not coincide, the motion is asymmetric. The size of the area enclosed by both paths, the swept area, is a measure for extent of the asymmetry. The direction of fluid motion can also be deduced from this plot. For inertial

flow this is not the case, since also the time-scales of rolling and rolling-back play a role. The simulated tip position of the left most cilium within the computational domain is given in Figure 3.4 for $Re = 0$ (left) and $Re = 10$ (right). From Figure 3.4 it is observed that for $Re = 0$ the net flow will be

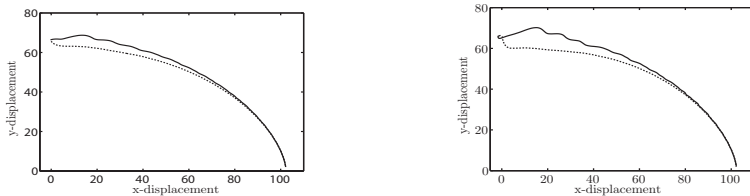


Figure 3.4: Simulated tip position of the leftmost cilium for $Re = 0$ (left) and $Re = 10$ (right). The dashed line is the unrolling path when the electric force is switched on, the solid line is the rolling path during which the force is switched off. The left most position is the starting position. Both displacements are given in micrometers.

to the left for this cilium, since the path during recovery lies above the path during unrolling. The amount of fluid which is displaced is relatively small compared to the entire swept area. For $Re = 10$, the net swept area increases but not significantly. Furthermore the flow direction is unknown, since also the timescales of unrolling and recovering play a role.

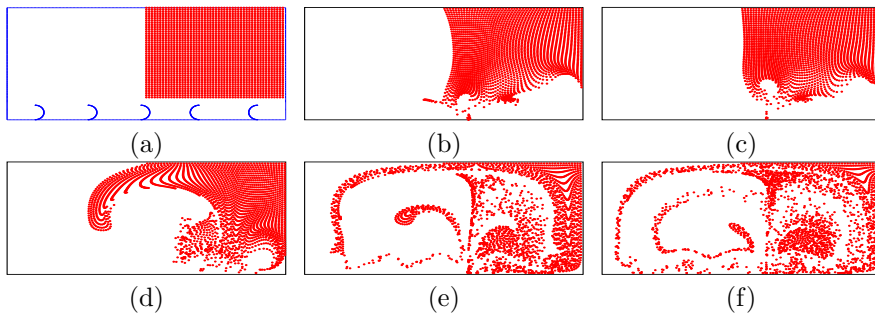


Figure 3.5: Original particle distribution (a). Particle distributions after 50 cycles for $Re = 0$ (b), $Re = 0.1$ (c), $Re = 1$ (d), $Re = 5$ (e) and $Re = 10$ (f). The Reynolds number is based on the cilium length.

The distributive mixing properties for different Reynolds numbers are studied next. A rectangular block containing 2500 particles is placed in the right half of the domain, see Figure 3.5(a). These particles are convected by the flow for 50 cycles of cilia actuation and their final positions are plotted in Figure 3.5 for various local Reynolds numbers. The distribution of particles over the domain becomes better for higher Reynolds number, indicating better

distributive mixing. The motion of particles for $Re = 0, 0.1$ is in the opposite direction to that of the $Re = 1, 5, 10$ simulations. Therefore a Reynolds number exist where there is no global flow, and hence mixing only occurs on the local level. This is the critical Re where the flow direction changes. Two flow domains can be seen, one for the three left cilia and one for the two right cilia. The distinct change in flow around $Re = 1$ is also observed in nature [59]. In order to quantify the mixing effectiveness, the entropy increase rate κ_S , as defined in (2.38), is computed for a typical domain size of 30×15 cells, and given in Figure 3.6. From this figure it is observed that for $Re = 0, 0.1$, κ_S is negative, indicating structure formation, so we have demixing rather than mixing. For $Re = 1$ κ_S remains about constant, so although the particles move, the distribution remains about the same. For $Re = 5, 10$ increases, indicating good mixing. Due to inaccuracies in the velocity field, several particles are accumulated on the moving cilium and on the lower wall, as can be seen in Figure 3.5. If the particles should be tracked for even more cycles, more and more particles are artificially accumulated in these areas. In order to obtain accurate mixing simulations a more accurate model is required, so that this accumulation is avoided. The particle distributions for $Re = 1$ at 50 cycles,

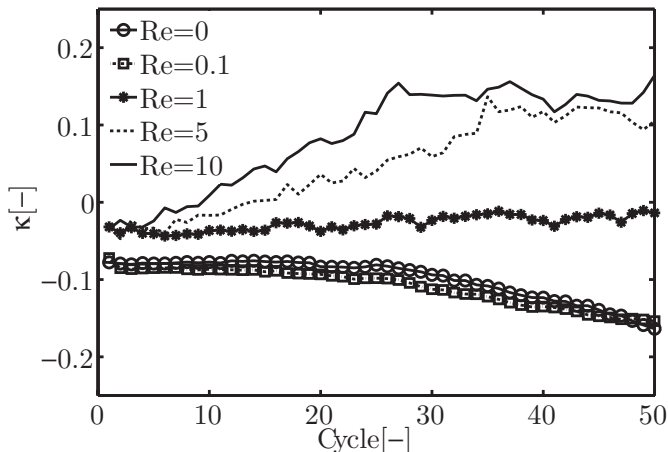


Figure 3.6: Evolution of the entropy increase rate κ_S for a range of Reynolds numbers.

$Re = 5$ at 12 cycles and $Re = 10$ at 5 cycles are almost identical, see Figure 3.7. This indicates that the net flow per cycle increases with the Reynolds number, while the basic flow remains the same. This means however that the same mixing state can be reached for all Re above the critical Re by just increasing the number of cycles.

Thus far the numerical simulations show that Stokes flow and inertial flow



Figure 3.7: Simulated particle distributions for $Re = 1$, 50 cycles (left), $Re = 5$, 12 cycles (middle) and $Re = 10$, 8 cycles (right).

give different flow patterns and that particles are better distributed for higher Reynolds numbers. In the experiments, the Reynolds number is estimated to be of $\mathcal{O}(1)$. This is based on a local fluid velocity, taken equal to the cilium velocity, of 1 ms^{-1} a density of 0.93 kgm^{-3} , a cilium length $100 \text{ }\mu\text{m}$ and a viscosity of 9.3 mPa s . It was therefore hypothesised that local inertial effects could play an important role [1]. This is indeed verified by comparing the flow structure as measured by OCT with the computed patterns, shown in Figure 3.8. The experimental results resemble the numerical results for high Reynolds numbers, when inertia is important, well, whereas the simulated patterns for the low Reynolds numbers are completely different. The number of simulated and observed cycles differ however. Following the previous paragraph, the same mixing state can be obtained for any Re above the critical Reynolds number. This indicates that $Re = 10$ is higher than the actual Re in experiments, but still the computed particle distributions can be used for comparison with experiments, as long as the comparison is made at a different number of cycles, as is done in Figure 3.8. Both experiments and simulations show that the initial

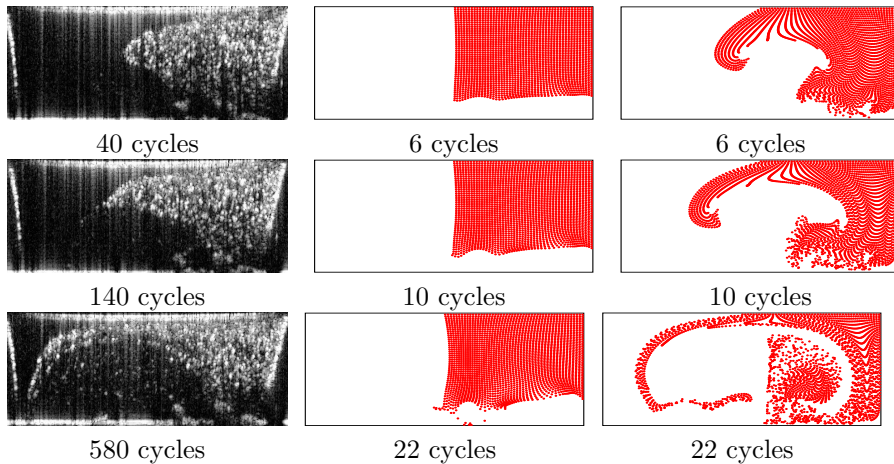


Figure 3.8: Left: images from OCT experiments. Middle: simulated particle distributions for $Re = 0$. Right: simulated particle distributions for $Re = 10$.

block of particles is stretched. Stretching alone will not give good mixing

however. From simulations it is clear that a separatrix exists between the two cilia groups. Hence fluid in one domain cannot get into the other domain, and good mixing cannot be obtained. Therefore symmetry breaking is necessary [60], which can be obtained by placing segments with mirrored alternating layouts in the channel, as shown in Fig. 2a. The alternating use of 3-2 and 2-3 configurations shifts the separatrix within the channel, breaking symmetry.

3.5 Conclusions

Numerical simulations and experimental visualization of the flow in the micro-mixer which is based on electrostatic artificial cilia have been performed. For five different Reynolds numbers, based on the cilium length and speed, a direct numerical simulation of one cilium motion cycle has been carried out. The obtained velocity field has been used for tracking particles for multiple cycles. The resulting particle distributions show that for $Re = 0, 0.1$ the nature of the induced flow is opposite to the flow for $Re = 1, 5, 10$. This is due to the growing importance of inertial effects for larger Re . It is also observed that increasingly better distributive mixing occurs for $Re = 1, 5, 10$. The simulation results are compared with optical coherence tomography flow visualizations, and good qualitative comparison is found for the $Re = 10$ case. This confirms that the observed flow behavior in the mixer based on artificial cilia is caused by inertial, rather than viscous phenomena.

Although these simulations give insight in the physics controlling the mixing behavior, it cannot be used for mixing simulations of more cycles, due to the inaccuracy of the velocity field near the cilium. Hence more accurate models are required in these simulations.

Chapter 4

XFEM and weak interface conditions

This chapter treats the numerical aspects of fluid structure interaction modeling. Due to the flexibility of the cilia, large deformations are expected. Methods in which both the fluid and solid mesh deform are therefore not that attractive, since large deformations deteriorate the mesh quality, thus leading to inaccurate solutions. A possible solution is the generation of a new mesh when the mesh becomes too distorted. This is not attractive in general, since mesh generation is expensive. Another solution is to keep the fluid mesh stationary and let the solid mesh move. With this solution no re meshing is required, so this approach is computationally cheaper. On the other hand the interface conditions (2.11) and (2.12) are only aligned with the solid mesh, and not with the fluid mesh, which makes it more difficult to enforce both conditions accurately. In the previous chapter a fictitious domain/Lagrange multiplier technique has been used for enforcing these conditions. The simulations from the previous chapter tell us something about the large scale physics at hand; namely that fluid inertia is important in this particular mixer. Near the fluid-structure interface however, the results are not very accurate. Let us consider the following typical example of pressure driven flow over a single cilium is given. For a large cilium deformation, the fluid velocity, pressure, vorticity and shear-stress on the boundary of the cilium are shown in Figure 4.1.

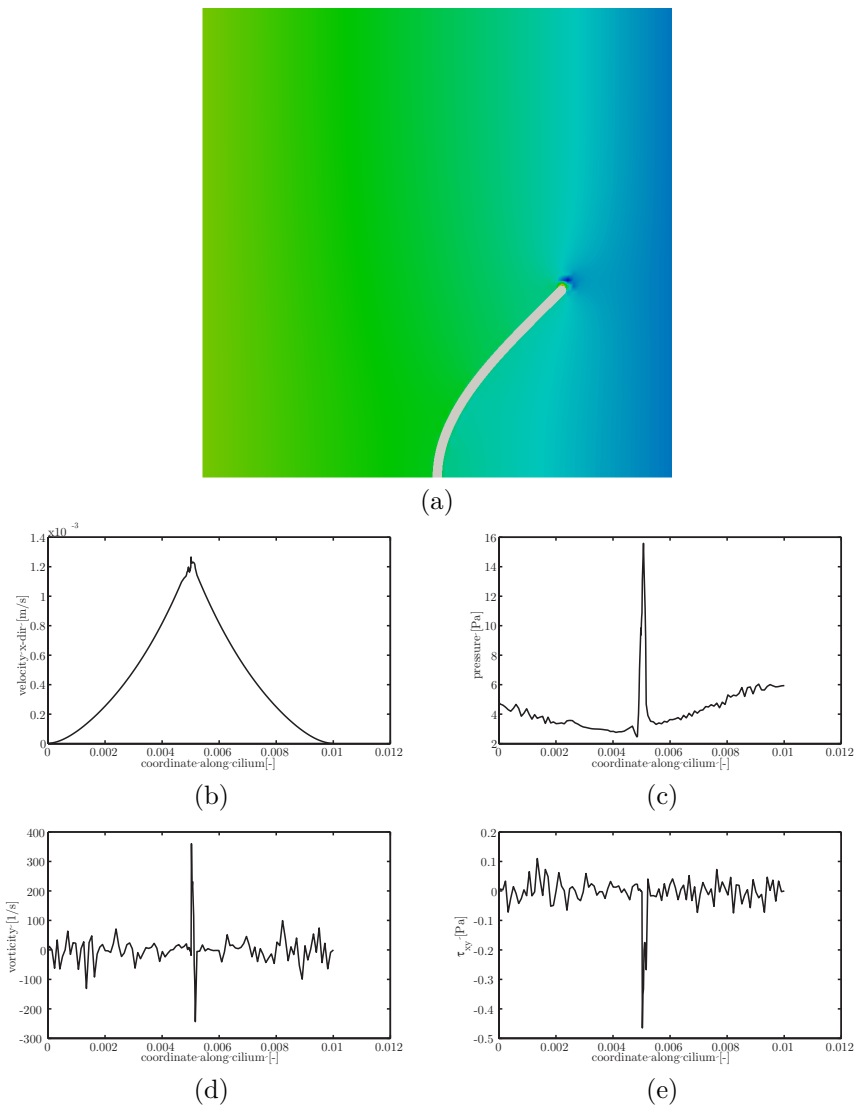


Figure 4.1: The fluid domain with the deformed cilium with the fluid pressure (a) and the following quantities on the boundary: velocity in x -direction (b), pressure (c), vorticity (d) and shear-stress (e).

The velocity field along the boundary is more or less smooth, but the pressure and the derived quantities such as the vorticity and shear-stress, show non-smooth behavior. So at least at the boundary these quantities are not smooth and also not accurate, since a shear-stress which is rapidly changing sign is not physically valid. These errors are caused by two effects:

- In the fictitious domain technique the solid floats in the fluid. Hence the equations of motion of the fluid are not only applied in the fluid domain, but also in the solid domain. This is unphysical as it causes the fluid domain to be continuous, whilst in reality is discontinuous.
- In order for the Lagrange multiplier technique to be stable, strict requirements have to be put on its discretization [54]. If the discretization is too dense compared to the fluid element, too many interface conditions are enforced causing spurious oscillations, whilst if too few are enforced, the interface conditions are, obviously, violated.

Both issues are of concern to us, since we want to accurately describe the flow field near the cilium, in order to perform mixing analysis, and, as will be shown in later chapters, to study the flow of a viscoelastic fluid pumped by cilia. For mixing analysis the accuracy of the velocity field is important, since the analysis relies on the tracking of points. If the velocity field is inaccurate, points end up at the boundaries of the domain, or, which is more likely, at the cilium wall. For the simulation of transport of non-Newtonian fluids the velocity gradients have to be accurate, since errors in the velocity gradient is a cause for numerical instability of the simulation. A solution to both problems mentioned above will be given in this chapter. The methods which solve these problems are also found in a recent paper [61]. First the problem of introducing discontinuities into a finite element by using the eXtended Finite Element Method (XFEM) is given in Section 4.1. Subsequently methods for enforcing the kinematic interface condition are given in Section 4.2. The Arbitrary Lagrange Euler method (ALE) will also be introduced in this chapter. It is used for computing reference solutions, against which new methods are compared, and as a starting point for the derivation of schemes for problems having instationary and convective terms in the fluid domain. The solid is modeled in a Lagrangian reference frame, which moves along with the solid. Hence the inertial terms can be treated with standard techniques, as will be shown in Subsection 4.3.

4.1 XFEM

The classical Galerkin Finite Element Method (GFEM), uses polynomials as shapefunctions for the test and trial functions. The entire domain is subdivided into smaller domains, the elements, which together form the mesh. The polynomials are defined element wise. Since the test and trial functions are polynomials, they are at least continuous within an element. Therefore discontinuities cannot be described accurately within an element. At the boundary between elements however they can be described accurately, since the shapefunctions of an element are only defined in that single element. So in many problems where discontinuities arise (fluid-structure interaction, multi compo-

ment flow, contact) the mesh is generated in such a way that it aligns with the discontinuities in the field variable or its derivatives. If the position of the discontinuities is time dependent, the element boundaries should follow the discontinuities, which requires motion of the mesh itself. Often the movement of the mesh is large, causing the elements to be elongated or distorted. Since the geometrical shape of an element in part determines the accuracy, elongated and distorted elements should be avoided and preparing a new mesh of (part of) the domain is often the only option.

The eXtended Finite Element Method XFEM allows the use of many more functions as shapefunction. Usually additional functions are added to the traditional polynomials in the following way:

$$a \approx \sum_{i=1}^N \phi_i(\mathbf{x}) A_i(\mathbf{x}); \quad A_i(\mathbf{x}) = a_i + \sum_{i=1}^N \sum_{j=1}^M f_j(\mathbf{x}) a_{ji}, \quad (4.1)$$

where a is the function to be approximated, N are the number of degrees of freedom of variable a , ϕ_i is the i -th polynomial shapefunction, a_i the standard degree of freedom in node i , f_j is an additional function, M the number of additional functions and a_{ij} the additional degrees of freedom for function j in node i . So by introducing extra functions, also the number of degrees of freedom increases.

In the case of fluid solid interaction, in absence of interfacial forces (such as electrostatic forces or interfacial tension) the velocity and traction are continuous over Γ_{fs} , leading to the interface conditions:

$$\mathbf{u} - \dot{\mathbf{d}} = \mathbf{0}, \quad (4.2)$$

$$\mathbf{n} \cdot \boldsymbol{\sigma}_f - \mathbf{n} \cdot \boldsymbol{\sigma}_s = \mathbf{0}, \quad (4.3)$$

where \mathbf{u} is the fluid velocity, $\dot{\mathbf{d}}$ the solid velocity, \mathbf{n} the outward normal of the fluid on Γ_{fs} , $\boldsymbol{\sigma}_f$ the fluid stress and $\boldsymbol{\sigma}_s$ the solid stress. The solid and fluid stresses and the derivatives of the displacement and velocity may be discontinuous, and often are. Note, that if the stress is discontinuous, the pressure is discontinuous as well (except if the other contributions to the stress are exactly the same).

Since the equations of motion of the solid are defined in a Lagrangian frame, the fluid-structure interface is always aligned with the boundary edges of the solid elements. Hence the discontinuity in the stress, pressure and displacement derivatives do not require any special treatment. The discontinuity of stress, pressure and velocity gradient in the fluid domain requires special treatment however, since the equations of motion of the fluid are defined in a fixed Eulerian frame, with corresponding fixed elements.

Following the XFEM framework the following shape functions for \mathbf{u} , p_f , \mathbf{d} , p_s

and their corresponding testfunctions $\mathbf{v}, q, \mathbf{w}, r$ are introduced:

$$\mathbf{u} \approx \sum_{i=1}^{Nv} \phi_i(\mathbf{x}) \mathbf{U}_i(\mathbf{x}); \quad \mathbf{U}_i(\mathbf{x}) = \mathbf{u}_i H(\mathbf{x}) \quad (4.4)$$

$$p_f \approx \sum_{i=1}^{Npf} \psi_i(\mathbf{x}) P_{f,i}(\mathbf{x}); \quad P_{f,i}(\mathbf{x}) = p_{f,i} H(\mathbf{x}), \quad (4.5)$$

$$\mathbf{d} \approx \sum_{i=1}^{Nd} \mu_i(\mathbf{x}) \mathbf{D}_i(\mathbf{x}) \quad (4.6)$$

$$p_s \approx \sum_{i=1}^{Nps} \mu_i(\mathbf{x}) P_{s,i}(\mathbf{x}) \quad (4.7)$$

$$\mathbf{v} \approx \sum_{i=1}^{Nv} \phi_i(\mathbf{x}) \mathbf{V}_i(\mathbf{x}); \quad \mathbf{V}_i(\mathbf{x}) = \mathbf{u}_i H(\mathbf{x}) \quad (4.8)$$

$$q \approx \sum_{i=1}^{Npf} \psi_i(\mathbf{x}) Q_i(\mathbf{x}); \quad Q_i(\mathbf{x}) = q_i H(\mathbf{x}), \quad (4.9)$$

$$\mathbf{w} \approx \sum_{i=1}^{Nw} \mu_i(\mathbf{x}) \mathbf{W}_i(\mathbf{x}) \quad (4.10)$$

$$r \approx \sum_{i=1}^{Nps} \mu_i(\mathbf{x}) R_i(\mathbf{x}) \quad (4.11)$$

where $H(\mathbf{x})$ is a Heaviside function defined as:

$$H(\mathbf{x}) = \begin{cases} 0 & \forall \mathbf{x} \in \Omega_s, \\ 1 & \forall \mathbf{x} \in \Omega_f, \end{cases} \quad (4.12)$$

and N_v, N_{pf}, N_d, N_{ps} denote the amount of the degrees of freedom for the velocity, fluid pressure, displacement and solid pressure respectively. By using the Heaviside function, the shape functions do only exist in the part of the element which contains fluid. This requires the exact knowledge about which part of a fluid element contains fluid and which part contains the solid. How to define these two regions is the topic of the next subsection.

4.1.1 Subdomain splitting

A fluid element is intersected by a solid element as depicted in Figure 4.2. The intersection defines the border between the areas where $H(\mathbf{x})$ is zero and one. Hence it splits the fluid domain into two parts. For problems with rigid body motions, an interface description by a levelset function has been used for

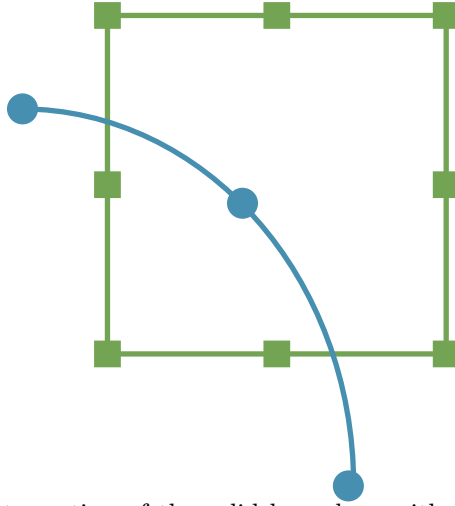


Figure 4.2: The intersection of the solid boundary with a fluid element, the squares \blacksquare denote the nodes of the fluid element, the circles \bullet the nodes of the solid boundary.

defining both regions in the fluid domain. This levelset based quadtree/eltree subdivision scheme has been used successfully by several authors [38, 62]. Here we will employ the following strategy, which is also graphically depicted in Figure 4.3:

- Find all the intersections of the solid boundary with the edges of the fluid element.
- Perform a Delaunay triangulation on all nodes of the fluid element, the solid boundary element and the intersection points. This generates a full Delaunay triangulation for the entire fluid element. More information about performing the Delaunay triangulation is given in Appendix B.
- Find the triangles which are in the fluid or solid.
- Since the solid displacement has Q_2 shape functions, the boundary is also a quadratic curve. The Delaunay algorithm creates linear triangles however, so additional points are added to the linear triangles to make them quadratic. This also ensures that the triangle exactly aligns with the solid boundary
- The triangles are used as sub-element for the spatial integration of the governing equations.
- Spatial integration of integrals over the interface takes place on line elements on the interface which follow the solids discretization. Hence line

elements which intersect with fluid elements are split into two sub line elements.

With this method the solid boundary is exactly followed, so no “hole” or overlap exist.

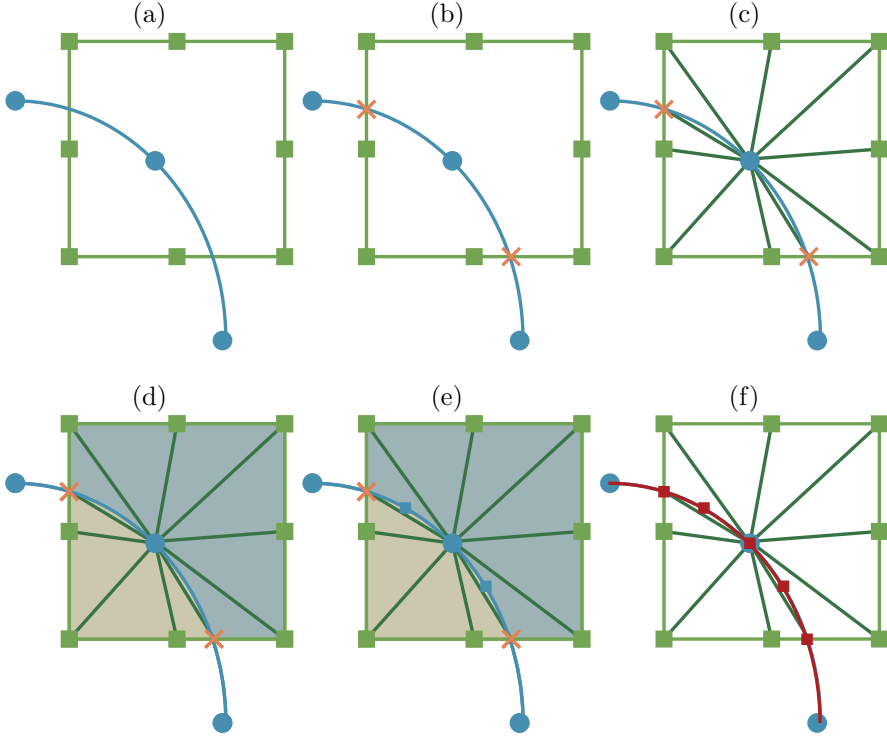


Figure 4.3: The process of finding the fluid and solid subdomain from the intersection of the solid boundary with the vertices of the fluid element, the initial situation is given in (a). First the intersection points \times are found (b). Then a Delaunay triangulation of solid \bullet and fluid \blacksquare nodes and intersection points is generated (c). The fluid and solid triangles are detected (d). Additional points \blacksquare are added to the triangle to make it quadratic (e). Finally sub-elements for spatial integration of the interface integrals are added, with corresponding end nodes \blacksquare (f).

4.1.2 Spatial integration

The weak form of the governing equations involves both domain and boundary integrals. The domain integrals are evaluated over the fluid domain. In

order to retain optimal convergence of the FEM, the integrals in the weak form have to be exactly evaluated for a given set of shape functions. In the FEM the domain integral is split into integrals over each element separately. The sum of all these integrals is the domain integral. Suppose the following integral has to be evaluated: $(a, b)_\Omega$, with functions $a(x, y)$ and $b(x, y)$. This becomes the sum over N elements: $(a, b)_\Omega = \sum_{i=1}^N (a, b)_{\Omega_i}$ where Ω_i is the domain of element i . In general this integral over Ω_i cannot be evaluated analytically and a numerical quadrature rule is used. In quadrature rules the integrand is evaluated at several points and the value of the integrand is multiplied with a weight. The position of the points, the amount of points and weight determine the accuracy of the rule. One of these numerical quadrature rules is Gauss quadrature, which is often used in FEM. For n points the 1D Gauss rule can evaluate a polynomial of order $2n - 1$ exactly [63]. The positions and weights for a given order of integrand are tabulated for reference domains. In order to use these tabulated Gauss rule, the integral has to be mapped to the reference domain, which means a coordinate transformation of the global coordinates (x, y) to the local coordinates (ξ, η) . In FEM the same shape functions are used for interpolating the variables as for mapping the coordinates, which is known as iso-parametric mapping. This yields : $(a(x, y), b(x, y))_{\Omega_i} = (a(\xi, \eta), b(\xi, \eta))J_{\Omega_{ref}}$, with $J = \det \mathbf{F}$ the determinant of the Jacobian matrix $\mathbf{F} = \frac{\partial \mathbf{x}}{\partial \boldsymbol{\xi}}$ with $\mathbf{x} = xe_x + ye_y$ and $\boldsymbol{\xi} = \xi e_\xi + \eta e_\eta$. Here Q_2Q_1 elements for the velocity-pressure are used. For a two dimensional problem with undeformed quadrilateral elements, this means that fourth order functions for the velocity are found. In case where a mass matrix $(\phi_i, \phi_j)_{\Omega_i} = (\mathcal{O}(\xi^4\eta^4))_{\Omega_i}$ is present, eighth-order functions are present and have to be evaluated exactly. In order to do this, a (3×3) Gauss rule (fifth order accurate in ξ and η) is used for the quadrilateral elements which are not intersected. This method only attains the required accuracy if the quadrilateral is not deformed. For the deformed quadratic sub-triangles used in XFEM, the exact evaluation of the mass matrix requires evaluation of functions of $\mathcal{O}(\xi^5\eta^4)$, leading to a 25 point integration rule which is tenth order accurate [64].

While the amount of degrees of freedom remains the same in both intersected and non-intersected elements, the amount of work required to obtain the element matrices and vectors differs a lot, due to larger amount of integration points in the intersected elements.

For the line integral similar reasoning holds and the same eighth order functions have to be integrated accurately, hence a five point Gauss rule is used for integration, yielding ninth order accuracy.

4.2 Weakly-applied Dirichlet boundary conditions

The equations of motion for the fluid and solid are defined in a different reference frame. The fluid is given in a fixed Eulerian reference frame, while the solid is given in a deforming Lagrangian reference frame. We would like that the discrete form of this set of equations is given in the same reference frames. This means that the discretization of the fluid domain does not move, while the discretization of the solid does.

Since the fluid mesh is fixed and the fluid-structure interface moves, this interface does not coincide with the element edges. Hence the fluid and solid do not have common nodes at which the interface conditions can be applied and other techniques have to be used.

In order to simplify matters, let us notice the following. If the restriction is made that the solid is not allowed to move at all, the problem is basically only a fluid problem, where the kinematic interface condition Eq. (2.11) becomes an essential boundary condition for the velocity, with value \mathbf{u}_{fs} and the dynamic interface condition Eq. (2.12) vanishes. In the following the inertial terms will be neglected, just for the sake of brevity. The fluid will also be considered to be Newtonian, so $\boldsymbol{\sigma} = 2\eta\mathbf{D} - p_f\mathbf{I}$. This leads to the following problem:

$$-\nabla \cdot \boldsymbol{\sigma} = \mathbf{0} \quad \text{in } \Omega_f, \quad (4.13)$$

$$\nabla \cdot \mathbf{u} = 0 \quad \text{in } \Omega_f, \quad (4.14)$$

$$\mathbf{u} = \mathbf{u}_{fs} \quad \text{on } \Gamma_{fs}, \quad (4.15)$$

$$\mathbf{u} = \mathbf{0} \quad \text{on } \Gamma_D. \quad (4.16)$$

The weak form of this set of equations is found after multiplying Eqs. (4.13) and (4.14) with test functions \mathbf{v}, q and integrating them over the entire fluid domain: Find $\mathbf{u} \in \mathcal{U}, p_f \in \mathcal{P}_f$ such that:

$$-(\mathbf{v}, \nabla \cdot \boldsymbol{\sigma})_\Omega - (q, \nabla \cdot \mathbf{u})_\Omega = 0 \quad \forall \mathbf{v} \in \mathcal{U}, q \in \mathcal{P}_f.$$

After applying partial integration to the first term an additional boundary term arises along the entire boundary Γ :

$$-(\mathbf{v}, \nabla \cdot \boldsymbol{\sigma})_\Omega = (\mathbf{D}_v, \boldsymbol{\sigma})_{\Omega_f} - (\mathbf{v}, \mathbf{n} \cdot \boldsymbol{\sigma})_\Gamma, \quad (4.17)$$

where $\mathbf{D}_v = \frac{1}{2}(\nabla \mathbf{v}^T + \nabla \mathbf{v})$ and \mathbf{n} is the outward facing normal on Γ . The last term in this equation is the traction at the boundary Γ . Since the traction is given on the part of the boundary where Neumann boundary conditions are applied Γ_N , this integral can be split into three parts:

$$(\mathbf{v}, \mathbf{n} \cdot \boldsymbol{\sigma})_\Gamma = (\mathbf{v}, \mathbf{t}_N)_{\Gamma_N} + (\mathbf{v}, \mathbf{n} \cdot \boldsymbol{\sigma})_{\Gamma_{fs}} + (\mathbf{v}, \mathbf{n} \cdot \boldsymbol{\sigma})_{\Gamma_D}, \quad (4.18)$$

where \mathbf{t}_N is the traction at the Neumann boundary. The last term is the traction at the Dirichlet boundary. It is common in the FEM to choose $\mathbf{v} = \mathbf{0}$ on the Dirichlet boundary, and we will do so accordingly. The last term then drops out and the final weak form reads:

Find $\mathbf{u} \in \mathcal{U}, p_f \in \mathcal{P}_f$:

$$\begin{aligned} (\mathbf{D}_v, \boldsymbol{\sigma})_{\Omega_f} - (\mathbf{v}, \mathbf{t}_N)_{\Gamma_N} - (\mathbf{v}, \mathbf{n} \cdot \boldsymbol{\sigma})_{\Gamma_{fs}} - (q, \nabla \cdot \mathbf{u})_{\Omega} &= 0 & (4.19) \\ \forall \mathbf{v} \in \mathcal{U}, q \in \mathcal{P}_f. \end{aligned}$$

The next step is finding a method for applying the essential boundary condition at Γ_{fs} on the system. We will consider three methods, the Lagrange multiplier method, the Gerstenberger-Wall scheme and our new scheme which is based on the Gerstenberger-Wall scheme.

4.2.1 Lagrange multiplier

In a Lagrange multiplier scheme the essential boundary condition is treated as a constraint on the system. Therefore an additional degree of freedom is added to the system for every condition to be enforced. These additional degrees of freedom are the Lagrange multipliers $\boldsymbol{\lambda}$ and their physical meaning will be determined later on.

Find $\mathbf{u} \in \mathcal{U}, p_f \in \mathcal{P}_f, \boldsymbol{\lambda} \in \mathcal{L}$:

$$(\mathbf{D}_v, \boldsymbol{\sigma})_{\Omega_f} - (\mathbf{v}, \mathbf{t}_N)_{\Gamma_N} + (\mathbf{v}, \boldsymbol{\lambda})_{\Gamma_{fs}} = 0 \quad (4.20)$$

$$- (q, \nabla \cdot \mathbf{u})_{\Omega} = 0 \quad (4.21)$$

$$(\boldsymbol{\mu}, \mathbf{u} - \mathbf{u}_{fs})_{\Gamma_{fs}} = 0 \quad (4.22)$$

$$\forall \mathbf{v} \in \mathcal{U}, q \in \mathcal{P}_f, \boldsymbol{\mu} \in \mathcal{L}.$$

This scheme has the following properties:

- The Lagrange multiplier can be identified as minus the boundary traction at Γ_{fs} .
- Since $\boldsymbol{\lambda}$ only exists on Γ_{fs} , it is quite natural to define it only on this boundary. So the fluid is discretized on the domain, and the Lagrange multiplier on the boundary. For stability reasons the discretization of the constraint cannot be chosen independently from the fluid discretization [54]. Since both are defined on a different geometry, finding a stable combination is difficult.
- The resulting system is symmetric.

4.2.2 Gerstenberger-Wall scheme

Recently Gerstenberger and Wall [39] have introduced a method for applying Dirichlet boundary conditions on boundaries which are not aligned with the element edges. Their method is based on the observation that the Lagrange multiplier in a Lagrange multiplier scheme can be identified as the traction. They therefore propose to introduce an extra stress variable $\hat{\boldsymbol{\sigma}}$ which is related to the Lagrange multiplier in the following way: $\mathbf{n} \cdot \hat{\boldsymbol{\sigma}} = -\boldsymbol{\lambda}$ and replace $\boldsymbol{\lambda}$ and $\boldsymbol{\mu}$ with $-\mathbf{n} \cdot \hat{\boldsymbol{\sigma}}$ and $-\mathbf{n} \cdot \hat{\mathbf{m}}$, with $\hat{\mathbf{m}}$ the new test function. Since $\hat{\boldsymbol{\sigma}}$ has more components than $\boldsymbol{\lambda}$, the resulting system is underdetermined. In order to make this additional stress variable unique they add an extra equation relating it to the rate of deformation tensor \mathbf{D} :

$$\left(\hat{\mathbf{m}}, \frac{\hat{\boldsymbol{\sigma}} + p_f \mathbf{I}}{2\eta} - \mathbf{D} \right)_{\Omega_f} + (\mathbf{n} \cdot \hat{\mathbf{m}}, \mathbf{u} - \mathbf{u}_{fs})_{\Gamma_{fs}} = 0 \quad (4.23)$$

Then the final weak form reads:

Find $\mathbf{u} \in \mathcal{U}, p_f \in \mathcal{P}_f, \hat{\boldsymbol{\sigma}} \in \mathcal{S}$:

$$(\mathbf{D}_v, \boldsymbol{\sigma})_{\Omega_f} - (\mathbf{v}, \mathbf{t}_N)_{\Gamma_N} - (\mathbf{v}, \mathbf{n} \cdot \hat{\boldsymbol{\sigma}})_{\Gamma_{fs}} = 0 \quad (4.24)$$

$$-(q, \nabla \cdot \mathbf{u})_{\Omega} = 0 \quad (4.25)$$

$$\left(\hat{\mathbf{m}}, \frac{\hat{\boldsymbol{\sigma}} + p_f \mathbf{I}}{2\eta} - \mathbf{D} \right)_{\Omega_f} + (\mathbf{n} \cdot \hat{\mathbf{m}}, \mathbf{u} - \mathbf{u}_{fs})_{\Gamma_{fs}} = 0 \quad (4.26)$$

$$\forall \mathbf{v} \in \mathcal{U}, q \in \mathcal{P}_f, \hat{\mathbf{m}} \in \mathcal{S}.$$

The properties of this scheme are:

- The new Lagrange multiplier $\hat{\boldsymbol{\sigma}}$ is defined on the domain thus finding a stable combination is easier than with the original Lagrange multiplier scheme.
- Since an extra stress is added to the system, this method can be seen as a mixed method.
- The system is asymmetric. It cannot be made symmetric, due to the presence of the pressure term in the last equation.
- The extra stress tensor can be defined only in the elements containing Γ_{fs} if their approximation space is discontinuous and encompasses the function space of $\boldsymbol{\sigma}$. If it is defined locally, it can be eliminated from the system by inverting it locally, thus reducing the size of the final system.
- The method shows optimal convergence of pressure and velocity for both continuous as well as discontinuous discretization of $\hat{\boldsymbol{\sigma}}$ [39].

- In order to make $\hat{\boldsymbol{\sigma}}$ unique the constitutive relation of the fluid has to be inverted. This is possible for linear constitutive relations, but may be difficult or even impossible for non-linear relations and relations involving an extra evolution equation. Since both the generalized Newtonian and viscoelastic models proposed in Chapter 2 belong to this class, the applicability of this scheme is uncertain.

Due to the latter property we propose an adaptation to the model, which renders the use of non-linear and viscoelastic fluid models possible.

4.2.3 Modified Gerstenberger-Wall for non-linear constitutive relations

The Gerstenberger-Wall scheme for weakly imposing Dirichlet boundary conditions is adapted such that it can be used with a wider range of constitutive relations. This adaptation was shown to work in a recent paper of Baltussen *et al.* [61]. By adding an extra rate of deformation tensor \mathbf{E} to the system instead of the stress tensor $\hat{\boldsymbol{\sigma}}$, the inversion of the constitutive relation is avoided and the system reads:

Find $\mathbf{u} \in \mathcal{U}, p_f \in \mathcal{P}_f, \mathbf{E} \in \mathcal{E}$:

$$(\mathbf{D}_v, \boldsymbol{\sigma})_{\Omega_f} - (\mathbf{v}, \mathbf{t}_N)_{\Gamma_N} - (\mathbf{v}, \mathbf{n} \cdot (2\eta\mathbf{E} - p_f\mathbf{I}))_{\Gamma_{fs}} = 0, \quad (4.27)$$

$$-(q, \boldsymbol{\nabla} \cdot \mathbf{u})_{\Omega} = 0, \quad (4.28)$$

$$(\mathbf{H}, \mathbf{E} - \mathbf{D})_{\Omega_f} + (\mathbf{n} \cdot \mathbf{H}, \mathbf{u} - \mathbf{u}_{fs})_{\Gamma_{fs}} = 0 \quad (4.29)$$

$$\forall \mathbf{v} \in \mathcal{U}, q \in \mathcal{P}_f, \mathbf{H} \in \mathcal{E}.$$

The next step is to replace \mathbf{E} in the boundary traction term with \mathbf{D} and add an extra term to compensate for this:

$$\begin{aligned} & \dots - (\mathbf{v}, \mathbf{n} \cdot (2\eta\mathbf{E} - p_f\mathbf{I}))_{\Gamma_{fs}} = \\ & \dots - (\mathbf{v}, \mathbf{n} \cdot (2\eta\mathbf{D} - p_f\mathbf{I}))_{\Gamma_{fs}} + (\mathbf{v}, \mathbf{n} \cdot 2\eta(\mathbf{E} - \mathbf{D}))_{\Gamma_{fs}} \end{aligned} \quad (4.30)$$

where the first term on the right is the traction on the boundary in the original variables \mathbf{u} and p_f and the second term is a viscous traction term which is only non-zero due to the different discretization of \mathbf{E} and \mathbf{D} . In order to use this method for non-Newtonian fluids, which are usually not written as a function of \mathbf{D} we propose the following. The first term is computed with the non-Newtonian constitutive relation, and the second term is retained, where η is replaced by the viscosity-like parameter κ . The second term can now be regarded as a stabilization term with parameter κ . For a Newtonian fluid and $\kappa = \eta$ the scheme is exactly the same as the Gerstenberger-Wall scheme. The extra rate of deformation tensor \mathbf{E} can be eliminated from the system by solving Eq. (4.29):

$$\mathbf{E}_i = \sum_j M_{ij}^{-1} \left((\phi_i, \mathbf{D})_{\Omega_f} - \frac{1}{2} (\mathbf{n}\phi_j, \mathbf{n}[\mathbf{u} - \mathbf{u}_{fs}] + [\mathbf{u} - \mathbf{u}_{fs}]\mathbf{n})_{\Gamma_{fs}} \right) \quad (4.31)$$

where M_{ij}^{-1} is the inverse of the mass matrix $M_{ij} = (\phi_i, \phi_j)_{\Omega_f}$. The shapefunctions ϕ have been defined for the interpolation of \mathbf{E} . By using locally defined shapefunctions, the mass matrix is defined on each element separately and can be inverted on element level. By replacing all occurrences of $\mathbf{E} = \sum_{i=1}^N \phi_i \mathbf{E}_i$ with the expression in Eq. (4.31), the system becomes:

Find $\mathbf{u} \in \mathcal{U}, p_f \in \mathcal{P}_f$:

$$\begin{aligned} & (\mathbf{D}_v, \boldsymbol{\sigma})_{\Omega_f} - (\mathbf{v}, \mathbf{t}_N)_{\Gamma_N} - (\mathbf{v}, \mathbf{n} \cdot (2\eta \mathbf{D} - p_f \mathbf{I}))_{\Gamma_{fs}} + \\ & \quad \left((\mathbf{v}, \mathbf{n} \cdot 2\kappa (\mathbf{D} - \phi_i M_{ij}^{-1} ((\phi_i, \mathbf{D})_{\Omega_f} - \right. \\ & \quad \left. \frac{1}{2} (\phi_j, \mathbf{n} [\mathbf{u} - \mathbf{u}_{fs}] + [\mathbf{u} - \mathbf{u}_{fs}] \mathbf{n})_{\Gamma_{fs}})) \right)_{\Gamma_{fs}} - \\ & \quad (q, \boldsymbol{\nabla} \cdot \mathbf{u})_{\Omega} = 0 \end{aligned} \tag{4.32}$$

$\forall \mathbf{v} \in \mathcal{U}, q \in \mathcal{P}_f.$

If ϕ_i is chosen such that it fully encompasses the shapefunctions of \mathbf{u} , then the projection of \mathbf{D} on the space of \mathbf{E} , which is the term $\phi_i [M_{ij}^{-1} ((\phi_j, \mathbf{D})_{\Omega_f})]$ becomes $\phi_i \mathbf{D}_i = \mathbf{D}$. For the velocity-pressure we use $Q_2^9 Q_1^4$ elements of the Taylor-Hood family, and for \mathbf{E} we use $Q_2^{9,d}$, which fully encompasses the Q_2 interpolation of the velocity. In this case, only the boundary term remains and the final set of equations becomes: Find $\mathbf{u} \in \mathcal{U}, p_f \in \mathcal{P}_f$:

$$\begin{aligned} & (\mathbf{D}_v, \boldsymbol{\sigma})_{\Omega_f} - (\mathbf{v}, \mathbf{t}_N)_{\Gamma_N} - (\mathbf{v}, \mathbf{n} \cdot (2\eta \mathbf{D} - p_f \mathbf{I}))_{\Gamma_{fs}} + \\ & \sum_i \sum_j M_{ij}^{-1} (\mathbf{v} \mathbf{n}, \kappa \phi_i)_{\Gamma_{fs}} : (\phi_j, \mathbf{n} [\mathbf{u} - \mathbf{u}_{fs}] + [\mathbf{u} - \mathbf{u}_{fs}] \mathbf{n})_{\Gamma_{fs}} = 0, \end{aligned} \tag{4.33}$$

$$\begin{aligned} & - (q, \boldsymbol{\nabla} \cdot \mathbf{u})_{\Omega} = 0 \\ & \quad \forall \mathbf{v} \in \mathcal{U}, q \in \mathcal{P}_f. \end{aligned} \tag{4.34}$$

In this final form the stabilization term with factor κ has a remarkable resemblance with the stabilization term in Nitsche's method [65]: $C (\mathbf{v}, \mathbf{u} - \mathbf{u}_{fs})_{\Gamma_{fs}}$, where C is a stabilization parameter which depends on the problem and the mesh. The major advantages of the method presented here are:

- For Newtonian fluids the stabilization parameter κ has a physical meaning, namely the viscosity, whereas C has not.
- Stabilization automatically scales with the length over volume ratio of the elements containing boundaries, whereas complicated eigenvalue analysis is needed to get the same scaling behavior for Nitsche's method [66].

4.2.4 Fluid solid interaction

In the previous sections several methods for enforcing Dirichlet boundary conditions on the fluid domain were proposed. With one of these methods the

kinematic interface condition Eq. (2.11) is enforced on the fluid and solid. The dynamic interface condition Eq. (2.12), is not enforced by this method however. The weak form of the fluid-structure interaction problem is found by using the weak form of the momentum and continuity balance of the fluid, Eqs. (4.27)-(4.29) and applying Eq. (4.30). For the solid part Eqs. (2.3)-(2.4) are multiplied with a test function and partially integrated where necessary. In the weak Dirichlet boundary condition, the value for \mathbf{u}_{fs} is replaced by $\dot{\mathbf{d}}$.

Find $\mathbf{u} \in \mathcal{U}, p_f \in \mathcal{P}_f, \mathbf{E} \in \mathcal{E}, \mathbf{d} \in \mathcal{D}, p_s \in \mathcal{P}_s$ such that:

$$(\mathbf{D}_v, \boldsymbol{\sigma}_f)_{\Omega_f} - (\mathbf{v}, \mathbf{n}_f \cdot \boldsymbol{\sigma}_f)_{\Gamma_f} + (\mathbf{v}, \mathbf{n}_f \cdot 2\kappa(\mathbf{E} - \mathbf{D}))_{\Gamma_{\text{fs}}} = 0, \quad (4.35)$$

$$- (q_f, \nabla \cdot \mathbf{u})_{\Omega_f} = 0, \quad (4.36)$$

$$(\mathbf{H}, \mathbf{E} - \mathbf{D})_{\Omega_f} + \left(\mathbf{n}_f \cdot \mathbf{H}, \mathbf{u} - \dot{\mathbf{d}} \right)_{\Gamma_{\text{fs}}} = 0, \quad (4.37)$$

$$(\mathbf{D}_w, \boldsymbol{\sigma}_s)_{\Omega_s} - (\mathbf{w}, \mathbf{n}_s \cdot \boldsymbol{\sigma}_s)_{\Gamma_s} = 0, \quad (4.38)$$

$$(q_s, \det(\mathbf{F}) - 1)_{\Omega_s} = 0, \quad (4.39)$$

$$\forall \mathbf{v} \in \mathcal{U}, q \in \mathcal{P}_f, \mathbf{H} \in \mathcal{E}, \mathbf{w} \in \mathcal{D}, r \in \mathcal{P}_s.$$

The dynamic interface condition $\mathbf{n}_f \cdot \boldsymbol{\sigma}_f + \mathbf{n}_s \cdot \boldsymbol{\sigma}_s = \mathbf{0}$ is enforced by replacing the traction term in the momentum equation of the solid by minus the traction on the fluid. The traction on the fluid has two components, the traction coming from the constitutive relation and the traction due to stabilization. Hence the final weak form reads:

Find $\mathbf{u} \in \mathcal{U}, p_f \in \mathcal{P}_f, \mathbf{E} \in \mathcal{E}, \mathbf{d} \in \mathcal{D}, p_s \in \mathcal{P}_s$ such that:

$$(\mathbf{D}_v, \boldsymbol{\sigma}_f)_{\Omega_f} - (\mathbf{v}, \mathbf{n}_f \cdot \boldsymbol{\sigma}_f)_{\Gamma_f} + (\mathbf{v}, \mathbf{n}_f \cdot 2\kappa(\mathbf{E} - \mathbf{D}))_{\Gamma_{\text{fs}}} = 0, \quad (4.40)$$

$$- (q_f, \nabla \cdot \mathbf{u})_{\Omega_f} = 0, \quad (4.41)$$

$$(\mathbf{H}, \mathbf{E} - \mathbf{D})_{\Omega_f} + \left(\mathbf{n}_f \cdot \mathbf{H}, \mathbf{u} - \dot{\mathbf{d}} \right)_{\Gamma_{\text{fs}}} = 0, \quad (4.42)$$

$$(\mathbf{D}_w, \boldsymbol{\sigma}_s)_{\Omega_s} - (\mathbf{w}, \mathbf{n}_s \cdot \boldsymbol{\sigma}_s)_{\Gamma_s} +$$

$$(\mathbf{w}, \mathbf{n}_f \cdot \boldsymbol{\sigma}_f)_{\Gamma_{\text{fs}}} - (\mathbf{w}, \mathbf{n}_f \cdot 2\kappa(\mathbf{E} - \mathbf{D}))_{\Gamma_{\text{fs}}} = 0, \quad (4.43)$$

$$(q_s, \det(\mathbf{F}) - 1)_{\Omega_s} = 0, \quad (4.44)$$

$$\forall \mathbf{v} \in \mathcal{U}, q \in \mathcal{P}_f, \mathbf{H} \in \mathcal{E}, \mathbf{w} \in \mathcal{D}, r \in \mathcal{P}_s.$$

The extra variables \mathbf{E} can be eliminated from the system as was described in Section 4.2.3. Recently the Gerstenberger-Wall scheme was also adapted for fluid-structure interaction by Mayer *et al.* [34]. They used the standard Gerstenberger-Wall formulation for imposing the kinematic interface condition, and enforced the dynamic interface condition by replacing the traction on the solid by the traction on the fluid, as we did. The major difference, as with the original Gerstenberger-Wall scheme, remains that in our case the extra variable is chosen as the rate of deformation tensor, instead of the Cauchy stress tensor. Hence the constitutive relation of the fluid does not have to be

inverted. In addition, our scheme with the stabilization term scaling with κ can be used for non-Newtonian fluid models.

4.3 Mesh moving schemes

In the previous sections a numerical method for solving fluid-structure interaction problems with fixed fluid grids was introduced. This method is validated by comparing it with an ALE scheme for fluid-structure interaction. ALE which stands for Arbitrary Lagrange Euler, which is the most widely used method for fluid-structure interaction having small deformations and requires the motion of the fluid grid in such a manner that Γ_{fs} remains a boundary of both the fluid as the solid mesh. Since this method requires a body-fitted fluid mesh which moves in time, it is referred to as the moving body-fitted mesh (MBFM). The major disadvantage of the XFEM approach given in the previous sections is that convective and time-dependent terms in the fluid domain cannot be treated in a fully Eulerian manner. Since the shape of the fluid domain changes in time, the fluid field variables are not constantly available in all points of the domain. This poses a problem for finite-difference based time integration schemes, where these field variables are supposed to be known at all positions and at all times. In Subsection 4.3.2 a remedy to this problem will be introduced. It requires the convection of the field variables with an ALE method.

4.3.1 MBFM

The method for modeling fluid-structure interaction will be validated by comparing it with a moving body-fitted mesh (MBFM), which is basically an ALE method. In this method the fluid mesh is allowed to move in an arbitrary manner. The fluid solid interface is always a common boundary of the fluid and solid mesh, hence the velocities are always continuous. For the set of equations Eqs. (2.1-2.4) and neglecting solid inertia it reads:

$$\rho \left(\frac{\delta \mathbf{u}}{\delta t} + (\mathbf{u} - \mathbf{u}_{\text{mesh}}) \cdot \nabla \mathbf{u} \right) = \nabla \cdot \boldsymbol{\sigma}_f \quad \text{in } \Omega_f, \quad (4.45)$$

$$\nabla \cdot \mathbf{u} = 0 \quad \text{in } \Omega_f, \quad (4.46)$$

$$-\nabla \cdot \boldsymbol{\sigma}_s = \mathbf{f}_s \quad \text{in } \Omega_s, \quad (4.47)$$

$$\det(\mathbf{F}) = 1 \quad \text{in } \Omega_s, \quad (4.48)$$

where the fluid mesh velocity \mathbf{u}_{mesh} is introduced. The adaptation of the convective term with \mathbf{u}_{mesh} should be applied on every occurrence, so also in the constitutive relation for the viscoelastic case.

The mesh displacement \mathbf{d}_{mesh} is defined by solving a Poisson's equation

$\nabla^2 \mathbf{d}_{\text{mesh}} = 0$ on the fluid domain having the following boundary conditions:

$$\mathbf{d}_{\text{mesh}}(\mathbf{x}) = \begin{cases} \mathbf{d} & \forall \mathbf{x} \in \Gamma_{\text{fs}}, \\ 0 & \forall \mathbf{x} \notin \Gamma_{\text{fs}}, \end{cases} \quad (4.49)$$

where \mathbf{d} the solid displacement. By applying these boundary conditions the fluid mesh exactly follows the solid mesh at Γ_{fs} , and has smooth gradients, thus avoiding highly distorted elements.

The fluid mesh velocity is related to the fluid mesh displacement by the following kinematic relation:

$$\mathbf{u}_{\text{mesh}} = \frac{\delta \mathbf{d}_{\text{mesh}}}{\delta t}. \quad (4.50)$$

The time derivative of the mesh displacement, $\frac{\delta \mathbf{d}_{\text{mesh}}}{\delta t}$, is treated with a first-order implicit Euler scheme, see Section A.1 in Appendix A.

Since the interface conditions are enforced in a strong form, either the fluid velocity or the solid displacement could be eliminated from the system at Γ_{fs} , thus reducing the amount of variables. This requires having different elements on the interface. Instead of defining new elements, we make use of a Lagrange multiplier to enforce the kinematic interface condition Eq. (2.11) via point collocation which requires some extra degrees of freedom.

Please note that in case of the Stokes equation it is not required to compute the mesh velocity from the mesh displacement, since inertial terms are absent. If however a viscoelastic fluid is modeled the mesh velocity has to be computed, since the convective derivative in the constitutive relation does not vanish.

4.3.2 XFEM-ALE

In the derivation of the weak interface conditions the fluid was considered to be inertialess, hence no time dependent and convective terms were present in the fluid's momentum equation. If this term is included and discretized in time (see A.1)¹, the following term arises in the momentum equation of the fluid:

$$\rho \frac{\mathbf{u}^{i+1} - \mathbf{u}^i}{\Delta t} \dots \quad (4.51)$$

where i and $i + 1$ denote the velocity at the previous and current time step respectively. Since the fluid is solved on an Eulerian grid, this requires that \mathbf{u}^{i+1} has to be known everywhere in the current domain Ω_{f}^{i+1} . This is the case for problems with stationary boundaries, since $\Omega_{\text{f}}^{i+1} = \Omega_{\text{f}}^i$. If the boundaries are not stationary, such as in fluid-structure interaction, $\Omega_{\text{f}}^{i+1} \neq \Omega_{\text{f}}^i$, \mathbf{u}^i is not known everywhere. This problem is also shown schematically in Figure 4.4.

¹Here the implicit Euler scheme is used, but this problem arises with every finite difference time stepping scheme

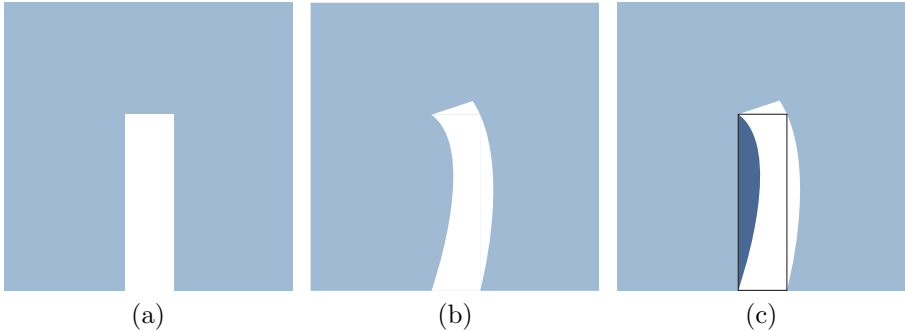


Figure 4.4: The fluid domain Ω_f at t^i (a), at t^{i+1} and the resulting indicated region where no information on \mathbf{u}^i is present.

There are basically two solutions to this problem, which is common to all XFEM problems with moving boundaries and time dependent governing equations. The first is using space-time elements for the total problem [67], thus abandoning the finite difference time discretization and using time as an additional dimension. Although this method is very elegant, since it circumvents all the problems with time integration altogether, it also requires a different approach to the implementation of XFEM. We therefore opt to use, the less elegant, but equally adequate method of convecting the variables at Ω_f^i to Ω_f^{i+1} . This requires the deformation of Ω_f^i in such a way that the boundaries exactly match Ω_f^{i+1} , which is graphically depicted in Figure 4.5. This method is basically applying ALE at every timestep, thus the machinery developed for ALE can be used immediately without much adaptation. The deformation applied to the mesh of Ω_f^i can be the real deformation during a time step (Lagrange), or an artificial deformation which sole purpose is to align the boundaries at t^{i+1} . The latter has successfully been used by Choi *et al.* [62], where the deformations during a time step were small. They compute the mesh deformation by solving a Poisson problem, which has the boundary movement as essential boundary condition. Since only information from t^{i-1} has to be transported to t^{i+1} , the mesh is only deformed with the deformation during these two time steps. Hence the deformation is relatively small and the elements are only slightly distorted.

Here we employ the scheme of Choi *et al.* [62], with a small modification. We will use the current mesh as the reference point, whereas Choi used the mesh at the previous timestep as the reference point. The advantage of the method used here is that only the value of the essential boundary condition changes for each mesh deformation, hence the matrix resulting from the discretized system remains unchanged. Therefore solution of this system is fast,

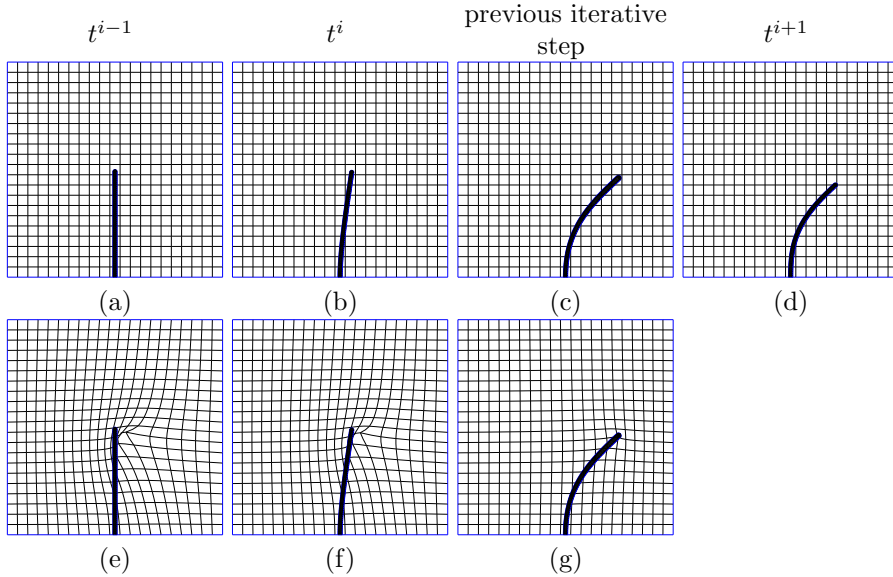


Figure 4.5: The XFEM mesh (top) at t^{i-1} (a), t^i (b), previous iteration (c) and t^{i+1} (d) and the ALE meshes (bottom) having a displacement from t^{i+1} to t^{i-1} (e), to t^i (f) and to the mesh at the previous iteration (g).

as the LU-decomposition of this matrix can be stored and used repetitively. Since Γ_{fs} moves through the fixed fluid mesh, the essential boundary terms for the Poisson's equation cannot be imposed in the standard way, *e.g.* by splitting the system into known and unknown degrees of freedom and elimination of the former. Here we will use the weakly imposed boundary conditions which we also used for enforcing essential and interface conditions in the previous section. The derivation follows similar lines and can be found in Appendix C. This results in the following weak set of equations to be solved: Find $\mathbf{d}_{\text{mesh}} \in \mathcal{D}_{\text{mesh}}$ such that:

$$\left(\nabla \mathbf{k}^T, \nabla \mathbf{d}_{\text{mesh}} \right)_{\Omega} - (\mathbf{k}, \mathbf{n} \cdot \nabla \mathbf{d}_{\text{mesh}})_{\Gamma_{\text{fs}}} + \sum_i \sum_j M_{ij}^{-1} (\mathbf{k} \mathbf{n}, \kappa \phi_i)_{\Gamma_{\text{fs}}} : (\phi_j, \mathbf{n} [\mathbf{d} - \mathbf{d}_{\text{mesh}}] + [\mathbf{d} - \mathbf{d}_{\text{mesh}}] \mathbf{n})_{\Gamma_{\text{fs}}} = 0 \quad (4.52)$$

$$\forall \mathbf{k} \in \mathcal{D}_{\text{mesh}}.$$

The Poisson equation is solved in the entire fixed fluid domain, so the fluid “insid” the solid is also taken into account. The mesh movement is thus solved with a fictitious domain technique. By taking into account the fluid mesh inside the solid, the fluid mesh deformation remains smooth.

4.4 Solution procedure

A multi physics problem such as fluid-structure interaction can be solved together, known as the fully coupled approach or monolithic approach, or the individual problems (fluid and solid) can be solved individually where the interface conditions are used to transfer information from one problem to another. This is known as a decoupled approach. The former has the advantage that it is more stable, at the cost of solving a larger system. The latter has the advantage that specialized packages can be used for each subproblem and coupling is relatively easy since it only involves prescribing boundary conditions. The major drawback of this method is that it is only stable for problems with a stiff solid and/or a very low viscous fluid. The stability of the decoupled approach can be illustrated by the following example.

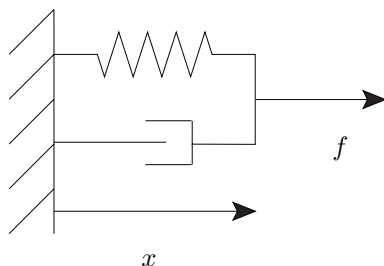


Figure 4.6: A simple fluid-solid interaction model with a dashpot(fluid) and a spring(solid) in parallel.

Example. 1. Consider a spring and dashpot in parallel, connected on one side to a wall and on the other side a force acts upon the system, see Figure 4.6. The spring represents the solid and the dashpot the fluid. This is a simple model for fluid solid interaction neglecting inertia. For this system the governing equation reads:

$$kx + d\dot{x} = f,$$

where k is the stiffness of the spring, x is the displacement, d is the damping coefficient of the dashpot, \dot{x} is the velocity and f is the applied force, which is constant in time. The initial condition is $x(t = 0) = x_0$. Since the problem is time dependent we use an Euler backward time integration scheme, which leads to the following system:

$$kx^{i+1} + d\frac{x^{i+1} - x^i}{\Delta t} = f.$$

For the fully coupled approach the solution reads: $x^{i+1} = \frac{f + \frac{d}{\Delta t}x^i}{k + \frac{d}{\Delta t}}$. For stability analysis the growth factor λ is defined as $x^{i+1} = \lambda x^i$, where $\lambda < 1$ for the system to be stable. In the fully coupled case $\lambda = \frac{\frac{d}{\Delta t}}{k + \frac{d}{\Delta t}}$, which is always smaller than one for $k, d, \Delta t > 0$, hence the scheme is unconditionally stable and any desired temporal accuracy can be obtained. In the decoupled approach the system is split up into two subproblems, for instance the following two:

$$\begin{aligned} x_{j+1}^{i+1} &= \frac{f - f_j}{k}, \\ f_{j+1} &= d \frac{x_{j+1}^{i+1} - x^i}{\Delta t}, \end{aligned} \quad (4.53)$$

where the subscript j indicates the j -th iterative step. The stability of the iterative scheme can be ascertained in a similar way as in the previous paragraph by computing $x_{j+1}^{i+1} = \lambda x_j^{i+1}$. In this case $\lambda = \frac{d}{\Delta t k} < 1$, which is only valid if $\Delta t > \frac{d}{k}$, hence there exists a *minimal* time step $\Delta t_{\min} = \frac{d}{k}$ for stability, while there exists a maximal time step for accuracy Δt_{\max} . If $\Delta t_{\min} > \Delta t_{\max}$ the system can be solved with the desired accuracy. This is usually the case for stiff elastic bodies and problems where the viscous forces are low $\frac{d}{k} \ll 1$. If $\Delta t_{\min} < \Delta t_{\max}$ however, the system is not stable for the desired temporal accuracy. This is the case for elastic bodies with low stiffness and large viscous forces $\frac{d}{k} \geq 1$. So for these systems the decoupled approach fails and a fully coupled approach has to be used.

Similar behavior is also caused when inertial forces are important in the fluid and/or solid. This leads to the so called "added mass effect", which also causes a restriction on the minimal time step, if the system is solved in a decoupled manner and not handled appropriately [68]. Although several more stable decoupling approaches have been developed [29, 32, 69], we opt for a fully coupled approach, since artificial cilia have a low geometrical stiffness and are easily deformed by flow.

4.4.1 Approximation spaces

The approximation spaces $\mathcal{U}, \mathcal{P}_f, \mathcal{D}, \mathcal{P}_s, \mathcal{E}$ have not be introduced. Due to compatibility conditions for incompressible fluid flow the discrete approximation spaces $\mathcal{U}, \mathcal{P}_f$ are defined as:

$$\begin{aligned}\mathcal{U} &= \mathbf{u} \in H_0^1(\Omega_f) : \mathbf{u}|_{\Omega_{f,h}} \in Q_2^9(\Omega_{f,h}), \\ \mathcal{P}_f &= p_f \in L_0^2(\Omega_f) : p_f|_{\Omega_{f,h}} \in Q_1^4(\Omega_{f,h}),\end{aligned}\tag{4.54}$$

where Ω_f is the union of fluid elements $\Omega_{f,h}$. For the approximation spaces of the equations of motion of the solid, which is also incompressible, a similar combination is chosen:

$$\begin{aligned}\mathcal{D} &= \mathbf{d} \in H_0^1(\Omega_s) : \mathbf{d}|_{\Omega_{s,h}} \in Q_2^9(\Omega_{s,h}), \\ \mathcal{P}_s &= p_s \in L_0^2(\Omega_s) : p_s|_{\Omega_{s,h}} \in Q_1^4(\Omega_{s,h}),\end{aligned}\tag{4.55}$$

where Ω_s is the union of solid elements $\Omega_{s,h}$. The spaces Q_a^b is defined on a quadrilateral element in two dimensions as:

$$Q_a^b = v : v(x, y) = \sum_{i,j=0}^a c_{i,j} x^i y^j \text{ on each element}\tag{4.56}$$

where b denotes the number of degrees of freedom in the element. The approximation of \mathcal{E} is chosen discontinuous, in order to eliminate this variable locally. Hence

$$\mathcal{E} = E \in H_0^1(\Omega_f) : \mathbf{E}|_{\Omega_{f,h}} \in Q_2^{9,d}(\Omega_{f,h}).$$

4.5 Test problems

The methods described in the previous sections will be tested in several problems. First XFEM in combination with weakly imposed boundary conditions will be tested for flow of a Newtonian fluid around a cylinder. The next problem will be fluid-structure interaction with a Newtonian fluid without and with fluid inertia.

4.5.1 Flow around a cylinder

The flow around a cylinder in a channel will be studied. The channel is periodic and shown in Figure 4.7. For the flow of a Newtonian fluid around a cylinder

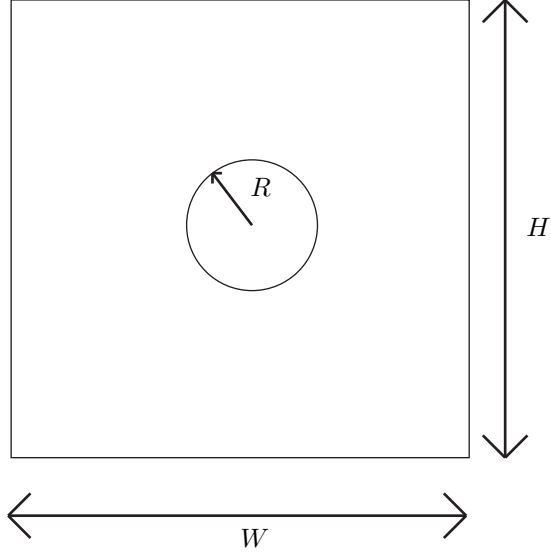


Figure 4.7: Periodic domain for flow around a cylinder, with radius R , height $H = 10R$ and width $W = 10R$.

with radius R the following solution is known:

$$\begin{aligned}
 \hat{u}_x &= \frac{(R^2 - r^2) \cos^2 \theta + r^2 \ln(r/R) + (1/2)(r^2 - R^2)}{r^2}, \\
 \hat{u}_y &= \frac{(R^2 - r^2) \cos \theta \sin \theta}{r^2}, \\
 \hat{p}_f &= \frac{-2 \cos \theta}{r} + 10,
 \end{aligned} \tag{4.57}$$

where (r, θ) are polar coordinates originating at the center of the cylinder. The radius is taken to be 0.2 which results in $(H, L) = (2, 2)$. The boundary conditions on the square domain are taken as the exact solution of Eq. (4.57) and are imposed in a strong manner. The no-slip boundary condition on the cylinder wall is imposed weakly with the modified Gerstenberger-Wall scheme, as described in Subsection 4.2.3. The pressure is prescribed in the lower left corner of the domain. For convergence analysis the following relative L^2 error

norms are defined:

$$\epsilon_{L^2, \mathbf{u}} = \frac{\left(\int_{\Omega_f} \|\mathbf{u} - \hat{\mathbf{u}}\|^2 dx \right)^{1/2}}{\left(\int_{\Omega_f} \|\hat{\mathbf{u}}\|^2 dx \right)^{1/2}}, \quad (4.58)$$

$$\epsilon_{L^2, p_f} = \frac{\left(\int_{\Omega_f} \|p_f - \hat{p}_f\|^2 dx \right)^{1/2}}{\left(\int_{\Omega_f} \|\hat{p}_f\|^2 dx \right)^{1/2}}. \quad (4.59)$$

The mesh is uniform and consists of square elements with size h . If $\kappa = \eta$, the original Gerstenberger-Wall scheme is found. For this scheme the errors are plotted versus h , and show optimal convergence as seen in Figure (4.8). In

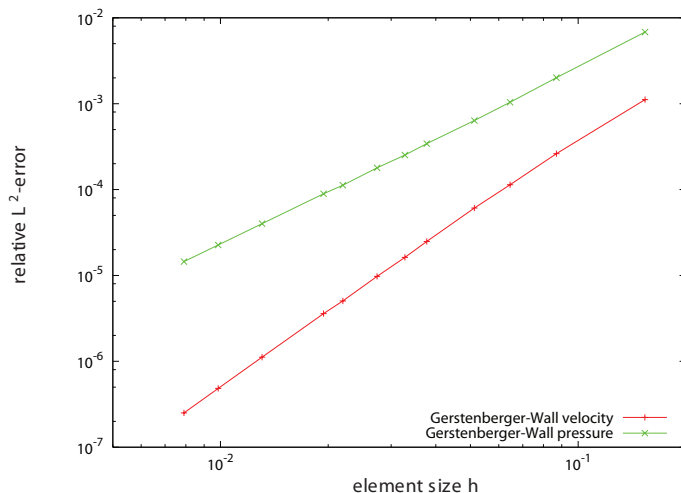


Figure 4.8: The relative L^2 errors for the velocity and pressure versus the size of an element h .

the modified Gerstenberger-Wall scheme an additional stability parameter κ is introduced. By computing the relative L^2 errors in the velocity and pressure for $h = 0.0377$ for different ratios of κ/η , the sensitivity of the solution to κ/η can be assessed. The result is shown in Figure 4.9. From this figure it can be seen that for $10^{-1} < \kappa/\eta < 200$, the solution is accurate and stable. Both for smaller and larger ratios the solution is inaccurate and shows wiggles. It is also clear that the optimum value is $\kappa/\eta = 1$, and that low ratios should be avoided, since the error increases rapidly below $\kappa/\eta = 0.1$. This is a promising result, since it shows that accurate solutions can be found, independent of the real viscosity or even the real constitutive behavior, which may not show a constant viscosity along the boundary.

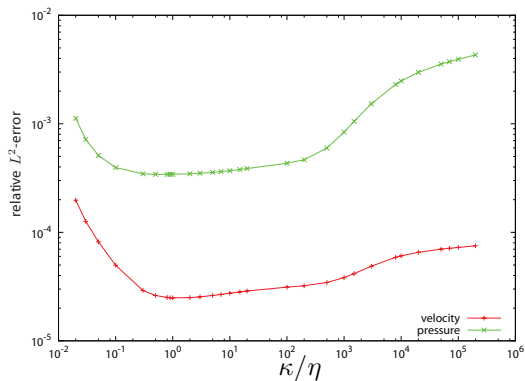


Figure 4.9: The relative L^2 error norms in velocity and pressure for different κ/η .

4.5.2 Pressure drop over an elastic beam

A pressure drop Δp is applied over an elastic beam in a square channel, see Figure 4.10. The pressure drop is applied through Neumann boundary conditions on the left and right boundary. In order to avoid singularities in the fluid stress near the tips of the beam, the top is rounded off with a radius of 0.0099. This value leaves a small straight section at the top of the cilium, which was required for meshing. Both MBFM and XFEM are used to solve the problem. The MBFM scheme is used as a reference solution against which the XFEM solution is compared. The solution will be compared on Γ_{fs} . The deformation

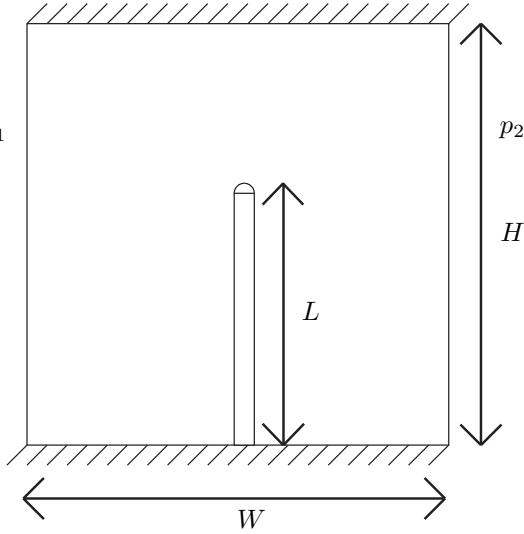


Figure 4.10: A pressure drop $\Delta p = p_1 - p_2$ over a beam of length $L = 0.5H$ in channel with height H and length W . The thickness of the beam is $0.02H$.

of the beam is relatively small (the tip deflection is less than $0.01H$), so the mesh in the ALE scheme is still well-posed. The velocity components, pressure and shear-stress components are compared for different mesh densities after ten timesteps at $t = 10^{-3}$ s. The viscosity of the fluid is 1 mPas, the modulus of the cilium is 1 MPa and the applied pressure drop $\Delta p = 10$ Pa. The XFEM mesh is regular with N elements in x and y -direction. The coarsest ALE mesh is shown in Figure 4.11.

The resulting velocity, pressure and shear-stress are given in Figure 4.12 for $N = 101, 201, 301$ for XFEM and MBFM as a reference solution. For the two most refined XFEM meshes, the x -velocity, pressure and shear-stress are very similar to the MBFM reference solution. Only for the coarsest mesh significant differences exist in the pressure and in the vorticity, where some sharp peaks appear. This verifies that the XFEM method with weakly imposed interface conditions results in the same solution as the MBFM for sufficiently refined meshes.

4.5.3 Pressure driven flow over a beam with fluid inertia

The flow over an elastic beam with fluid inertia is considered. The domain remains unchanged and is given in Figure 4.10. The startup of flow will be simulated both by MBFM and XFEM-ALE. The fluid is initially in rest $\mathbf{u} = \mathbf{0}$, and the following parameters are used in the computation: $\Delta p = 10$ Pa, $\eta = 10^{-3}$ Pa s, $\rho = 10^3$ kg m³ and the height of the channel is 1 cm. The velocity

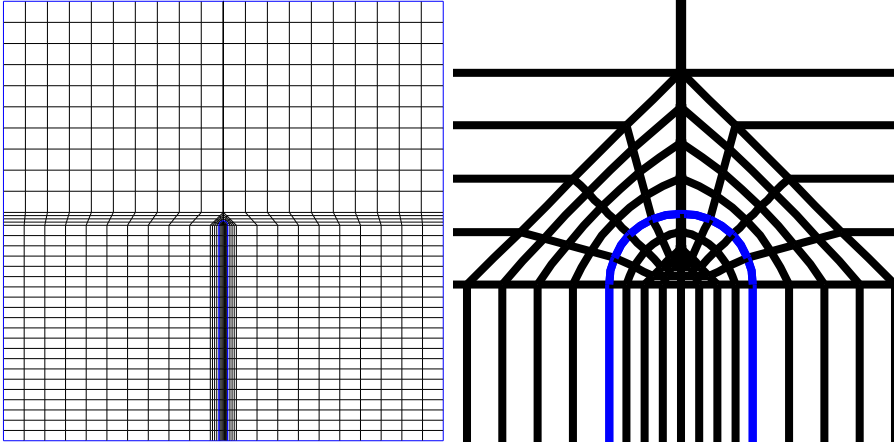


Figure 4.11: The coarsest ALE mesh, with a zoomed in view of the region around the tip of the rounded beam. The boundary of the solid is given in blue.

is estimated by scaling the instationary inertial term with the pressure drop in the momentum equation of the fluid, which is valid as long as the viscous forces are smaller than the inertial forces. This gives $U = \frac{\Delta p t}{\rho H}$, with t the time at which the velocity is computed. For $t = 10^{-2}$ this gives $U = 10^{-2}$, corresponding to a Reynolds number of 100, which makes the assumption that the pressure drop and the instationary inertial term balance valid. A timestep of $\Delta t = 2.5 \cdot 10^{-4}$ is used and 40 timesteps are taken. For the same MBFM mesh as in the previous analysis and for two XFEM-ALE meshes $N_x = 101, 201$ the solution is given in Figure 4.13. The x -velocity, pressure and shear-stress for the XFEM-ALE simulation is very similar to the solution from the MBFM simulation. Even for the coarsest mesh XFEM-ALE gives approximately the same result. This confirms that XFEM-ALE gives correct results in the primary variables velocity and pressure as well as in the derivatives of the velocity.

4.6 Conclusions

In this chapter the numerical aspects in solving the fluid-structure interaction problem as encountered in cilia driven flow were treated. First the deficiencies of the fictitious domain/Lagrange multiplier method were shown, namely that it cannot capture discontinuities in the solution and that imposing kinematic interface conditions with Lagrange multipliers can lead to difficulties. The first problem was solved by using XFEM, which allows discontinuous shapefunctions in the finite element method, and the second was solved by using a newly

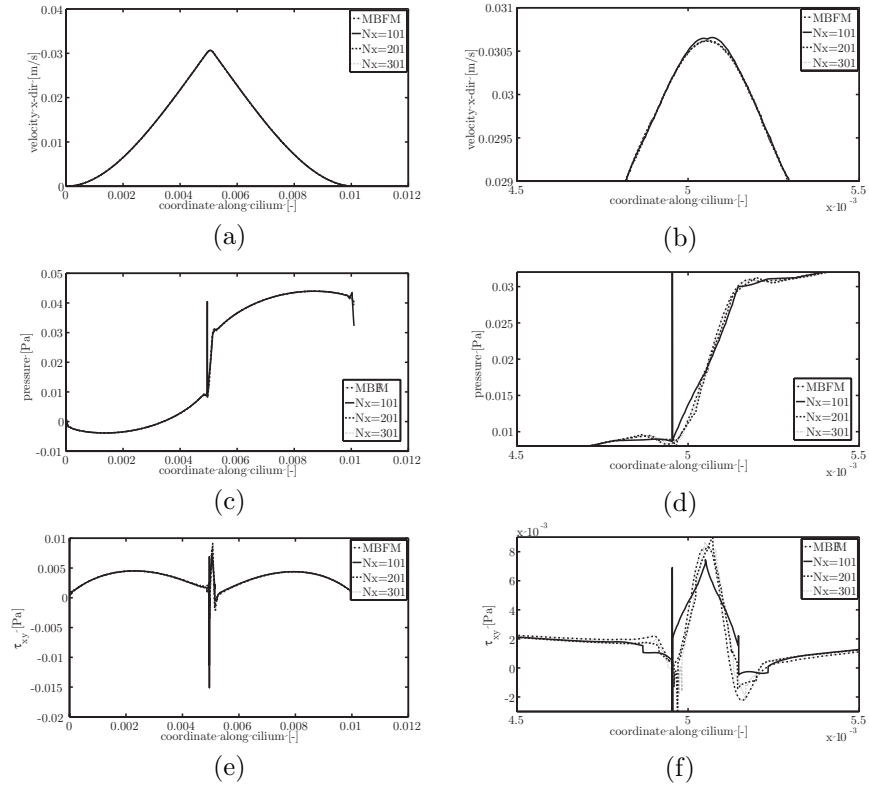


Figure 4.12: The results from an ALE (MBFM) and XFEM-weak interface simulation of beam in a channel over which a pressure drop is applied. All values are plotted along Γ_{fs} starting at the right lower corner going counter clockwise. Figure (a) shows the velocity in x -direction, (b) is a zoom of (a) near the cilium tip. (c) Shows the pressure over the entire cilium length, and (d) is a zoom in of (c) near the tip. The shear-stress τ_{xy} is shown in (e) and a zoom in (f).

developed method for imposing Dirichlet boundary conditions in a weak sense. The latter method was extended in order to use it for more general constitutive relations, such as generalized Newtonian and viscoelastic fluid models. In the same spirit the incorporation of the dynamic interface condition, which forces traction continuity, was treated and a weak form for the fluid-structure interaction problem was presented. This method does not require additional degrees of freedom, thus does not enlarge the final system to be solved. Finally the accuracy of the weak interface conditions was assessed, both for Dirichlet boundary conditions and for fluid-structure interface conditions. In both cases

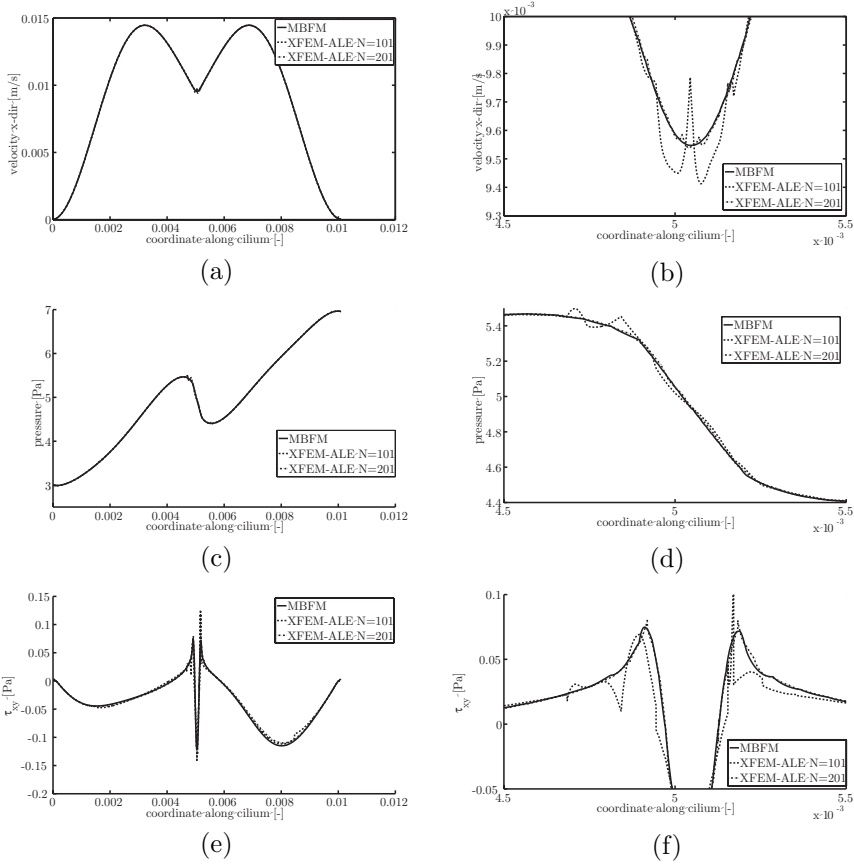


Figure 4.13: The results from an ALE (MBFM) and XFEM-weak interface simulation of beam in a channel over which a pressure drop is applied. Startup flow from rest. All values are plotted along Γ_{fs} starting at the right lower corner going counter clockwise. Figure (a) shows the velocity in x -direction, (b) is a zoom of (a) near the cilium tip. (c) Shows the pressure over the entire cilium length, and (d) is a zoom in of (c) near the tip. The shear-stress τ_{xy} is shown in (e) and a zoom in (f).

the method was stable and accurate. For the Dirichlet boundary conditions optimal convergence rates for the velocity and pressure were found. For two fluid-structure interaction problems where a pressure drop was applied over a beam in a channel, the velocity, pressure and shear-stress were compared at the boundary of the beam. For both simulations without inertia it was shown that XFEM with weakly imposed interface conditions gives the same results as the Moving Body Fitted Mesh (MBFM) solution, which was the reference. For

flows with inertia, XFEM with temporary ALE steps also gave the same results as the MBFM scheme. Although the deformation of the beam was small, both XFEM and XFEM-ALE will also give accurate results for larger deformations since the fluid mesh is fixed. In the case of inertial flow, the ALE steps will only have small deformations, thus have small errors. We can thus conclude that the modified Gerstenberger-Wall scheme for fluid-structure interaction is spatially optimally convergent and gives the same results as a moving mesh approach, with the advantage that a fixed mesh can be used for the fluid domain at all timesteps.

Chapter 5

Simulation of transport and mixing by artificial cilia: Newtonian fluid

In the previous chapters a model of artificial cilia was developed and accurate numerical techniques for solving the model equations were introduced. This opens up the road for studying the flow generated by artificial cilia. In Section 5.1 a single cilium is actuated with a constant body force, in order to find the scaling relations for this problem, mimicking a magnetically actuated cilium. In several studies a rotating magnetic field is used to actuate the cilia [2, 4, 36]. Here this rotating magnetic field is modeled as a rotating body force. Since fluid-structure interaction problems have an intrinsic time-scale, as shown in Chapter 2, even in absence of fluid and solid inertia, the dynamics of the system change with changing actuation frequency. Thus the influence of the actuation frequency on the motion and the generated flow is studied in Subsection 5.1.2. Khataavkar *et al.* [9] showed that two cilia which were actuated by the same rotating body force, but with a difference in phase angle of 90 degrees generated efficient mixing. Since the actuation of each cilium individually is cumbersome in practice, we would like to use the same actuation means for all cilia, yet still let them move at a phase angle. Since the motion of the cilium depends both on the time-scale t_3 and the actuation frequency, two cilia with different time-scales, but the same actuation frequency will show different motion. By scanning the available parameter space, we analyze the mixing performance of systems with two cilia, which have different properties. Results of this analysis are shown in Section 5.2. As the goal of mixing is to create chaotic motion of fluid particles in a non-chaotic flow, the possibility of having chaotic motion of the cilium is investigated in Section 5.3.

5.1 Transport

Artificial cilia are mainly developed as microfluidic actuators, which cause either fluid transport or fluid mixing [1, 2, 36]. As was shown in Chapter 2, the main difference between transport and mixing are the boundary conditions for the fluid domain. For transport a periodic domain is considered, for mixing a closed domain. Although the boundary condition has profound effects on the flow, the modeling and actuation of the cilia remains unchanged.

In Section 2.4 it was shown that a fluid-structure interaction problem involving a non-rigid solid, has an intrinsic time-scale t_3 . This time-scale is present in the system due to the interface conditions at the fluid-structure interface, and not due to inertial terms in the momentum equations of the fluid or solid. In this section the influence of problem parameters on this time-scale are simulated. The domain under consideration is a periodic domain containing a single cilium at the center of the domain, as depicted in Figure 5.1. The

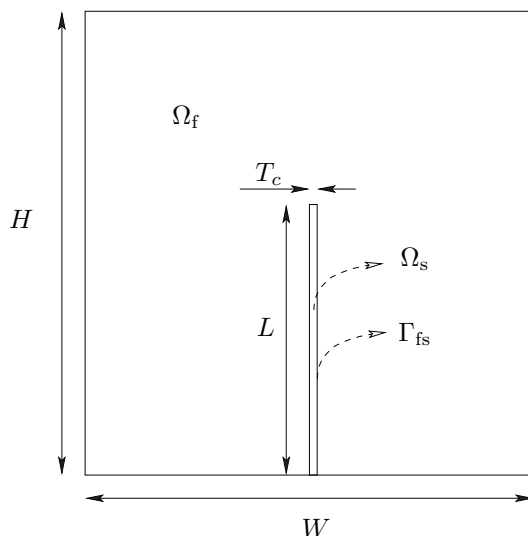


Figure 5.1: The periodic channel with height H , width $W = H$, cilium length L_c and cilium thickness T_c .

fluid and solid are assumed to be inertialess, so all time dependent and convective terms are considered to be absent in both the momentum equation of the fluid and solid. This is valid for slowly varying actuation forces, resulting in low velocities and small effects of inertia.

5.1.1 Results: scaling

A cilium actuated with a body force which follows the following step-function is modeled:

$$\mathbf{f} = \begin{cases} \mathbf{0} & \forall t \leq 0, \\ f_0 \mathbf{e}_x & \forall t > 0, \end{cases} \quad (5.1)$$

where f_0 is the magnitude of the actuation force. The position of the top-right corner of the cilium as well as the velocity in this point are recorded. The stiffness of the cilium is varied, either by changing the modulus or the thickness. In addition the influence of viscosity and aspect ratio are investigated. For $\eta = 1$, $L = 0.5H$, $T_c = 0.02H$, $f_0 = 4 \cdot 10^3$ and $G_s = 10^n$ where $n = 3-8$, the tip velocities in x -direction are shown in Figure 5.2. The velocity is scaled by $\frac{f_0 L^2}{\eta}$

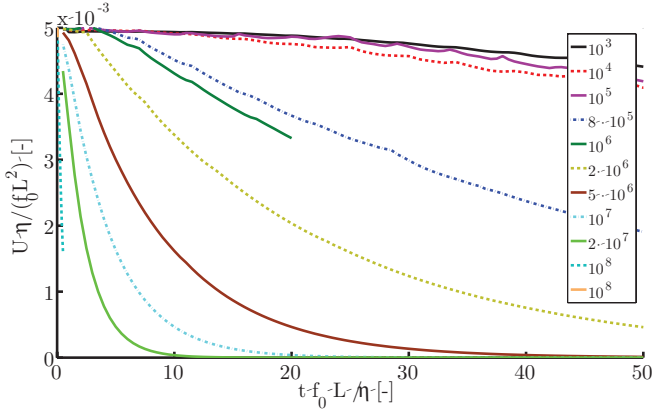


Figure 5.2: The tip velocity versus time in x -direction for different moduli of the cilium.

and time with $\frac{\eta}{f_0 L}$. Since only the modulus is varied, the scaling parameters of time and velocity are independent of this variation thus showing different behavior. The velocity drops off more slowly if the modulus is decreased. This suggests that the time can be scaled with $t_3 = \frac{\eta}{G}$, which is shown in Figure 5.3. The decay of the x -velocity overlaps for all moduli larger than 10^6 . So for stiff cilia the appropriate time-scale is indeed t_3 . The time-scale of the more compliant cilia scales differently, and the reason for this effect must be sought in the fact that for very compliant cilia the deformation is different than for stiff cilia. Stiff cilia deform only due to the applied force, compliant cilia due to the applied force and the viscous drag. The initial velocity is independent of the stiffness of the cilium, which is explained by the fact that the solid is stress-free initially. Therefore the initial displacement of the solid requires

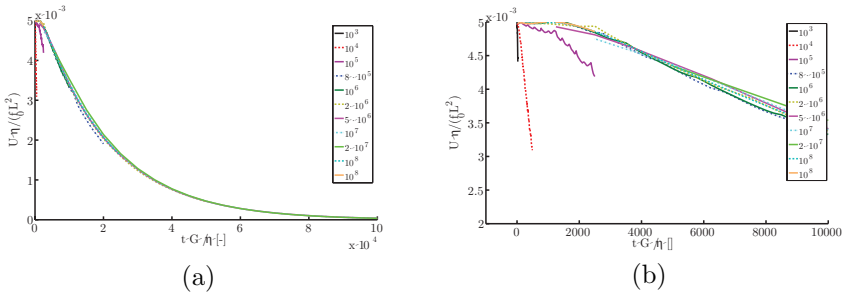


Figure 5.3: The tip velocity of a cilium in a periodic channel with varying modulus versus time. (a): velocity x -direction (b): zoomed-in plot of the x -velocity.

almost no force, thus most of the force is used for overcoming the viscous drag of the cilium. By scaling the tip velocity with $\frac{f_0 L^2}{\eta}$, the initial velocities for different viscosities, applied forces and cilium lengths fall onto a single curve. This scaling also has a consequence for the initial timestep used in simulations; It only depends on the time-scale $\frac{\eta}{f_0 L}$, so for every cilium stiffness it is the same.

5.1.2 Rotating force field

In the previous subsection a constant actuation force was used, which is the most simple forcing available and thus enables us to determine the characteristic time-scale of the system. Although the main characteristics of the fluid-structure interaction problem can be studied systematically with this forcing, it is difficult to realize this in practice. Hence a periodic actuation force [1, 9] or field [2, 36] was proposed by a number of authors. Here we use the following periodic actuation body force:

$$\mathbf{f} = f_0 (\cos(2\pi\omega t)\mathbf{e}_x - \sin(2\pi\omega t)\mathbf{e}_y), \quad (5.2)$$

where f_0 is the amplitude of the actuation force which is constant in time. Since the fluid-structure interaction has a time-scale $t_3 = \frac{\eta}{G_s}$, as we have seen in the previous section, and an external actuation time-scale $\frac{1}{\omega}$ is introduced, the following dimensionless group can be formed $R_4 = \omega t_3$. This dimensionless number gives the ratio between the actuation time-scale and the intrinsic time-scale of the system. If $R_4 \ll 1$ the cilium will follow the force quasi-statically. If $R_4 \gg 1$ the cilium is not able to follow the force and will not move. In between those limits the cilium will lag behind the force. This behavior is studied by varying R_4 through variation of ω and keeping all other parameters

the same. The following parameter set was used in the simulations: $H = 1$, $L = H$, $L_c = 0.5H$, $T_c = 0.02H$, $\eta = 1$, $G_s = 1 \cdot 10^4$, $f_0 = 8 \cdot 10^3$. Hence the characteristic time-scale $t_3 = 1 \cdot 10^{-4}$. Again the top-right position of the cilium, the velocity in that point and the flow rate over the channel will be monitored in time. The path followed by the tip is shown in Figure 5.4. For small $R_4 \leq 1.15 \cdot 10^{-3}$ values, the actuation shows similar motion with increasing frequency. This motion also becomes periodic after one actuation period. For intermediate values $1.15 \cdot 10^{-3} < R_4 < 7.5 \cdot 10^{-3}$, the motion of the cilium changes a lot, and the motion becomes periodic after several cycles. The amount of cycles required increases with increasing actuation frequency. For the highest actuation frequencies $R_4 \geq 7.5 \cdot 10^{-3}$, the motion of the cilium is reduced even more, and the motion has not become periodic, at least not within the time the simulation was performed. Figure 5.4(i) shows the highest actuation frequency simulated, where the tip of the cilium follows a more or less circular path each cycle. The cilium is moving only slightly. For even larger actuation frequencies, it is expected that the motion will become even less, until the cilium is stagnant at very high frequencies. This can be seen as the cilium being unable to follow the quickly rotating force field. From this analysis we learn that the actuation frequency for a different cilium/fluid combination should be changed too, in order to give the same cilium motion. So naively using the same actuation scheme for a given cilium/fluid combination will not always work.

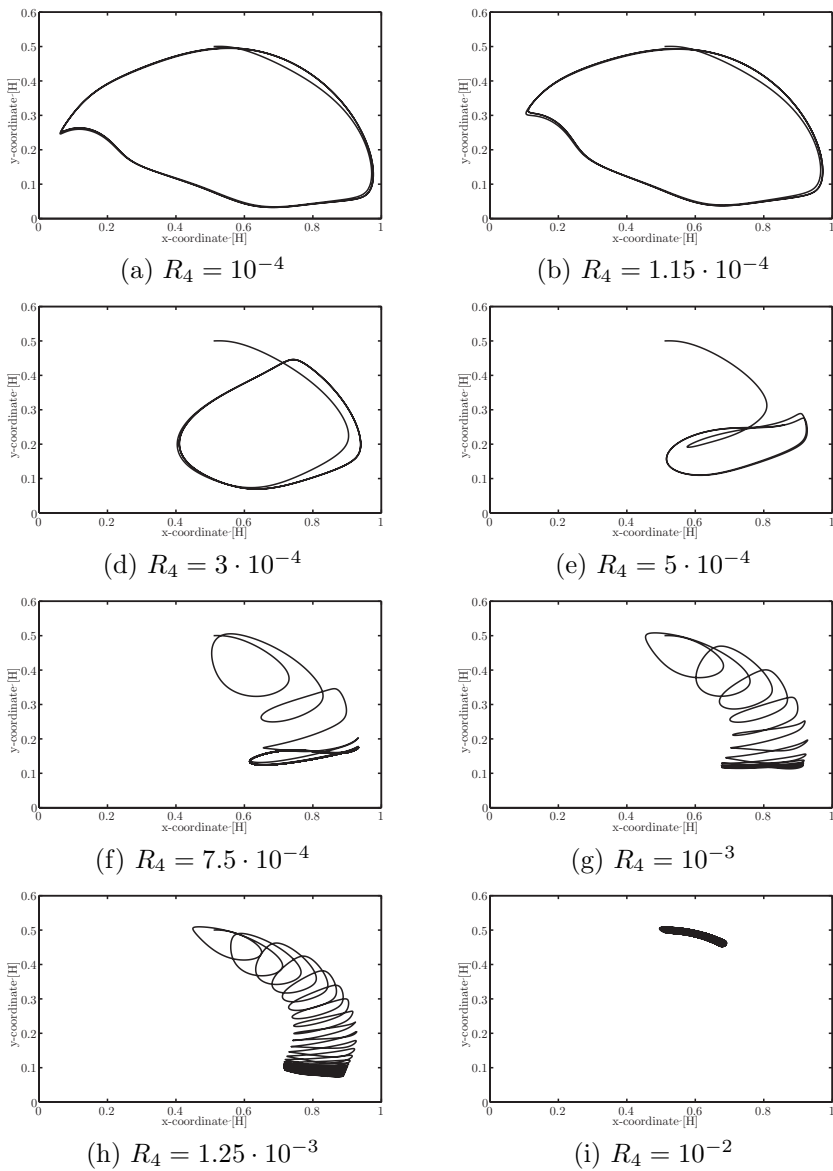


Figure 5.4: The path followed by the top-right corner of the cilium for various actuation frequencies.

For $R_4 = 3 \cdot 10^{-4}$, the motion of the cilium during a periodic cycle and for $R_4 = 10^{-3}$ the motion of the last simulated cycle, which is not periodic, is shown in Figure 5.5. In red the part of the cycle is given where the horizontal

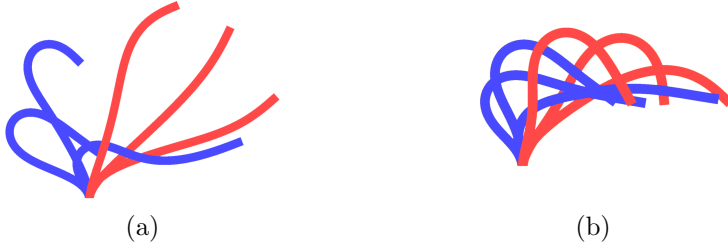


Figure 5.5: The motion of the cilium for $R_4 = 3 \cdot 10^{-4}$ (a) and $R_4 = 10^{-3}$ (b). The red snapshots indicated when the horizontal component of the rotating actuation force is pointing to the right, and the blue snapshots when it is pointing to the left.

part of the rotating body force is pointing to the right, in blue where it is pointing to the left. The cilium actuated at low frequency, clearly sweeps a larger area than the high frequency actuated cilium. In both cases the cilium buckles when the body force is oriented towards the anchoring point, which folds the cilium during the motion to the left. When the force is applied away from the anchoring point, the cilium is stretched out and displaces much more fluid. For the higher actuation frequency, the tip of the cilium does not move that much, while the middle section of the cilium does move, which results in an peculiar cilium cycle. The total amount of fluid which is transported during one cycle is computed by first computing the flowrate $Q = \int_0^H \mathbf{n} \cdot \mathbf{u} ds$ on the right boundary of the computational domain and then integrating $q = \int Q dt$ over $1/\omega$ when a steady state has been reached. The resulting flowrate Q is given in Figure 5.6 for $\omega t_3 = 1 \cdot 10^{-4}$ and $\omega t_3 = 1 \cdot 10^{-3}$.

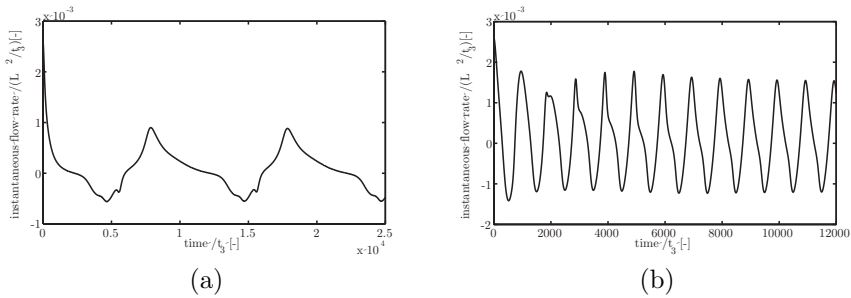


Figure 5.6: The flowrate versus time for two actuation frequencies: (a) $\omega t_3 = 1 \cdot 10^{-4}$ (b) $\omega t_3 = 1 \cdot 10^{-3}$.

From this time dependent flow the total flow per cycle q is computed by integrating Q over one cycle when the flow has become periodic. For the higher actuation frequencies $R_4 > 10^{-3}$ the flow becomes periodic while the motion of the cilium is not periodic. A possible reason could be that the cilium motion is similar at longer times, yet not periodic. This would lead to almost the same flow field. For a range of actuation frequencies, the flow per cycle is given in Figure 5.7. The flow per cycle decreases steadily for increasing actuation frequency, which can be related to the decrease of the swept area with R_4 in Figure 5.4. By multiplying the flow per cycle with the frequency of actuation, the flow-rate is obtained. For cilia in a transport geometry, the flow-rate is the objective function which should be maximized. In Figure 5.8, the flow rate is given as a function of the actuation frequency and it has three regions. At low frequencies the flow-rate increases linearly, since the motion of the cilium is independent of the frequency for low frequencies. So the flow per cycle is about constant and the flow-rate scales linearly with frequency. At very high frequencies, the cilium is almost stagnant and hardly any fluid is displaced per cycle. Even if this low flow per cycle is multiplied with the high frequency the flow-rate is still very low. For an increasing actuation frequency, the flow-rate decreases in this region. Since the flow-rate increases at low frequencies and decreases at high frequencies an optimum is present in order to have a smooth transition. In this case the optimum is found at $R_4 = \omega t_3 = 3 \cdot 10^{-4}$. So the cilia pump most effectively when they do not displace the largest amount of fluid per cycle, which means that using the largest amount of displaced fluid per cycle is not the best optimization parameter. For real systems where we would like to achieve good transport performance, and the viscosity is 1 mPa s (water) and the modulus of the cilium is 1 MPa, the actuation frequency should be $3 \cdot 10^5$ Hz, which is rather high. For a more viscous fluid with a more compliant cilium this could become $\mathcal{O}(10^2)$ Hz, which is more realistic. A possible explanation for the high frequencies is the fact that only material stiffness is used for scaling t_3 and not the geometrical stiffness of the beam. This also explains why the transition of the motion of the cilium starts at about

$R_4 = 1 \cdot 10^{-4}$, while one would expect a transition at $R_4 = 1$. The factor 10^4 is a non-dimensional pre-factor, incorporating the geometrical stiffness of a beam. So changing the geometry, or better the length/thickness ratio $\frac{L}{T_c}$ of the beam, means also changing this pre-factor.

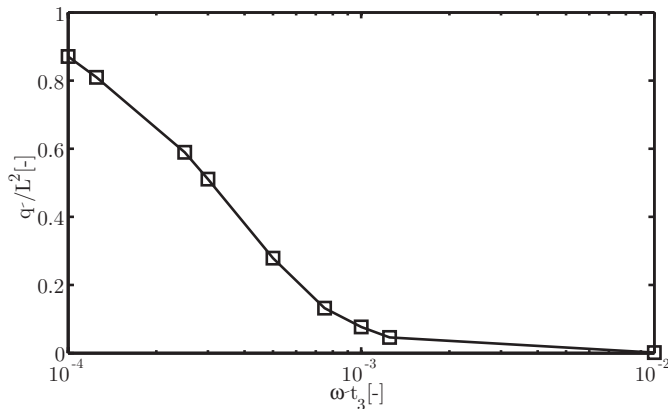


Figure 5.7: The total net flow generated by the actuated cilia during one cycle when the motion of the cilium has come periodic, given for different actuation frequencies.

5.2 Mixing

Artificial cilia can be used as an active micro-fluidic mixer, since the flow is convection dominated, rather than diffusion dominated, even in micro-fluidic channels (See Section 2.5). This means that efficient mixing occurs through chaotic advection only. Khatavkar *et al.* [9] showed that the phase lag between two individual cilia affects the mixing performance significantly. If both move synchronously, the phase lag is zero and it is 180 degrees if they both move exactly opposite, as shown in Figure 5.2.

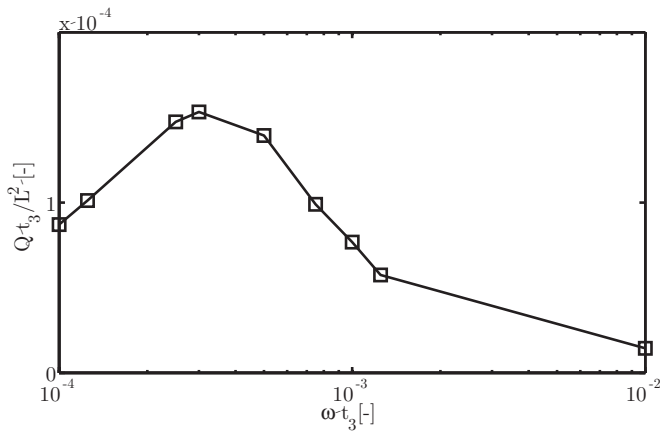


Figure 5.8: The flow total net flowrate for different actuation frequencies

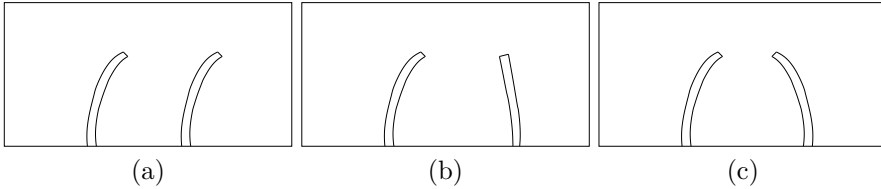


Figure 5.9: The phase lag expressed in angles: (a) 0 degrees, which means synchronous motion of two cilia. (b) 90 degrees, which means that one cilium is lagging behind with quarter of a period compared to the other and (c) 180 degrees, which means opposite motion of two cilia.

In [9], the mixing performance was measured by monitoring the length increase of a drop which was initially placed in between the two cilia. It was shown that a phase angle of 90 degrees achieved the best mixing. In the work of Khataavkar [9], the phase lag between the two cilia was induced externally by applying phase angle between the rotating force of each individual cilium. Although this method can easily be used in simulations, the individual actuation of a single cilium is not that easily achieved in practice. The main problem is that individual field generators, either electric or magnetic, have to be miniaturized and incorporated into the micro-fluidic device. This makes the device more complicated and thus both the failure rate and costs are higher. Therefore other means of generating a phase lag between cilia, without requiring individual actuation have to be found. The starting point of developing such a system is the observation that the motion of the cilia is frequency dependent, as was observed in the previous section. There the motion of the cilium was recorded for different actuation frequencies, and a decrease in motion was observed for an increase in frequency. Therefore, by actuating two cilia with different characteristic frequencies we would observe different motion of both cilia. Instead of changing the actuation frequency, we propose to change the typical time-scale of each individual cilium by changing the stiffness of the cilium, and keeping the actuation field constant for all cilia. This can be incorporated into the device by changing the cilium thickness.

5.2.1 Problem description

A rectangular domain is modelled containing two cilia, see Figure 5.10. Either the modulus of the individual cilia or its thickness is changed. Since the motion of a cilium depends on the actuation frequency, two different actuation frequencies will be used leading to $R_4 = 3 \cdot 10^{-4}$, the optimal for transport and $R_4 = 1 \cdot 10^{-3}$, which resulted in less fluid transport. All values of R_4 were computed with the properties of the left cilium. We would like to know under which conditions this system leads to mixing of the fluid.

Three different sets of simulations have been performed, one in which the

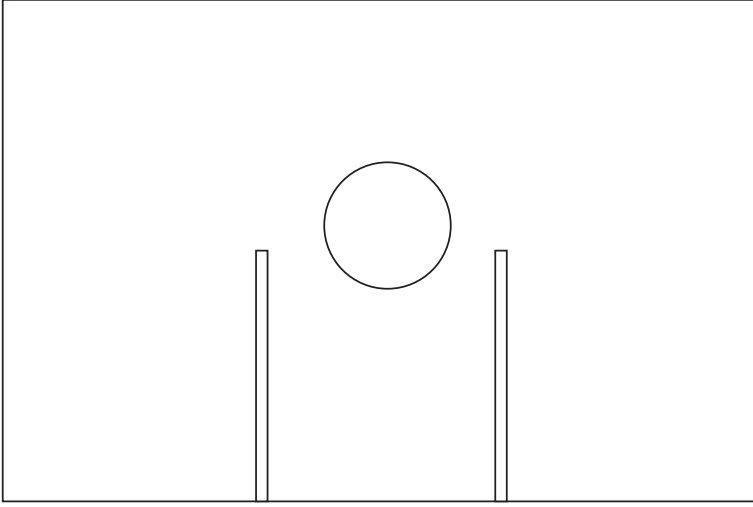


Figure 5.10: The mixing domain of height H and width $= 1.5H$ containing two cilia with length $L = 0.5H$, spaced $0.5H$ apart. The thickness of the left cilium is T_{c1} , of the right cilium T_{c2} . A blob is placed in between the cilia for measuring mixing performance.

modulus of the right cilium is increased from $2.5[f_0L]$ to $2.5 \cdot 10^3[f_0L]$ for $R_4 = 3 \cdot 10^{-4}$. In the second set the stiffness of the right cilium is increased by increasing the thickness from $T_{c2} = T_{c1}$ to $T_{c2} = 2T_{c1}$ with $R_4 = 3 \cdot 10^{-4}$ and the last set contains the same thickness variation with $R_4 = 1 \cdot 10^{-3}$. The conditions for the simulations with the cilia moduli, thicknesses and actuation frequencies are given in Tables 5.1 -5.3. The mixing performance

Table 5.1: Variation of cilium modulus.

Name	Modulus left cilium $[f_0L]$	Modulus right cilium $[f_0L]$	$T_{c1}[L]$	$T_{c2}[L]$	$R_4[-]$
A_1	2.5	2.5	0.04	0.04	3
A_2	2.5	$2.5 \cdot 10^1$	0.04	0.04	$3 \cdot 10^{-4}$
A_3	2.5	$2.5 \cdot 10^2$	0.04	0.04	$3 \cdot 10^{-4}$
A_4	2.5	$2.5 \cdot 10^3$	0.04	0.04	$3 \cdot 10^{-4}$

can be measured in several ways, see Section 2.5. Since it is not clear whether the movement of the cilium becomes periodic, measures which depend on the periodicity of the velocity field cannot be used. Hence we use the simplest mixing measure, which is the stretch of a blob of material. The blob with

Table 5.2: Variation of cilium thickness, $\omega t_3 = 3 \cdot 10^{-4}$.

Name	Modulus left cilium [f_0L]	Modulus right cilium [f_0L]	$T_{c1}[L]$	$T_{c2}[L]$	$R_4[-]$
B_1	2.5	2.5	0.04	0.04	$3 \cdot 10^{-4}$
B_2	2.5	2.5	0.04	0.06	$3 \cdot 10^{-4}$
B_3	2.5	2.5	0.04	0.08	$3 \cdot 10^{-4}$

Table 5.3: Variation of cilium thickness, $\omega t_3 = 10^{-3}$.

Name	Modulus left cilium [f_0L]	Modulus right cilium [f_0L]	$T_{c1}[L]$	$T_{c2}[L]$	$R_4[-]$
C_1	2.5	2.5	0.04	0.04	10^{-3}
C_2	2.5	2.5	0.04	0.06	10^{-3}
C_3	2.5	2.5	0.04	0.08	10^{-3}

radius $0.2L$ is placed in between the two cilia with the center at $(x, y) = (0.75H, 0.6H)$, as shown in Figure 5.10. The blob is placed in between the cilia, since the most stretching due to elongation flow is expected in this region. The change of interfacial length of the blob will be computed over time.

5.2.2 Results

The interfacial length stretch ($l/l_0 = l/(0.8\pi L)$) of the blob is given versus time in Figure 5.11 for the simulations given in Table 5.1. All simulations are performed for at least two actuation cycles (each cycle has a period of $1/(t_3\omega) = 1/(3 \cdot 10^{-4})$). Although the length of the blob increases for all moduli, there is not a clear trend. The blob is stretched the most for the intermediate modulus $25 [f_0L]$. Good mixing is indicated by an exponential increase in length (indicating an exponential decrease in distance opposite to the stretching direction). For the blob which is stretched the most this seems to be the case, although longer simulations should be performed in order to confirm this. If the cilium thickness of the right cilium is increased, a stronger effect is found, see Fig 5.12.

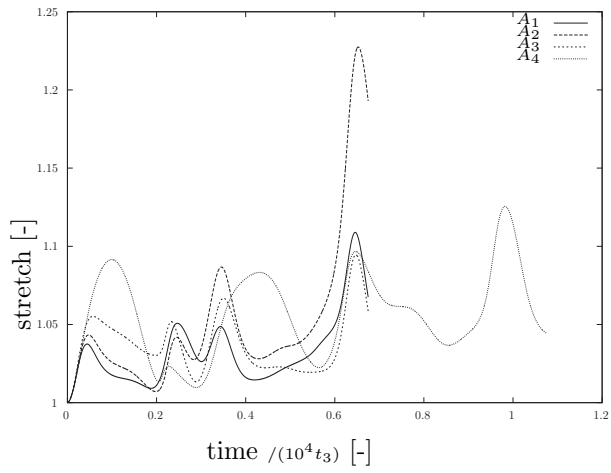


Figure 5.11: The stretch of the blob versus time for different moduli of the right cilium for the parameters in Table 5.1.

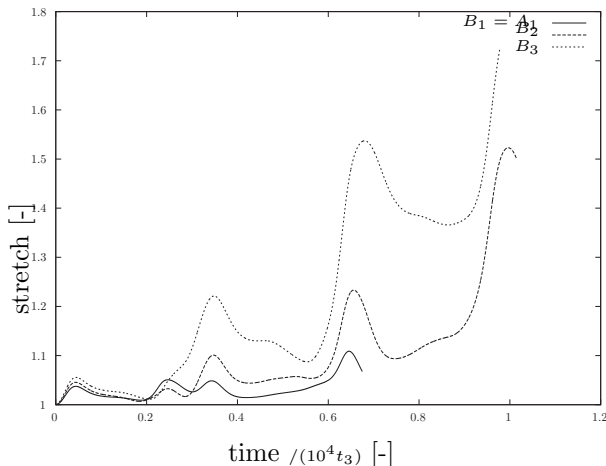


Figure 5.12: The stretch of the blob versus time for different thicknesses of the right cilium for the parameters in Table 5.2.

A clear trend can be seen: larger differences in cilium thickness lead to better mixing. And again the stretch seems to be exponential, but longer simulations have to confirm this. For the simulations at the higher frequencies, the trend is the same, see Figure 5.13, yet the overall stretch is lower. Hence larger fluid displacements seem to be important in order to obtain efficient mixing. In all cases the results do not give any information on the mixing performance in the remainder of the domain.

5.3 Chaotic cilium motion

The motion of an artificial cilium in an inertialess fluid is described by Eqs. (2.2–2.3, 2.11–2.12). This set of equations is time dependent and also non-linear. The nonlinearity of the problem is due to the movement of Γ_{fs} , due to quadratic terms in the constitutive relation of the solid and due to the slenderness of the cilium which causes different behavior in tension and compression (buckling). Dynamical systems can show remarkable movement if they are highly non-linear. Bifurcations, which means that two or more solutions are possible or even chaos, where an infinite, but bounded, amount of solutions is possible are observed if the system is highly non-linear. The main question is whether bifurcations and chaos can also be expected for the artificial cilia. Let's consider the following simplified model of a cilium, consisting of a dashpot representing the fluid drag with damping coefficient d , a spring representing the cilium with stiffness k and a driving force f . The displacement x is the only free variable in the system. The stiffness of the spring is chosen to be $k = k_0(x - 1)$, representing a higher stiffness in tension than in compression. The driving

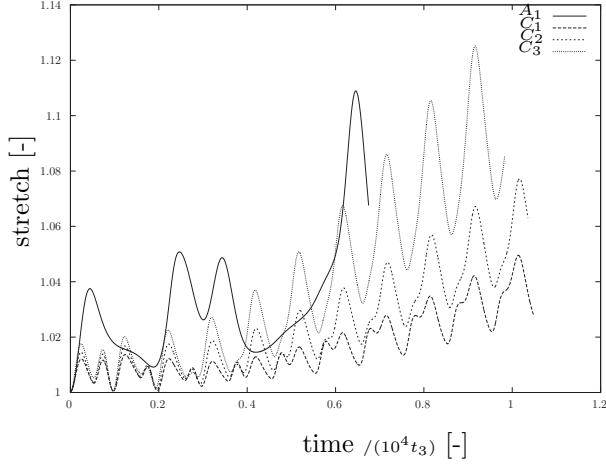


Figure 5.13: The stretch of the blob versus time for different thicknesses of the right cilium for the parameters in Table 5.3. For comparison the stretch for configuration A_1 is also shown.

force $f = f_0 \sin(2\pi\omega t)$, where f_0 is the force amplitude and ω the frequency of oscillation. The equation of motion then becomes:

$$\begin{aligned} d\dot{x} + kx &= f, \\ d\dot{x} + k_0(x - 1)x &= f_0 \sin 2\pi\omega t. \end{aligned} \quad (5.3)$$

After using an explicit Euler time integration scheme the discretized equation becomes:

$$d \frac{x^{i+1} - x^i}{\Delta t} + k_0(x^i - 1)x^i = f_0 \sin 2\pi\omega t^i, \quad (5.4)$$

where the superscripts $i + 1$ and i denote the variable at the current and previous timestep respectively and Δt is the timestep. Re-arranging yields:

$$x^{i+1} = x^i - \frac{k_0}{d\Delta t}(x^i - 1)x^i + \frac{f_0}{d\Delta t} \sin 2\pi\omega t^i, \quad (5.5)$$

which is the ‘‘Logistic Map’’ with an extra forcing term. The logistic map [70] is known to show a bifurcation at $R = \frac{k_0}{d\Delta t} > 2$, which for a given k_0 and d means $\Delta t < \frac{d}{2k_0}$. For $2 < R < 4$ it shows more bifurcations, and for $R > 4$ the motion is chaotic, thus having no periodicity. So even for this very simple non-linear model of a cilium, bifurcations and chaos can be observed if R is high enough. Low R values are related to a low stiffness of the cilium and much damping large. So for cilia with a large aspect ratio moving through a viscous fluid bifurcations and chaos can be expected for this simple model.

The predictions of this simple model have not been verified with simulations of the full fluid-structure interaction model.

5.4 Conclusions

In this chapter the model developed in Chapter 4 was used for the simulation of cilia in a Newtonian fluid. Both transport and mixing are investigated. For the transport geometry it was found that the time-scale of motion for stiff cilia ($G > 10^6$) indeed is $t_3 = \frac{\eta}{G}$ as was predicted from the scaling analysis in Section 2.4, while for the more compliant cilia the time-scale is $\frac{\eta}{f_0 L}$. This difference was explained by the fact that viscous forces play an important role in both the deformation and time-scale of deformation for the compliant cilia, while it only affects the time-scale for the stiffer cilia. In all cases the tip velocity of the cilium scales with $\frac{f_0 L^2}{\eta}$, which is independent of the stiffness of the cilium. This was explained by the absence of elastic forces at the very beginning of actuation, hence the actuation force is balanced only by the viscous drag forces on the cilium. This has an important consequence for the simulations, namely that the timestep is independent of the cilium stiffness, and moreover independent of t_3 . This means that very small timesteps have to be used although the system moves on a much larger time-scale. The cilia are also actuated with a rotating body force with varying frequency. It was shown that the motion of the cilium tip become periodic for the lower frequencies $R_4 = 1 - 7.5 \cdot 10^{-4}$, while for the higher frequencies the motion did not become periodic within the time-scale of simulation. The computed flow per cycle steadily decreased for increasing frequency and the total flow rate showed an optimum at $R_4 = 3 \cdot 10^{-4}$. For low frequencies the flow rate increased linearly with frequency, and for higher frequencies the flow rate dropped. On the basis of the notion that cilium motion depends on the actuation frequency, a two cilia micromixer was designed, where the intrinsic time-scale of the individual cilia were changed, instead of the actuation frequency. The time-scale was either changed by changing the modulus of the individual cilia or by changing cilium thickness. The mixing performance was assessed by analyzing the length-stretch of a blob placed in between the two cilia. The system with two cilia with different modulus showed an increase in stretch, yet a clear trend was not observed. The stretch increase seemed to be exponential, although this has to be confirmed by longer simulations. For the system with different cilium thicknesses, the length stretch increased with the ratio of cilium thicknesses, and again the stretch seemed to increase exponentially. For a system with different thicknesses, but actuated at a higher frequency, the stretch is much lower than at low frequency, but the trend between thickness ratio and stretch is still observed. It was shown that for a non-linear stiffness of the cilium, the

cilium motion could become chaotic for a one dimensional model system. This has not been confirmed with simulations.

Chapter 6

Numerical tools for modeling of cilia driven flow of non-Newtonian fluids

In Chapter 4 a model was developed for cilia driven flow of a Newtonian fluid. Although many fluids are Newtonian, *i.e.* show a linear relation between the fluid stress and the rate of deformation, an even larger group of fluids behaves non-Newtonian. The branch of science which studies the relation between fluid stress and deformation is rheology. An important class of non-Newtonian fluids are macromolecular solutions. In these solutions even a small weight fraction of macromolecules changes the rheology significantly even if the solvent is a Newtonian fluid.

Artificial cilia are fluid manipulators for Lab-on-a-Chip devices. In these devices, biological fluids such as blood, urine and saliva are analyzed, all of which are solutions of cells or proteins in water. A solution of large molecules, such as proteins shows distinct flow effects due to the interaction of the elastic proteins with the viscous drag of the water surrounding them. These effects, among them shear-thinning, strain-hardening and normal stresses in shear flow, are known as viscoelastic effects.

A lot of research has been done to understand and control the flow in microfluidic devices, but almost all work, both experimental and numerical, was performed with water as the model fluid. Since water and biological fluids have different flow properties, it is important to ascertain whether the flow phenomena and control strategies found for Newtonian fluids also work for non-Newtonian fluids.

The most profound differences are expected for force driven flows. In force driven flows, the kinematics are not determined fully by the essential boundary conditions, but also by natural boundary conditions. Since the stress in a non-Newtonian fluid depends nonlinearly on the velocity gradient, a small change in such a natural boundary condition leads to a large change in the velocity gradient. In systems with actuators this effect is also expected, since the motion of the actuators is almost always force driven. This means that the rheology of the fluid has a profound effect on the flow, and more importantly on the efficiency of the actuators.

In this thesis we will focus on saliva, since it is a homogeneous fluid, even at the scale of microfluidic channels. Although the rheological properties of saliva have been studied in the past [71], not much data is available in literature. Hence we have measured the shear rheology of human, unfiltered, saliva. The measurement data serves as an input to the fluid-structure interaction model developed in the previous chapter. In order to model non-Newtonian fluid flow, the model has to be adapted to allow different constitutive behavior, and to stabilize the numerical model in the case of viscoelastic computations. This model is given in Section 6.2.

6.1 Saliva rheology

One of the fluids which is analyzed in Lab-on-a-Chip devices is saliva. Saliva is a solution of large molecules, macromolecules, in water. It plays an important role in the digestive system, by lubrication and adding enzymes, and in oral hygiene, by cleaning the mouth [72]. It therefore contains information on the person's health, and since it is easily sampled, it is often used for analysis. If looked at from a rheological standpoint, instead of a biological one, saliva contains large molecules which give it different flow behavior than the solvent, which is water, alone. Under steady shear it shows a decrease in shear viscosity, known as shear-thinning [73]. By filtering out the longer molecules, this behavior is suppressed. Since not much rheological data on saliva is found in literature [73], or the measured ranges are quite small, we performed steady state shear measurements on human whole saliva (HWS), which was not filtered.

6.1.1 Materials and methods

The rheology of human whole saliva is tested using an ARES 902-30004 rheometer of Rheometric Scientific. A plate-plate setup (50 mm diameter plates) was used. Saliva samples were collected from five test subjects, by letting them drool into a plastic cup. The drooling prevented much of the air bubbles, which are usually present in saliva and hence homogeneous samples were obtained. The donors were instructed not to eat or drink anything other than

water for one and a half hours before the test. Directly after donation, 2-3 ml of saliva was pipetted in between the plates of the rheometer. Then a series of steady-state shear tests were performed where the steady-state viscosity was measured after 50 s of shearing at shear-rates of 1 up to 500 s^{-1} . The series were performed four times, where the results from the first set were disregarded, since they always showed lower and non-reproducible viscosities. The most likely reason for this behavior are air bubbles, which are broken up at the high shear-rates of the first series. The results of the remaining three series were reproducible. Initial tests in which the viscosity was recorded from the commence of shearing showed that it took 50 s to reach steady state, hence the steady state viscosity was recorded only after 50 s. The reason for this could be the reversible (elastic) effects or irreversible effects (break up of a network). The latter can be ruled out, since the sample showed the same transient behavior when the experiment was repeated. Hence the time-dependency is attributed to elastic effects.

6.1.2 Results

The measured saliva rheology data is shown in the top of Figure 6.1. The error bars indicate the standard deviation of all measurements and test subjects and is due to differences between the subjects, not between different measurements of the same sample. This shows that the test method used is reproducible. It is also clear that saliva is extremely shear thinning, since the viscosity declines rapidly over this range of shear rates, whilst no zero-shear rate plateau and infinite shear rate plateau is found. A wider range of shear rates has been used for only one test person and is shown in the lower part of Figure 6.1. It shows the remarkably high zero shear rate plateau of 70 Pa s. It is expected that the viscosity remains constant at 1 mPa s at higher shear rates, which is the viscosity of water. A fit of the Carreau rheological model, Equation (2.6), to this measurement yields $n = 0.2$, $\eta_0 = 70 \text{ Pa s}$, $\eta_\infty = 1 \text{ mPa s}$, $\lambda = 100 \text{ s}$. The plateau viscosity at high shear rates is taken as the solvent viscosity, which is water.

6.2 Fluid-structure interaction with a non-Newtonian fluid

The equations of motion which govern the motion in a fluid-structure interaction problem consist of the momentum and continuity equation for both the fluid and solid Equations (2.1)-(2.4), a kinematic and a dynamic interface condition Equations (2.11)-(2.12) and the constitutive relations for both fluid and solid Equations (2.5)-(2.10). Since the interface conditions are independent of the constitutive relation of the fluid and solid, a numerical model for fluid-structure interaction will be derived without introducing a material model.

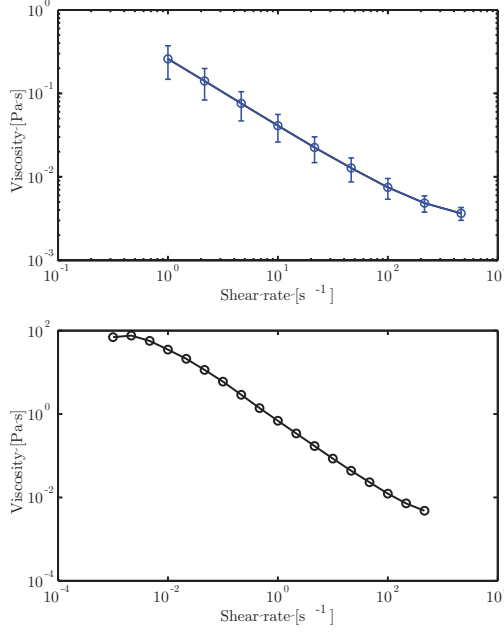


Figure 6.1: Top: The measured saliva viscosity for all test subjects, showing clear shear thinning. The error bars indicate the standard deviation. Bottom: A single measurement of saliva of only one test subject over a wider range, showing a low shear rate plateau of 70 Pa s. Measurements at higher shear rates were not possible due to fluid inertial effects.

These will be introduced at a later stage. The weak form of the momentum and mass balance equations of the fluid and solid with the interface conditions incorporated reads:

Find $\mathbf{u} \in \mathcal{U}$, $p_f \in \mathcal{P}_f$, $\mathbf{d} \in \mathcal{D}$, $p_s \in \mathcal{P}_s$ such that:

$$\begin{aligned}
 & (\mathbf{D}_v, \boldsymbol{\sigma}_f)_{\Omega_f} - (\mathbf{v}, \mathbf{n}_f \cdot \boldsymbol{\sigma}_f)_{\Gamma_{fs}} - (\mathbf{v}, \mathbf{t}_{Nf})_{\Gamma_{Nf}} + \\
 & \kappa \sum_i \sum_j M_{ij}^{-1} (\mathbf{v} \mathbf{n}_f, \phi_i)_{\Gamma_{fs}} : \left(\phi_j, \mathbf{n}_f [\mathbf{u} - \dot{\mathbf{d}}] + [\mathbf{u} - \dot{\mathbf{d}}] \mathbf{n}_f \right)_{\Gamma_{fs}} = 0 \\
 & (q, \nabla \cdot \mathbf{u})_{\Omega_f} = 0 \\
 & (\mathbf{D}_w, \boldsymbol{\sigma}_s)_{\Omega_s} + (\mathbf{w}, \mathbf{n}_f \cdot \boldsymbol{\sigma}_f)_{\Gamma_{fs}} - (\mathbf{w}, \mathbf{t}_{Ns})_{\Gamma_{Ns}} - (\mathbf{w}, \mathbf{f})_{\Omega_s} - \\
 & \kappa \sum_i \sum_j M_{ij}^{-1} (\mathbf{w} \mathbf{n}_f, \phi_i)_{\Gamma_{fs}} : \left(\phi_j, \mathbf{n}_f [\mathbf{u} - \dot{\mathbf{d}}] + [\mathbf{u} - \dot{\mathbf{d}}] \mathbf{n}_f \right)_{\Gamma_{fs}} = 0 \quad (6.1) \\
 & (r, \det \mathbf{F} - 1)_{\Omega_s} = 0, \\
 & \forall \mathbf{v} \in \mathcal{U}, q \in \mathcal{P}_f, \mathbf{w} \in \mathcal{D}, r \in \mathcal{P}_s
 \end{aligned}$$

where the traction term on the solid $\mathbf{n}_s \cdot \boldsymbol{\sigma}_s$ on Γ_{fs} has been replaced by $-\mathbf{n}_f \cdot \boldsymbol{\sigma}_f$. Additionally the extra variable \mathbf{E} which is used for enforcing the kinematic interface condition, has been eliminated from the system, as was done in Section 4.2.3.

If the solid is rigid, this system is shown to be stable for Newtonian, generalized Newtonian and viscoelastic fluids for a large range of the stabilization parameter κ [61]. If the solid is flexible and free to move, the system is shown to converge to a reference solution based on a moving fluid mesh in Chapter 4 for a Newtonian fluid. Combining both results, we expect this system to be able to simulate fluid-structure interaction with complex fluids.

The solid is modeled as an incompressible Mooney-Rivlin solid, thus $\boldsymbol{\sigma}_s = G_{si,I}(\mathbf{B} - \mathbf{I}) + G_{sII}(\mathbf{B}^{-1} - \mathbf{I}) - p_s \mathbf{I}$. For the fluid either a generalized Newtonian, an Oldroyd-B or a Giesekus model is used. Both generalized Newtonian and Giesekus models describe shear-thinning. Both the Oldroyd-B and the Giesekus model are able to describe time-dependent effects and normal stresses in shear flow. The generalized Newtonian model has a shear-rate dependent viscosity; one particular form is the Carreau model (see Section 2.1.1):

$$\eta(\dot{\gamma}) = \eta_\infty + \frac{\eta_0 - \eta_\infty}{\sqrt{(1 + (\lambda\dot{\gamma})^{(1-n)/2})^2}}. \quad (6.2)$$

The Oldroyd-B model gives the fluid stress in terms of the conformation tensor \mathbf{c} which is related to the orientation and stretch of the long molecules, see Section 2.1.1. The fluid stress for this model reads:

$$\boldsymbol{\sigma}_f = 2\eta_\infty \mathbf{D} - p_f \mathbf{I} + G(\mathbf{c} - \mathbf{I}) \quad (6.3)$$

where η_∞ is the viscosity of the solvent, which is water and G is the modulus of the viscoelastic fluid. The conformation tensor has the following weak form of the evolution equation, which has to be solved in addition to the mass and momentum balance equation:

$$\left(\mathbf{s}, \frac{\partial \mathbf{c}}{\partial t} + \mathbf{u} \cdot \nabla \mathbf{c} - \mathbf{L} \cdot \mathbf{c} - \mathbf{c} \cdot \mathbf{L}^T + \frac{1}{\lambda_G} [(\mathbf{c} - \mathbf{I}) + \alpha(\mathbf{c} - \mathbf{I})^2] \right)_{\Omega_f} = 0 \quad (6.4)$$

which is given for the Giesekus model. If $\alpha = 0$ the Oldroyd-B model is obtained.

For the generalized Newtonian model, the constitutive relation Equation (2.6) is used in the weak form of the equations of motion Equation (6.1). This also holds for the viscoelastic model, but then the evolution equation of the conformation tensor has to be solved additionally. In principle also other constitutive relations for the fluid and solid can be used, if the physics demand so.

6.2.1 Time dependence

For both the fluid models a non-linear time-dependent system is found. In order to solve this system we need to apply a proper time-stepping scheme and linearize it. In this chapter only the time discretization of Equation (6.4) will be treated since the time dependency in the kinematic interface condition is treated the same as for the Newtonian case, *i. e.* an Euler backward scheme is used. The linearization of constitutive equation of the solid is also the same as for the Newtonian case, and will therefore not be treated in this chapter. The final set of equations to be solved is: Find $\mathbf{u} \in \mathcal{U}$, $p_f \in \mathcal{P}_f$, $\mathbf{d} \in \mathcal{D}$, $p_s \in \mathcal{P}_s$, $\mathbf{c} \in \mathcal{C}$ such that:

$$\begin{aligned}
& (\mathbf{D}_v, 2\eta(\dot{\gamma})\mathbf{D} - p_f\mathbf{I} + G(\mathbf{c} - \mathbf{I}))_{\Omega_f} - \\
& (\mathbf{v}, \mathbf{n}_f \cdot [2\eta(\dot{\gamma})\mathbf{D} - p_f\mathbf{I} + G(\mathbf{c} - \mathbf{I})])_{\Gamma_{fs}} - (\mathbf{v}, \mathbf{t}_{Nf})_{\Gamma_{Nf}} + \\
& \sum_i \sum_j M_{ij}^{-1} (\mathbf{v}\mathbf{n}_f, \kappa\phi_i)_{\Gamma_{fs}} : \left(\phi_j, \mathbf{n}_f[\mathbf{u} - \dot{\mathbf{d}}] + [\mathbf{u} - \dot{\mathbf{d}}]\mathbf{n} \right)_{\Gamma_{fs}} = 0 \\
& (q, \nabla \cdot \mathbf{u})_{\Omega_f} = 0 \\
& (\mathbf{D}_w, G_s(\mathbf{B} - \mathbf{I}))_{\Omega_s} + \\
& (\mathbf{w}, \mathbf{n}_f \cdot [2\eta(\dot{\gamma})\mathbf{D} - p_f\mathbf{I} + G(\mathbf{c} - \mathbf{I})])_{\Gamma_{fs}} - \\
& (\mathbf{w}, \mathbf{t}_{Ns})_{\Gamma_{Ns}} - (\mathbf{w}, \mathbf{f})_{\Omega_s} - \\
& \sum_i \sum_j M_{ij}^{-1} (\mathbf{w}\mathbf{n}_f, \kappa\phi_i)_{\Gamma_{fs}} : \left(\phi_j, \mathbf{n}_f[\mathbf{u} - \dot{\mathbf{d}}] + [\mathbf{u} - \dot{\mathbf{d}}]\mathbf{n} \right)_{\Gamma_{fs}} = 0 \\
& (r, \det \mathbf{F} - 1)_{\Omega_s} = 0 \\
& \left(\mathbf{s}, \frac{\partial \mathbf{c}}{\partial t} + \mathbf{u} \cdot \nabla \mathbf{c} - \mathbf{L} \cdot \mathbf{c} - \mathbf{c} \cdot \mathbf{L}^T + \frac{1}{\lambda_G} [(\mathbf{c} - \mathbf{I}) + \alpha(\mathbf{c} - \mathbf{I})^2] \right)_{\Omega_f} = 0, \quad (6.5) \\
& \forall \mathbf{v} \in \mathcal{U}, q \in \mathcal{P}_f, \mathbf{w} \in \mathcal{D}, r \in \mathcal{P}_s, \mathbf{s} \in \mathcal{C},
\end{aligned}$$

where the generalized Newtonian case is found for $G = 0$, and the Oldroyd-B case is found for $\eta_0 = \eta_\infty$.

6.2.2 Time discretization

The time dependent term in the kinematic interface condition is discretized in time with a semi-implicit scheme. The evolution equation of the conformation tensor is treated semi-implicitly by taking all convective terms fully implicit and the relaxation terms explicit, which yields the following relation for \mathbf{c} at $t = t^{i+1}$:

$$\frac{\mathbf{c}^{i+1} - \mathbf{c}^i}{\Delta t} + \mathbf{u}^{i+1} \cdot \nabla \mathbf{c}^{i+1} - \mathbf{G}^{i+1} \cdot \mathbf{c}^{i+1} - \mathbf{c}^{i+1} \cdot \mathbf{G}^{T, i+1} + \frac{1}{\lambda_G} [(\mathbf{c}^i - \mathbf{I}) + \alpha(\mathbf{c}^i - \mathbf{I})], \quad (6.6)$$

where Δt is the time-step. The relaxation terms are taken explicitly, since it does not require the linearization of the relaxation terms, which can be complicated for non-linear models. Since the system is solved fully coupled, the viscoelastic contribution to the fluid stress is easily incorporated in the following way:

$$\boldsymbol{\sigma}_f^{i+1} = 2\eta_\infty \mathbf{D}^{i+1} - p_f^{i+1} \mathbf{I} + G(\mathbf{c}^{i+1} - \mathbf{I}). \quad (6.7)$$

In the temporary ALE scheme the velocity in the convective term is replaced by the velocity minus the mesh velocity:

$$\mathbf{u}^{i+1} \cdot \nabla \mathbf{c}^{i+1} \Rightarrow (\mathbf{u}^{i+1} - \mathbf{u}_{\text{mesh}}) \cdot \nabla \mathbf{c}^{i+1}, \quad (6.8)$$

as was done for the inertial terms in Section 4.3.

6.2.3 Stabilization

The simulation of viscoelastic flow is less stable than the simulation of Newtonian flow due to several reasons, which are of a physical or numerical nature. The non-linear constitutive relation is the first, which can lead to non-physical but mathematically valid solutions which are not desired. This problem can be avoided by choosing the proper model and model parameters. Another is the presence of a convective term in the constitutive relation, which can lead to very small stress boundary layers if the flow is convection dominated. This problem is also encountered in flows of a Newtonian fluid where inertia dominates the flow. This is a numerical source of instabilities, since as long as the boundary layer and the element size are of equal order the boundary layer can be captured and the physical solution is found. In viscoelastic fluids however, the boundary layer can be very thin in regions where the velocities are low, but the velocity gradients are large, since the constitutive relation does not contain a diffusive term. Hence stabilization is required, since it is expensive to choose the mesh fine enough to capture this boundary layer.

This is remedied by using the Streamline Upwind Petrov Galerkin method (SUPG) [74], in which the standard test function is replaced by a test function containing the convective term:

$$\left(\mathbf{s} + \tau \mathbf{u}^i \cdot \nabla \mathbf{s}, \frac{\mathbf{c}^{i+1} - \mathbf{c}^i}{\Delta t} + \mathbf{u}^{i+1} \cdot \nabla \mathbf{c}^{i+1} - \mathbf{L}^{i+1} \cdot \mathbf{c}^{i+1} - \mathbf{c}^{i+1} \cdot \mathbf{L}^{i+1,T} + \frac{\mathbf{c}^i - \mathbf{I}}{\lambda_{\text{OB}}} \right)_{\Omega_f} = 0 \quad (6.9)$$

where τ is a stabilization parameter which scales with $\frac{h}{U}$ where h is the element size in the direction of the velocity and U the typical velocity. The typical velocity is the average of the velocity magnitude over the integration points. In the neighborhood of the interface however the velocities can be low which

would lead to too high values of τ . Here $\tau = 0.5\Delta t$, as was done by Choi *et al.* [62]. The switchover between the two ways of scaling τ depends on the value of the Courant number C , which is the ratio between the velocity and the discrete velocity $C = h/\Delta t$:

$$\tau = \begin{cases} \frac{h}{2U} & C \geq 1 \\ \frac{\Delta t}{2} & C < 1 \end{cases} \quad (6.10)$$

In order to stabilize the flow of a viscoelastic fluid, \mathbf{G} an extra representation of velocity gradient tensor \mathbf{L} is added to the system, which is known as DEVSS-G [75]. An additional term in the momentum equation of the fluid is added and all occurrences of \mathbf{L} in the constitutive relation are replaced by \mathbf{G} . This leads to the following additional terms in the momentum equation:

$$\dots \alpha \left(\mathbf{D}_v^T, \mathbf{L}^{i+1} - \mathbf{G}^{i+1} \right)_{\Omega_{j,f}} \dots, \quad (6.11)$$

where α is a stabilization parameter which is usually chosen equal to the polymer viscosity $G\lambda_{OB}$ [76]. Note that in case \mathbf{L} and \mathbf{G} are identical, the stabilization term disappears making the method consistent.

6.2.4 Spatial discretization

Since the DEVSS-G problem is a mixed problem, the interpolation functions for the velocity, fluid pressure, velocity gradient problem cannot be chosen independently. In addition the shape functions for \mathbf{c} are also related. For $(\mathbf{u}, p, \mathbf{G}, \mathbf{c})$ Baaijens *et al.* [76] found that $Q_2^9 Q_1^4 Q_1^4 Q_1^4$ interpolation is stable, hence this combination of shape functions will be used here. Since the solid is also incompressible, the shape functions for the displacement and solid pressure are chosen to be $Q_2^9 Q_1^9$, which fulfills the Babuska-Brezzi condition. The extra rate-of-deformation tensor \mathbf{E} will be interpolated discontinuously having the same order as the velocity, yielding a $Q_2^{9,d}$ element. Since the velocity, fluid pressure, conformation tensor and velocity gradient are computed on a fixed grid, whilst the interface moves, these variables show a jump at the interface. Hence XFEM will be used to model this jump. This means that the trial and

testfunctions are defined in the following way:

$$\mathbf{u} \approx \sum_{i=1}^{Nu} \phi_i(\mathbf{x}) \mathbf{U}_i; \quad \mathbf{U}_i(\mathbf{x}) = \mathbf{u}_i H(\mathbf{x}) \quad (6.12)$$

$$p_f \approx \sum_{i=1}^{Npf} \psi_i(\mathbf{x}) P_{f,i}; \quad P_{f,i}(\mathbf{x}) = p_{f,i}(\mathbf{x}) H(\mathbf{x}), \quad (6.13)$$

$$\mathbf{G} \approx \sum_{i=1}^{Ng} \nu_i(\mathbf{x}) \mathbf{G}_{2,i}; \quad \mathbf{G}_{2,i}(\mathbf{x}) = \mathbf{G}_i(\mathbf{x}) H(\mathbf{x}), \quad (6.14)$$

$$\mathbf{c} \approx \sum_{i=1}^{Nc} \xi_i(\mathbf{x}) \mathbf{C}_i; \quad \mathbf{C}_i(\mathbf{x}) = \mathbf{c}_i(\mathbf{x}) H(\mathbf{x}), \quad (6.15)$$

$$\mathbf{d} \approx \sum_{i=1}^{Nd} \mu_i(\mathbf{x}) \mathbf{D}_i, \quad (6.16)$$

$$p_s \approx \sum_{i=1}^{Nps} \psi_{f,i}(\mathbf{x}) P_{s,i}, \quad (6.17)$$

$$\mathbf{v} \approx \sum_{i=1}^{Nu} \phi_i(\mathbf{x}) \mathbf{V}_i; \quad \mathbf{V}_i(\mathbf{x}) = \mathbf{V}_i H(\mathbf{x}) \quad (6.18)$$

$$q \approx \sum_{i=1}^{Npf} \psi_i(\mathbf{x}) Q_i; \quad Q_i(\mathbf{x}) = q_i(\mathbf{x}) H(\mathbf{x}), \quad (6.19)$$

$$\mathbf{H} \approx \sum_{i=1}^{Ng} \nu_i(\mathbf{x}) \mathbf{H}_{2,i}; \quad \mathbf{H}_{2,i}(\mathbf{x}) = \mathbf{H}_i(\mathbf{x}) H(\mathbf{x}), \quad (6.20)$$

$$\mathbf{s} \approx \sum_{i=1}^{Nc} \xi_i(\mathbf{x}) \mathbf{S}_i; \quad \mathbf{S}_i(\mathbf{x}) = \mathbf{s}_i(\mathbf{x}) H(\mathbf{x}), \quad (6.21)$$

$$\mathbf{w} \approx \sum_{i=1}^{Nd} \mu_i(\mathbf{x}) \mathbf{W}_i, \quad (6.22)$$

$$r \approx \sum_{i=1}^{Nps} \psi_{f,i}(\mathbf{x}) R_i, \quad (6.23)$$

where $H(\mathbf{x})$ is the Heaviside function defined in Equation (4.12). Using these trail and testfunctions and linearization, the discretized system is represented

by:

$$\begin{bmatrix} A + C + L_f + O_f & B^T + M_f & D^T & F + N_f & 0 & 0 & 0 \\ B & 0 & 0 & 0 & 0 & 0 & 0 \\ D & 0 & E & 0 & 0 & 0 & 0 \\ G & 0 & H & I & 0 & 0 & 0 \\ L_s O_s & M_s & 0 & N_s & J & K^T & 0 \\ 0 & 0 & 0 & 0 & K & 0 & 0 \end{bmatrix} \begin{bmatrix} \mathbf{u} \\ p_f \\ \mathbf{G} \\ \mathbf{c} \\ \mathbf{d} \\ p_s \end{bmatrix} = \begin{bmatrix} f + g_f \\ 0 \\ 0 \\ h \\ g_s + i + j \\ k \end{bmatrix} \quad (6.24)$$

where the submatrices $A - O_s$ are defined as:

$$A = \left(\nabla \phi^T + \nabla \phi, \frac{1}{2} \eta(\dot{\gamma}_j) (\nabla \phi + \nabla \phi^T) \right)_{\Omega_f} \quad (6.25)$$

$$B = -(\psi_f^T, \nabla \phi)_{\Omega_f} \quad (6.26)$$

$$C = \left(\nabla \phi^T + \nabla \phi, \frac{\alpha}{4} (\nabla \phi + \nabla \phi^T) \right)_{\Omega_f} \quad (6.27)$$

$$D = -\left(\nu^T + \nu, \frac{\alpha}{4} (\nabla \phi + \nabla \phi^T) \right)_{\Omega_f} \quad (6.28)$$

$$E = \left(\nu^T + \nu, \frac{\alpha}{4} (\nu + \nu^T) \right)_{\Omega_f} \quad (6.29)$$

$$F = (\nabla \phi^T + \nabla \phi, G\xi)_{\Omega_f} \quad (6.30)$$

$$G = (\xi^T + \tau \mathbf{u}_j \cdot \nabla \xi^T, \phi \cdot \nabla \mathbf{c}_j)_{\Omega_f}, \quad (6.31)$$

$$H = (\xi^T + \tau \mathbf{u}_j \cdot \nabla \xi^T, -\nu \cdot \mathbf{c}_j - \mathbf{c}_j \cdot \nu^T)_{\Omega_f}, \quad (6.32)$$

$$I = \left(\xi^T + \tau \mathbf{u}_j \cdot \nabla \xi^T, \frac{\xi}{\Delta t} + \mathbf{u}_j \cdot \nabla \xi - \mathbf{G}_j \cdot \xi - \xi \cdot \mathbf{G}_j^T \right)_{\Omega_f}, \quad (6.33)$$

$$J = (-\sigma_{s,j}^T \cdot (\nabla \mu^T \nabla \mu)^T + \sigma_{s,j}^T \cdot \nabla \mu^T \nabla \mu + \nabla \mu^T \cdot \mathbf{C} \cdot \nabla \mu)_{\Omega_s}, \quad (6.34)$$

$$K = -(\psi_s^T, \nabla \mu)_{\Omega_s}, \quad (6.35)$$

$$L_f = -(\phi^T, \mathbf{n}_{f,j} \cdot [\eta(\dot{\gamma}_j) (\nabla \phi + \nabla \phi^T)])_{\Gamma_{fs}}, \quad (6.36)$$

$$M_f = (\phi^T, \mathbf{n}_{f,j} \cdot [\psi_f \mathbf{I}])_{\Gamma_{fs}}, \quad (6.37)$$

$$N_f = -(\phi^T, \mathbf{n}_{f,j} \cdot [G\xi])_{\Gamma_{fs}}, \quad (6.38)$$

$$L_s = (\mu^T, \mathbf{n}_{f,j} \cdot [\eta(\dot{\gamma}_j) (\nabla \phi + \nabla \phi^T)])_{\Gamma_{fs}}, \quad (6.39)$$

$$M_s = -(\mu^T, \mathbf{n}_{f,j} \cdot [\psi_f \mathbf{I}])_{\Gamma_{fs}}, \quad (6.40)$$

$$N_s = (\mu^T, \mathbf{n}_{f,j} \cdot [G\xi])_{\Gamma_{fs}}, \quad (6.41)$$

$$O_f = \sum_k \sum_l M_{kl}^{-1} (\phi^T \mathbf{n}_{f,j} \cdot \kappa \phi_k)_{\Gamma_{fs}} : (\phi_l, \mathbf{n}_{f,j} \phi + \phi \mathbf{n}_{f,j})_{\Gamma_{fs}}, \quad (6.42)$$

$$O_s = -\sum_k \sum_l M_{kl}^{-1} (\mu^T \mathbf{n}_{f,j} \cdot \kappa \phi_k)_{\Gamma_{fs}} : \left(\phi_l, \mathbf{n}_{f,j} \frac{\mu}{\Delta t} + \frac{\mu}{\Delta t} \mathbf{n}_{f,j} \right)_{\Gamma_{fs}}, \quad (6.43)$$

where $\boldsymbol{\sigma}_{s,j} = G_{sI} (\mathbf{B}_j - \mathbf{I}) + G_{sII} (\mathbf{B}_j^{-1} - \mathbf{I}) - p_{s,j} \mathbf{I}$ is the solid Cauchy stress at the previous iteration and the fourth-order tensor \mathbf{C} is a linearization of the constitutive equation. The right-hand side vectors $f - j$ have been defined as:

$$f = (\phi^T, \mathbf{t}_{\text{Nf}})_{\Gamma_{\text{Nf}}}, \quad (6.44)$$

$$g_{\text{f}} = \sum_k \sum_l M_{kl}^{-1} (\phi^T \mathbf{n}_{\text{f},j}, \kappa \phi_k)_{\Gamma_{\text{fs}}} : \left(\phi_l, \mathbf{n}_{\text{f},j} \frac{\mathbf{d}_j - \mathbf{d}^i}{\Delta t} + \frac{\mathbf{d}_j - \mathbf{d}^i}{\Delta t} \mathbf{n}_{\text{f},j} \right)_{\Gamma_{\text{fs}}}, \quad (6.45)$$

$$g_{\text{t}} = - \sum_k \sum_l M_{kl}^{-1} (\mu^T \mathbf{n}_{\text{f},j}, \kappa \phi_k)_{\Gamma_{\text{fs}}} : \left(\phi_l, \mathbf{n}_{\text{f},j} \frac{\mathbf{d}_j - \mathbf{d}^i}{\Delta t} + \frac{\mathbf{d}_j - \mathbf{d}^i}{\Delta t} \mathbf{n}_{\text{f},j} \right)_{\Gamma_{\text{fs}}}, \quad (6.46)$$

$$h = \left(\xi^T + \tau_j \mathbf{u}_j \cdot \nabla x_i^T, \frac{\mathbf{c}^i}{\Delta t} + \mathbf{u}_j \cdot \nabla \mathbf{c}_j - \mathbf{G}_j \cdot \mathbf{c}_j - \mathbf{c}_j \cdot \mathbf{G}_j^T - \frac{\mathbf{c}_j - \mathbf{I} - \alpha(\mathbf{c}_j - \mathbf{I})^2}{\lambda_{\text{G}}} \right)_{\Omega_{\text{f}}}, \quad (6.47)$$

$$i = (\mu^T, \mathbf{t}_{\text{Ns}})_{\Gamma_{\text{Ns}}}, \quad (6.48)$$

$$j = (\mu^T, \mathbf{f})_{\Omega_{\text{s}}}, \quad (6.49)$$

$$k = (\psi_s^T, (\det \mathbf{F}_j - 1) / \det \mathbf{F}_j)_{\Omega_{\text{s}}}. \quad (6.50)$$

Since the evolution equation of \mathbf{c} is time dependent, and XFEM is used, information from the previous time steps and iterative steps was found at the current iterative step by using a temporary ALE scheme as was used for the systems with fluid inertia in Section 4.3.2.

6.2.5 Solution procedure

The fluid-structure interaction problem in the previous chapters was solved in a fully coupled manner since this is more stable than solving them decoupled. In case viscoelastic fluid models are used, the evolution equation for the conformation tensor can be solved separately or at the same time as the fluid-structure interaction problem. The choice for an explicit (decoupled) or implicit (coupled) approach again depends on the time-scales involved. The time-scale of the fluid is the relaxation time λ_{OB} , for an Oldroyd-B or λ_{G} for a Giesekus fluid, and the time-scale of the fluid-structure interaction problem is t_3 , defined as $\frac{\eta}{G_s}$. Since we would like to study a wide range of relaxation times of the fluid, whilst keeping t_3 fixed, a fully coupled approach is the safest, since it is more stable than the decoupled approach. It however requires the

solution of a much larger system, which makes it computationally much more expensive.

6.2.6 Local mesh refinement

Initial tests of the coupled approach presented in the previous section revealed that the computations at a mesh size of $(N_x, N_y) = (91, 91)$ that the solution of a single time increment took about 6 minutes. The Newtonian simulations typically required 1000 to 10000 time-steps, which means that the viscoelastic simulations would take between 5 and 50 days to complete, which is not acceptable. The main reason for the long simulation time is the large amount of fluid elements. Since each fluid element contains degrees of freedom for the velocity, pressure, velocity gradient and conformation tensor, a reduction of the amount of elements will reduce the amount of degrees of freedom accordingly. Although the number of elements should be reduced, the accuracy of the solution should not suffer. This is accomplished by using large elements in regions far away from the cilium and small elements near the cilium. We propose the following simple and robust mesh adaptation method.

Two meshes spanning the fluid domain are generated. The second mesh M_2 is n times more refined than mesh M_1 . This means that $n \times n$ elements of M_2 exactly overlap with one element in M_1 . Initially all elements of M_1 are used for the computation, and the elements of M_2 are not. At parts of the mesh where refinement is required, such as near Γ_{fs} , elements of M_2 are marked for computation and the corresponding elements of M_1 are not marked any longer, leading to the situation depicted in Figure 6.2. The part of the fluid domain connected to M_1 is Ω_{f,M_1} and the part of the fluid domain connected to M_2 is Ω_{f,M_2} and $\Omega_f = \Omega_{f,M_1} \cup \Omega_{f,M_2}$. The common boundary between these domains is $\Gamma_{M_{12}}$. At $\Gamma_{M_{12}}$ the same kinematic and dynamic interface conditions hold as for the fluid-structure interaction problem, namely continuity of the velocity and traction, Equations (2.11) and (2.12). These conditions couple velocity and pressure on one side to velocity and pressure on the other side. For viscoelastic flow an extra condition is required, which defines the conformation tensor on the inflow part of either Ω_{f,M_1} or Ω_{f,M_2} . Inflow is defined as $\mathbf{n}_1 \cdot \mathbf{u}_1 < 0$, with \mathbf{n}_1 the outward normal of Ω_{f,M_1} on $\Gamma_{M_{12}}$ and \mathbf{u}_1 the velocity in Ω_{f,M_1} . The velocity gradient tensor \mathbf{G} is not coupled at the interface, but $\nabla \mathbf{u}^T$ is through the treatment of the kinematic and dynamic interface conditions. For a viscoelastic problem, the conformation tensor is coupled at the inflow part by adding the following term to the weak form of the equations of motion:

$$\dots + (\mathbf{v}_1, \nu \mathbf{n}_1 \cdot (\mathbf{c}_1 - \mathbf{c}_2))_{\Gamma_{M_{12}}} + (\mathbf{v}_2, (1 - \nu) \mathbf{n}_2 \cdot (\mathbf{c}_2 - \mathbf{c}_1))_{\Gamma_{M_{12}}} \dots \quad (6.51)$$

where the subscripts 1 and 2 denote the coarse and fine parts of the domain. The parameter ν determines on which subdomain the inflow condition for the con-

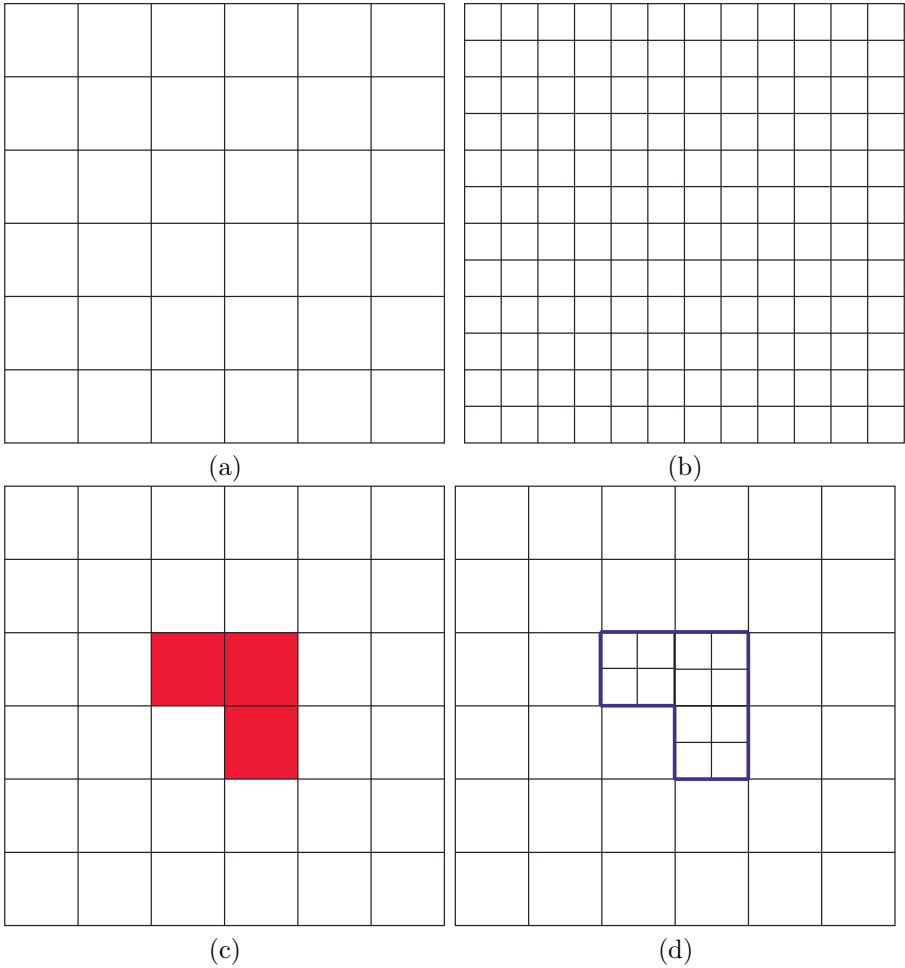


Figure 6.2: The coarse (a) and fine (b) meshes which serve as a starting point for the local mesh refinement technique. Several elements are selected for refinement (c) and these refined elements are combined with the other non-refined elements (d). At the interface (depicted in blue) the coarse and fine domains are coupled via interface conditions.

formation tensor should be applied:

$$\nu = \begin{cases} 1 & \text{if } \mathbf{n}_1 \cdot \mathbf{u}_1 < 0, \\ 0 & \text{if } \mathbf{n}_1 \cdot \mathbf{u}_1 \geq 0. \end{cases} \tag{6.52}$$

The method presented above has one level of refinement, which is sufficient for our purpose. The extension to multiple levels is relatively easy, by only

introducing multiple domains of different refinement and multiple boundary integrals in the weak form.

6.3 Validation

An elastic flap ($L = 0.5H, T_c = 0.02H$) in a channel with geometries $H = W = 1 \cdot 10^{-3}$ m is subjected to a prescribed velocity on the left boundary: $u_{\text{in}} = 600y(H - y)e_x$. The flap is rounded off with radius $r = 0.0098H$ and located at the center of the channel, see Figure 6.3. The fluid viscosity $\eta_\infty = 1 \cdot 10^{-3}$ Pa s, and the Oldroyd-B model is used with a relaxation time $\lambda_{\text{OB}} = 0.1$ s, $G = 1$ Pa, $G_{sI} = 1 \cdot 10^4$ Pa and $G_{sII} = 0$ Pa. The typical shear-rate $\dot{\gamma} = U/H = 10^{-4}/10^{-3} = 0.1$, with the typical velocity $U = 10^{-4}$ m s $^{-1}$. This results in a Weissenberg number of $\text{Wi} = \lambda_{\text{OB}}\dot{\gamma} = 0.01$, which should not cause numerical difficulties found in very elastic flows. Note however that this is the global Weissenberg number and that locally the fluid can behave elastically due to high local deformation rates. At inflow $\mathbf{n}_f \cdot \mathbf{u} < 0$, $\mathbf{c} = \mathbf{I}$. The right boundary is taken stress-free: $\mathbf{n} \cdot \boldsymbol{\sigma} = \mathbf{0}$. The velocity is imposed on the fluid, instead of a pressure drop as was done in the test problem of Section 4.5.2, since this will prescribe the global kinematics of the flow. If a pressure drop would be applied, and the solvent viscosity is low, very large deformations are expected in the beginning, since both fluid and solid behave fully elastically at short time-scales. Various variables are given along the cilium boundary at $t = 10^{-1}$ for $\Delta t = 10^{-2}$ in Figure 6.4. A typical solution for c_{xx} is shown in Figure 6.5. Near the tip of the cilium there is a region where the fluid is compressed (left) and where the fluid is extended (right). This is reflected in compression and stretch of the polymer chains, leading to c_{xx} smaller than one and larger than one respectively.

6.3.1 Local mesh refinement

The local mesh refinement scheme of the previous section is tested by using a single refined element in Couette flow of a Oldroyd-B fluid of $\text{Wi} = \lambda_{\text{OB}}U/H = 10$, where λ is the relaxation time of the fluid, U the applied velocity and H the height of the channel. The flow is periodic in the horizontal direction. An initial disturbance is placed on the initial value of the conformation tensor of order $\mathcal{O}(10^{-3})$. The mesh used for this computation is shown in Figure 6.6. The proposed method is compared with a regular mesh where the periodicity is enforced with Lagrange multipliers and a regular mesh where periodicity is enforced with the Lesaint-Raviart coupling of Equation (6.51). For a stable method the initial disturbance should damp out in time. Since the growth rate of a possibly unstable system can be very low, the simulation is performed for at time of $30\lambda_{\text{OB}}$. The difference of the solution with the steady state value \mathbf{c}_s , is computed and given in Figure 6.7. In addition to the numerical

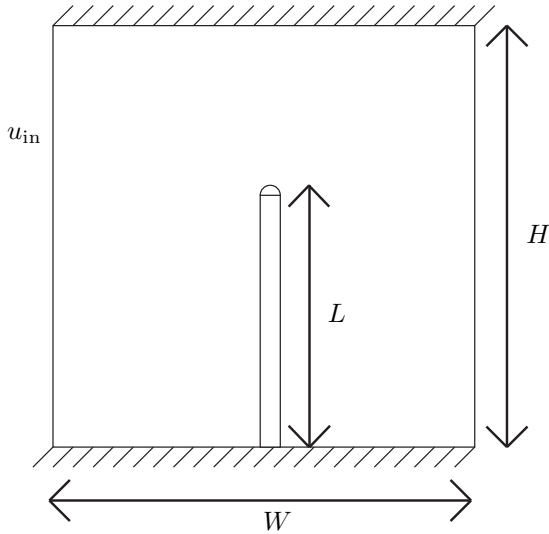


Figure 6.3: Imposed flow over a beam of length $L = 0.5H$ in channel with height H and length W . The thickness of the beam is $0.02H$.

schemes the transient behavior as predicted by Kupferman [77] and the slowest decaying eigenmode predicted by Gorodtsov and Leonov [78] are shown. Both the regular DEVSS-G/SUPG with Lagrange multipliers and Lesaint-Raviart upwinding for the periodic boundary condition, nicely follow the transient form predicted by Kupferman and they eventually follow the slowest decaying mode predicted by Gorodtsov and Leonov. The local mesh refinement scheme shows some shoulder after the initial growth and subsequent decay, but eventually follows the slowest eigenmode. Therefore this refinement scheme is stable, at least for this refinement level and this amount of refined elements.

The local mesh refinement has also been applied to the viscoelastic cilium model. A layer around the cilium is 3 times more finer than the surrounding mesh, and a simulation of a Giesekus fluid ($\alpha = 0.05$) at $Wi = 0.1$ is shown in Figure 6.8. The simulation is free from oscillations and the mesh is locally refined around the cilium as can be seen in the figure.

6.4 Conclusion

In this chapter the model for fluid-structure interaction with a Newtonian fluid, which was presented in previous chapters, was extended to non-Newtonian fluids. This allows us to study the differences in flow and cilium motion between a Newtonian and a non-Newtonian fluid. This is practically relevant since in practical microfluidic systems, biological fluids such as saliva are analysed,

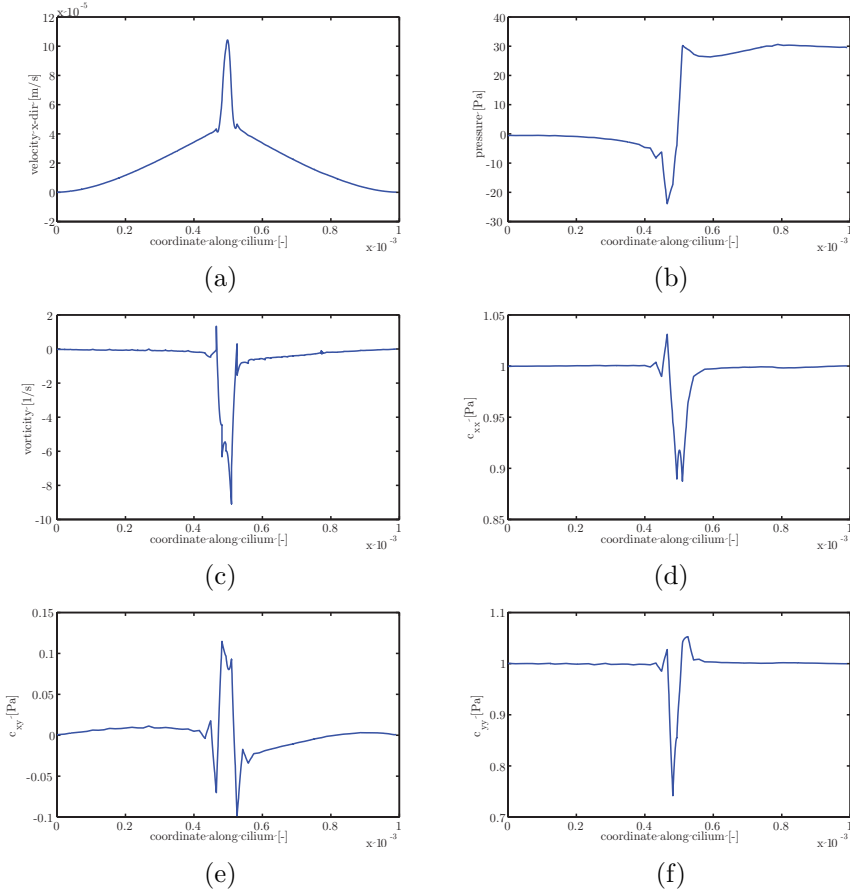


Figure 6.4: Various variables along the cilium boundary: (a) x -velocity, (b) pressure, (c) vorticity, (d) c_{xx} , (e) c_{xy} and (f) c_{yy} .

and saliva has a different rheology than its main constituent water, which is Newtonian. The most prominent non-Newtonian feature of polymer solutions, among which saliva, is shear-thinning, which is the decrease of the shear viscosity under steady shear. This effect was studied by performing steady state shear tests on human whole saliva, and it was found that the shear viscosity at low shear rates $\dot{\gamma} < 10^{-2} \text{ s}^{-1}$ was about 70 Pa s. At higher shear-rates the viscosity scaled with $\dot{\gamma}^{-0.8}$, until it reaches the shear viscosity of water which is 1 mPa s. Thus at low shear-rates the viscosity is a factor 70.000 larger than that of water, while there is a large range where it decreases rapidly from this value to that of water. In order to model shear-thinning behavior two non-Newtonian models were used, a generalized Newtonian model which is

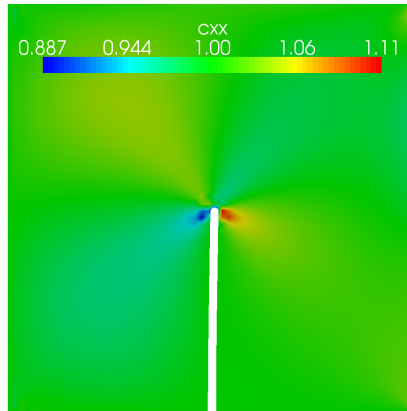


Figure 6.5: A typical solution of c_{xx} for the XFEM method for $Wi=0.01$ at $t = 10^{-1}$.

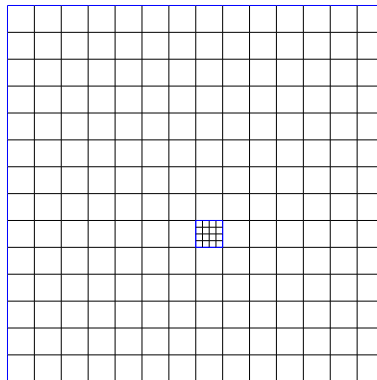


Figure 6.6: The locally refined mesh used for testing the stability of this refinement method in Couette flow.

only capable of modeling the decrease in shear viscosity, and the Oldroyd-B model, which is capable of capturing time-dependent effects and normal stresses in shear. The first can only describe the steady-state viscosity decrease, while the Oldroyd-B model can describe elastic effects. In order to use these models the fluid-structure interaction model of Chapter 4 was adapted. For the generalized Newtonian model the changes are relatively simple, whilst for the Oldroyd-B model additional stabilization terms have to be added to the discretized momentum and conformation evolution equation, known as the DEVSS-G/SUPG method for solving viscoelastic flow.

In order to avoid stability problems due to splitting the system into a fluid

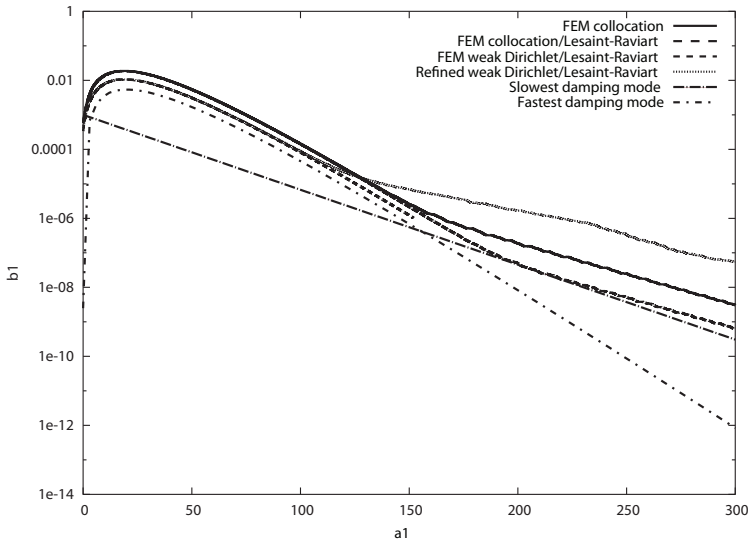


Figure 6.7: The growth and decline of an initial disturbance on the conformation tensor for Couette flow for different numerical schemes.

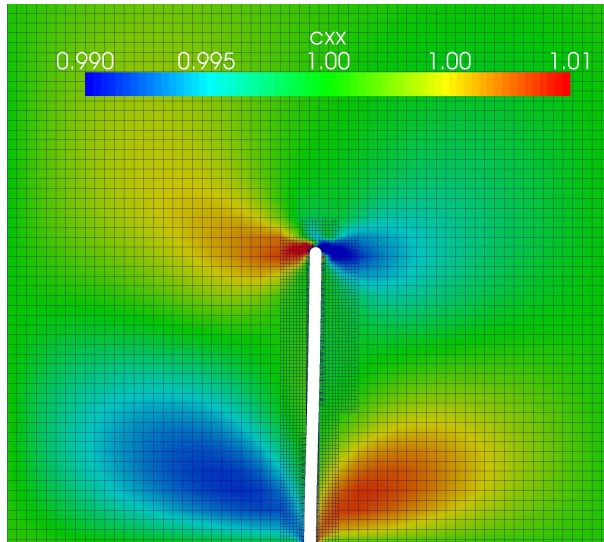


Figure 6.8: The xx -component of the conformation tensor for prescribed flow over a cilium of a Giesekus fluid for $\alpha = 0.05$ and $Wi = 0.1$.

and a solid problem and solving them sequentially, the resulting set of equa-

tions is solved simultaneously, resulting in a large system with many unknowns. The viscoelastic model was shown to be stable by solving flow over an elastic flap with $Wi=0.01$.

Since the fully coupled set of equations has many unknowns per element, and fine meshes are required for accurate results near the cilium, the computation of a single actuation cycle can take several weeks. Since large gradients are present mainly near the cilium, a local mesh refinement strategy is proposed, which reduces the amount of unknowns and thus computation time. The stability of this local refinement scheme was tested by checking how an initial disturbance in the conformation tensor damps out for a Couette flow (without fluid-structure interaction). Even for very long simulations the refinement scheme is stable and finally reaches the predicted damping slope. This scheme is also tested in a situation where an external flow is applied over an elastic flap, and a stable solution is also shown for a Giesekus fluid at $Wi=0.1$.

Chapter 7

Simulation of transport by artificial cilia: non-Newtonian fluids

In the previous chapter a model for the flow of complex fluids generated by artificial cilia was introduced. In this chapter this model will be used for the simulation of such flows, and differences between the flow of a Newtonian and a non-Newtonian fluid will be studied. Since complex fluids show a time-dependent behavior, an extra time-scale is introduced into the system. If this time-scale is much shorter than the actuation time-scale, the fluid stresses build up very fast and time-dependent effects due to the rheology of the fluid are minimal. If the fluid time-scale is much longer than the actuation time-scale, time-dependent effects govern the motion of the cilia and the fluid. So the ratio between the actuation period and the fluid-structure time-scale $t_3 = \frac{\eta}{G_s}$ in the Newtonian case, the ratio between the relaxation time λ_{OB} and the actuation period also becomes important for complex fluids.

7.1 Transport of a generalized Newtonian fluid

In Chapter 5 it was shown for Newtonian fluids, that the typical time scale at which a cilium moves is $t_3 = \frac{\eta}{G_s}$, for sufficiently stiff cilia. For Newtonian fluids the viscosity η is constant, but for non-Newtonian fluids it is not, and depends on the shear-rate $\dot{\gamma}$. In addition to the time-scale, the initial velocity $U = \frac{f_0 L^2}{\eta}$ also depends on the viscosity. It is therefore useful to look at the rate dependence of the viscosity. If we define a characteristic shear-rate by

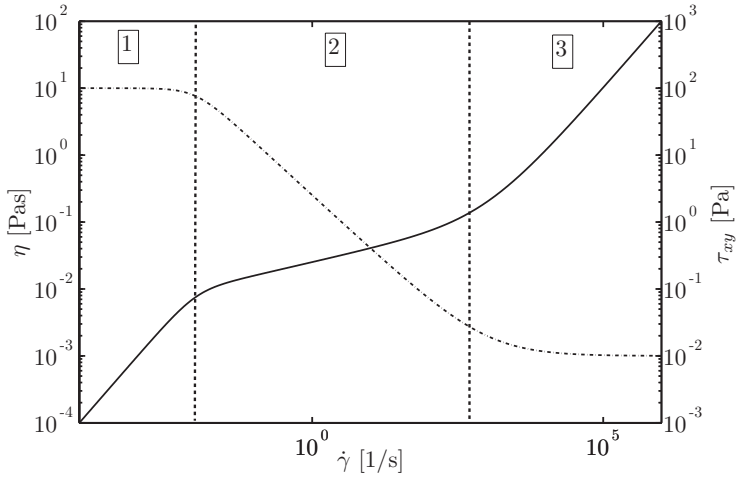


Figure 7.1: The viscosity (dashed line, left axis), as shear stress (solid line, right axis) for a shear-thinning fluid. Three regions are present: (1) Newtonian low shear-rate plateau, (2) shear-thinning region and (3) high shear-rate plateau.

$\dot{\gamma} = \frac{U}{L} = \frac{f_0 L}{\eta(\dot{\gamma})}$, then we obtain a characteristic shear stress of $\tau_{xy} = \eta(\dot{\gamma})\dot{\gamma} = f_0 L$. The characteristic shear-rate and viscosity at this shear stress can now be found in Figure 7.1, where a typical viscosity and corresponding shear stress profile are given for a shear-thinning fluid. Although it is important to get estimates of the characteristic displacement, velocity and time scale, it is much more interesting to see the influence of changes of these variables due to the changes in f_0 because this is the parameter that can be controlled in practice. In shear-thinning fluids, three regions can be distinguished (see Figure 7.1): region 1 where τ_{xy} and $\dot{\gamma}$ are low and η is high and independent of $\dot{\gamma}$, region 2, where η rapidly decreases with increasing shear-rate, this is the shear-thinning region, and region 3 where τ_{xy} is large and the viscosity independent of $\dot{\gamma}$, but lower than in region 1. A change of f_0 within regions 1 and 3 will only result in a small change of characteristic time-scale, velocity and displacement; the viscosity remains the same however, hence this situation is the same as for a Newtonian fluid. In the second region a change in f_0 leads to large changes in η and therefore the characteristic velocity and time scale will change too, far more than in the first and third region.

We anticipate that, for the effect of the non-Newtonian behavior to be largest, possibly resulting in enhanced net flow, the dynamic contrast between the forward and the backward stroke of the cilia should be large, and therefore different forces should be applied shifting back and forth between different positions in region 2 of Figure 7.1. To study this, we propose the following

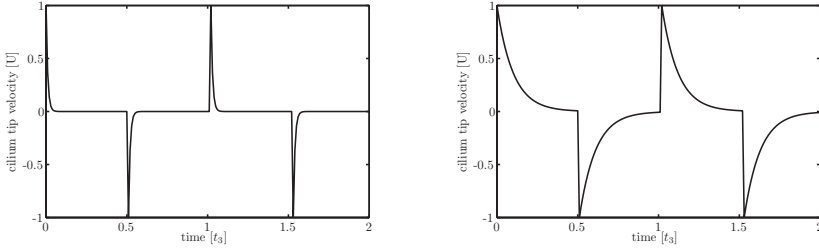


Figure 7.2: Cilium tip velocity as function of time for $R_5 < 1, R_6 < 1$ (left) and $R_5 > 1, R_6 > 1$ (right).

actuation scheme; apply a large actuation force f_1 for a time Δt_1 as forward stroke and a smaller force f_2 for Δt_2 as a backward stroke. Both forces only act in horizontal direction, and are related as follows: $f_1/f_2 = (\Delta t_2)/(\Delta t_1)$. We therefore have three free parameters: f_1, f_2 and Δt_1 . Since the characteristic time-scale is t_3 , and the typical time-scales of applying the force are Δt_1 and Δt_2 , two new dimensionless groups appear:

$$R_5 = \frac{t_3}{\Delta t_1}, \quad (7.1)$$

$$R_6 = \frac{t_3}{\Delta t_2}, \quad (7.2)$$

which give the ratios of the characteristic time-scale of the system to the time-scales of the applied force. If both are smaller than unity the cilium moves to its steady state position and remains there for the remainder of the stroke. If R_5 or R_6 are larger than unity the steady state position is not reached before the end of the applied force. See Figure 7.2 for a schematic view of the two situations. From the scaling analysis it follows that for a given system, the actuation force governs the time scale of movement, *i.e.* it controls the dynamics of the system. In particular, if the two non-dimensional numbers R_5 and R_6 are different, the dynamical behavior of the system is different between the forward and the backward strokes, which can lead to asymmetric cilia motion. This is true for a Newtonian as well as for a shear-thinning fluid. However for a shear-thinning fluid this difference can be much more pronounced since the characteristic time scale t_3 itself depends on the time scale of the applied force through its viscosity dependence, as explained above. The relation between R_5 and R_6 is chosen as follows:

$$R_5 = \frac{\eta_1}{\eta_2} \sqrt{\frac{f_1}{f_2}} R_6 \quad (7.3)$$

where η_1 and η_2 are the typical viscosities in forward and backward stroke respectively. So the force ratio has a smaller influence on the difference in

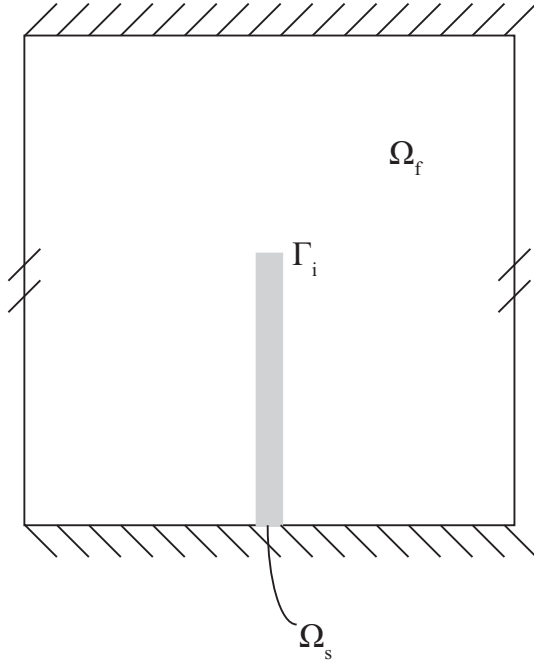


Figure 7.3: The modeled periodic domain with a single cilium. The fluid domain (Ω_f), grey solid domain (Ω_s) and the cilium boundary (Γ_i) are indicated in the figure. The cilium has length L and thickness T_c , the domain is square and has dimensions $(2L \times 2L)$.

dynamics during forward and backward stroke than the viscosity ratio. Hence even for small force ratios large differences in dynamics can be apparent when the fluid is shear-thinning. We have carried out simulations for a Newtonian liquid with $\eta_0 = 0.1 \text{ Pa s}$ and a shear thinning liquid with the parameters given in Section 6.1.2 ($n = 0.2, \eta_0 = 70 \text{ Pa s}, \eta_\infty = 1 \text{ mPa s}, \lambda = 100 \text{ s}$). The domain is $1 \text{ mm} \times 1 \text{ mm}$, the cilium is $L \times T_c = 0.5 \text{ mm} \times 10 \mu \text{ m}$, see Figure 7.1 and the actuation force is varied in order to investigate its influence. Simulations have been performed for 20 cycles, in order to exclude transient effects. Simulations have been performed for $\Delta t_1 = 0.02 \text{ s}$, $\Delta t_2 = 0.04 \text{ s}$ and for four different actuation forces $f_1 = [2, 3, 4, 5] \cdot 10^5 \text{ Nm}^{-3}$. This results in $f_2 = [1, 1.5, 2, 2.5] \cdot 10^5 \text{ Nm}^{-3}$. The cilium trajectories for both the Newtonian and shear-thinning fluid and an actuation force of $f_1 = 4 \cdot 10^5 \text{ Nm}^{-3}$ are shown in Figure 7.4. The red positions are obtained during forward motion, the blue positions during backward motion. While the path of the cilium is more or less symmetric around the initial configuration for the Newtonian fluid, the path in the shear-thinning fluid is tilted in the forward stroke direction. This is a direct

consequence of the different viscosities and time-scales during the forward and backward stroke. Since the forward stroke involves a higher force, the time-scale is shorter and hence there will be more deflection. During the backward stroke the force is lower and the time-scale is larger. For the Newtonian fluid $R_5 = \sqrt{2}R_6$, for this actuation scheme, so the dynamics are different during forward and backward stroke. A similar analysis for the shear-thinning fluid requires information on the actual viscosities, which will be shown in the next paragraph. A typical viscosity profile at the start of forward and backward



Figure 7.4: The forward (blue) and backward (red) stroke of a cilium in a Newtonian fluid (left) and the shear-thinning fluid (right). Both have the same actuation cycle with $f_1 = 4 \cdot 10^5 \text{ Nm}^{-3}$.

actuation is shown in Figure 7.5, from which it is clear that the lowest viscosity found in forward stroke is about 10 times lower than the viscosity found in the backward stroke. This leads to $R_5 = 0.1\sqrt{2}R_6$, so a ten times smaller ratio than for the Newtonian case. It is also clear that the viscosity itself is not constant over the entire domain, thus leading to different flow profiles further away from the cilium. This has also been observed by Smith *et al.* [79] in a Maxwell fluid, where particle motion was different for a Newtonian liquid than for the Maxwell fluid. The net flow produced during one actuation cycle is computed at the 11th cycle. The path followed by the cilium is constant for each cycle by then, so no transient effects are observed anymore. The channel width is taken 1 mm, yielding a square channel cross-section. In addition to the flow rate the efficiency was computed by taking the ratio of the net flow over the total amount of fluid which was moved (so both forward and backward). For the studied actuation parameters the results are given in Figure 7.6.

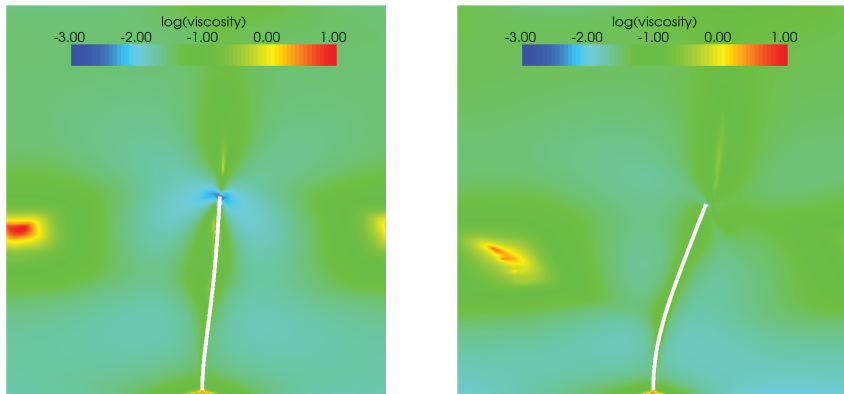


Figure 7.5: The decadic logarithm of the viscosity at the beginning of forward stroke of the 11th cycle (left) and at the beginning of the backward stroke of the same cycle (right) for a generalized Newtonian fluid.

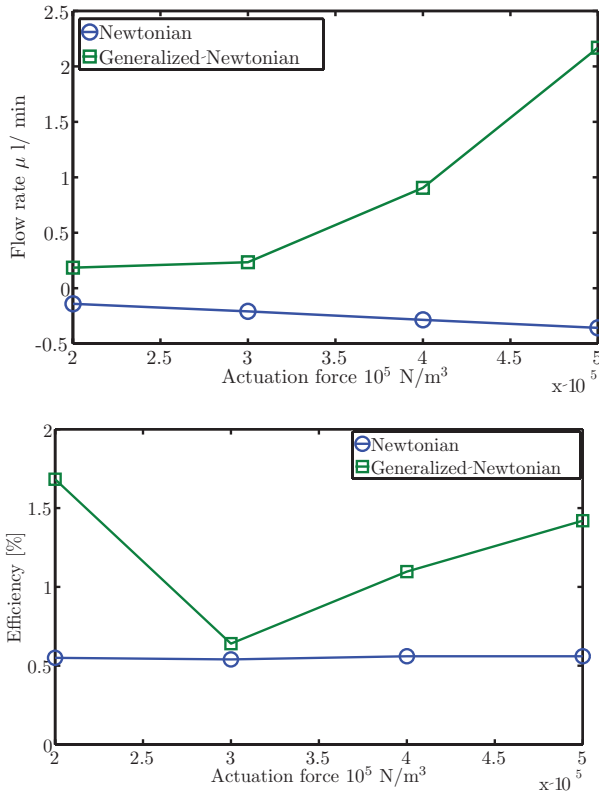


Figure 7.6: The flow rate and the efficiency for different actuation forces for a Newtonian and generalized Newtonian fluid.

Flow is generated in all cases, but the flow of a shear-thinning fluid is positive while the flow of a Newtonian fluid is negative. So the flow direction depends on the fluids constitutive relation. The efficiency is low in both cases, but for the Newtonian fluid it is about constant at 0.55%, while for the shear-thinning fluid it increases. The reason for the high efficiency at the lowest actuation force is not known.

7.2 Conclusions

The motion of a single cilium in a periodic array has been modeled, both within a Newtonian and a shear-thinning fluid. A scaling analysis showed that the characteristic displacements, velocities and time-scales of the system are determined by the solid modulus, cilium length, fluid viscosity and applied force only. Hence for a system with a given geometry and modulus, the applied

force is the only control parameter. The dynamical response of the cilium to the applied force is determined by the ratio of the characteristic time-scale of the system itself to the time-scale of applying the load both for Newtonian and shear-thinning fluids. Hence, applying different forces and loading rates during the forward and the backward stroke can lead to asymmetric motion of the cilium resulting in a net induced flow. This effect can be much larger for shear-thinning fluids, and non-Newtonian fluids in general, than for Newtonian fluids due to the shear-rate dependency of viscosity of the former, causing a different viscosity and hence different characteristic time scale between the two strokes. We found that, for a particular design of the system, this difference in dynamical behavior led to higher flow rates in opposite direction and higher efficiencies for saliva than for a Newtonian liquid with the same actuation and comparable cilia deflection.

Chapter 8

Conclusions and recommendations

In this thesis fluid propulsion by artificial cilia was studied. In Chapter 2, a model of cilia driven flow was developed and all the necessary tools for studying this flow were introduced. After performing a dimension analysis, a characteristic time-scale was found in this fluid-structure interaction problem, even when inertial effects in the fluid and solid were absent. The time-scale scales with the viscosity over the cilium stiffness. This means that the motion of and flow generated by cilia is inherently time-dependent. In Chapter 3, the flow in an electrostatically actuated micro-mixer was studied with the model developed in the previous chapter. It was shown that fluid inertia plays important roles in this micro-mixer. It changed the flow direction, with respect to a fluid having no inertia, and it improved the mixing performance. It is important to note however that the model used, was not very accurate near the moving cilia. This problem was addressed in Chapter 4, where two causes for this inaccuracy were exposed. The first cause was the fictitious domain method. In this method a fictitious fluid body is included in the equations of motion. This was solved by using the eXtended Finite Element Method (XFEM), where the equations of motion are applied on the actual domains only. The second problem was imposing the kinematic interface condition at the cilium-fluid interface. This condition couples the fluid velocity to the solid velocity. Previously this condition was enforced via a constraint on the fluid and solid velocity via a Lagrange multiplier. The stability of systems being constrained with Lagrange multipliers strongly depends on the discretization of the Lagrange multiplier, the fluid and solid. For systems with moving interfaces it is often difficult to find a stable combination. This problem was solved by introducing an adaptation of a recently developed method of imposing Dirichlet conditions in a weak manner. This method was shown to be stable, accurate and showed optimal

convergence rates. Only one additional parameter was introduced, which is equal to the viscosity in the Newtonian case and chosen equal to the polymer viscosity in the non-Newtonian case. The model developed in Chapter 4 was used for simulating cilia driven flow of a Newtonian fluid in Chapter 5. First it was shown that these systems indeed have a time-scale which governs the motion of the cilium. Since the system is time-dependent, the influence the actuation frequency on the transport and mixing performance was investigated. It was shown that the transport performance changes strongly with the actuation frequency. Both at low and high actuation frequencies the flow-rate was low, indicating an optimal operational frequency, which was indeed found. A phase delay between individual cilia aids mixing, [9]. Since the motion of a cilium depends on the time-scale of the system and the actuation frequency, changing the time-scale could lead to improved mixing. Hence the stiffness of one of two cilia was changed by changing the modulus and the cilium thickness. For mixing analysis a blob of material was tracked for several periods and the length was recorded. It was found that increasing the thickness of the cilium had larger effects on the mixing performance than increasing the modulus. Exponential length increase, which indicates good mixing, seemed to be present, although the amount of periods was too low to confirm this. The rheological properties of saliva were measured, and it was shown that human whole saliva has a high zero-shear rate viscosity of 70 Pa s, shows pronounced shear-thinning since the viscosity scales with $\dot{\gamma}^{-0.8}$. Additionally a model for studying viscoelastic fluid-structure interaction was developed and tested in Chapter 6. In order to perform simulations within a realistic time-frame, a local mesh refinement technique was developed in the same chapter. This scheme was shown to be stable in a Couette flow of an Oldroyd-B fluid, which was initially disturbed. In the final Chapter 7, the influence of rheology on the motion and flow generated by cilia was investigated. For a generalized Newtonian fluid, the influence of the applied force magnitude on the flow-rate was investigated, and compared to a Newtonian fluid. It was observed that the flow-rate shows a linear dependence on the actuation force for the Newtonian case, while the behavior is non-linear for the generalized Newtonian case. This indicates that slight variations in the actuation force large differences in flow-rate are expected for generalized Newtonian fluids.

8.1 Recommendations

In this thesis an accurate numerical model of fluid propulsion by artificial cilia was developed. The model incorporates fluid-structure interaction, with Newtonian or non-Newtonian fluids and local mesh adaptation. This numerical tool can also be used for the simulation of other fluid-structure interaction problems, such flow of fluids containing vesicles, rigid and non-rigid particles. One of the most interesting problems in this respect is accurately modeling

the deformation of cells in narrow channels, where large deformations of the cell membrane are expected. Other possible applications are the modeling of production processes which involve moving boundaries and contain two phases, complex fluids, suspensions or combinations of these aspects.

In this thesis only a small portion of all the possible problems arising in ciliar flow have been addressed. An interesting problem from a physical point of view is proving that ciliar motion can become chaotic when the problem becomes highly non-linear. This would have the direct result that the flow is also chaotic, opening up the road for efficient mixers. Since chaotic systems are sensitive to initial disturbances, a practical question is how much the motion of a cilium depends on the initial direction of the actuation force. If this is sensitive it could well be that it becomes hard to compare experimental data with simulations and getting reproducible experimental results.

Bibliography

- [1] J.M.J. den Toonder, F.M. Bos, D.J. Broer, L. Filippini, M. Gillies, J. de Goede, G.N. Mol, W. Talen, J.T.A. Wilderbeek, V. Khatavkar, and P.D. Anderson. Artificial cilia for active micro-fluidic mixing. *Lab Chip*, 8:533–541, 2008.
- [2] A.R. Shields, L. Fiser, B.A. Evans, M.R. Falvo, S. Washburn, and R. Superfine. Biomimetic cilia arrays generate simultaneous pumping and mixing regimes. *PNAS*, 107:15670–15675.
- [3] S.N. Khaderi, C.B. Craus, J. Hussong, N. Schorr, J. Belardi, J. Westerweel, O. Prucker, J. Rhe, J.M.J. den Toonder, and P.R. Onck. Magnetically-actuated artificial cilia for microfluidic propulsion. *Lab Chip*, 11:000–000, 2011.
- [4] J. Hussong, N. Schorr, J. Belardi, O. Prucker, J. Rhe, and J. Westerweel. Experimental investigation of the flow induced by artificial cilia. *Lab Chip*, 11:2017, 2011.
- [5] J. Belardi, N. Schorr, O. Prucker, and J. Rhe. Artificial cilia: Generation of magnetic actuators in microfluidic systems. *Advanced Functional Materials*, 21:3314–3320, 2011.
- [6] A. Alexeev, J.M. Yeomans, and A.C. Balazs. Designing synthetic, pumping cilia that switch the flow direction in microchannels. *Langmuir*, 24:1844–1847, 2008.
- [7] B.A. Evans, A.R. Shields, R. Lloyd Carroll, S. Washburn, M.R. Falvo, and R. Superfine. Magnetically actuated nanorod arrays as biomimetic cilia. *Nanoletters*, 7:1428–1434, 2007.
- [8] F. Fahrni, M.W.J. Prins, and L.J. IJzendoorn. Micro-fluidics actuation using magnetic artificial cilia. *Lab Chip*, 9:3413–3421.

- [9] V. Khatavkar, P.D. Anderson, and H.E.H. Meijer. Active micromixer based on artificial cilia. *Phys. Fluids*, 19:083605, 2007.
- [10] C.H. Ahn, J.W. Choi, G. Beaucage, J.H. Nevin, J.B. Lee, A. Puntambekar, and J.Y. Lee. Disposable smart lab on a chip for point-of-care clinical diagnostics. *Proc. IEEE*, 92:154–173, 2004.
- [11] D. Hun, B.D. Matthews, A. Mammoto, M. Montoya-Zavala, H.Y. Hsin, and D.E. Ingber. Reconstituting organ-level lung functions on a chip. *Science*, 328:1662–1668, 2010.
- [12] H.A. Stone, A.D. Stroock, and A. Ajdari. Engineering flows in small devices: Microfluidics toward a lab-on-a-chip. *Annu. Rev. Fluid Mech.*, 36:381–411, 2004.
- [13] H.E.H. Meijer, M.K. Singh, T.G. Kang, J.M.J. den Toonder, and P.D. Anderson. Passive and active mixing in microfluidic devices. *Macromol. Symp.*, 279(1):201–209, 2009.
- [14] J.M. Ottino and S. Wiggins. Introduction: mixing in microfluidics. *Phil. Trans. R. Soc. Lond. A*, 362:923–935, 2004.
- [15] S.Y. Teh, R. Lin, L.H. Hung, and A.P. Lee. Droplet microfluidics. *Lab Chip*, 8:198–220, 2008.
- [16] Y. Gambin, C. Simonnet, V. VanDelinder, A. Deniz, and A. Groisman. Ultrafast microfluidic mixer with three-dimensional flow focusing for studies of biochemical kinetics. *Lab Chip*, 10:598–609, 2009.
- [17] Z. Wu and N.T. Nguyen. Rapid mixing using two-phase hydraulic focusing in microchannels. *Biomedical Microdevices*, 7:13–20, 2005.
- [18] T.J. Johnson, D. Ross, and L.E. Lacascio. Rapid microfluidic mixing. *Analytical Chemistry*, 74:45–51, 2002.
- [19] A.D. Stroock, S.K.W. Dertinger, A. Ajdari, I. Mezić, H.A. Stone, and G.M. Whitesides. Chaotic Mixer for Microchannels. *Science*, 295:647–651, 2002.
- [20] T.H. Kwon, D.S. Kim, S.W. Lee and S.S. Lee. A barrier embedded chaotic micromixer. *J. Micromech. Microeng.*, 14:798–805, 2004.
- [21] Thomas Frommelt, Marcin Kostur, Melanie Wenzel-Schäfer, Peter Talkner, Peter Hänggi, and Achim Wixforth. Microfluidic mixing via acoustically driven chaotic advection. *Phys. Rev. Lett.*, 100:034502, Jan 2008.

- [22] M.A. Unger and H.P. Chou and T. Thorsen and A. Scherer and S.R. Quake. Monolithic microfabricated valves and pumps by multilayer soft lithography. *Science*, 288:113–116, 2000.
- [23] M. Vilfan, A. Potocnik, B. Kavcic, N. Osterman, I. Poberay, A. Vilfan, and D. Babic. Self assembled artificial cilia. *PNAS*, 107:12102–12106.
- [24] E.M. Gauger, M.T. Downton, and H. Stark. Fluid transport at low Reynolds number with magnetically actuated artificial cilia. *Eur. Phys. J. E*, 28:231–242, 2009.
- [25] C.L. van Oosten, C.W.M. Bastiaansen, and D.J. Broer. Printed artificial cilia from liquid-crystal network actuators modularly driven by light. *Nature Materials*, 8:677–682, 2009.
- [26] T. Sanchez, D. Welch, D. Nicastro, and Z. Dogic. Cilia-like beating of active microtubule bundles. *Science*, 333:456–459, 2011.
- [27] K. Oh, J.H. Chung, S. Devasia, and J.J. Riley. Bio-mimetic silicone cilia for microfluidic manipulation. *Lab Chip*, 9:1561–1566, 2009.
- [28] R. van Loon, P.D. Anderson, J. de Hart, and F.P.T. Baaijens. A combined fictitious domain/adaptive meshing method for fluid-structure interaction in heart valves. *Int. J. Numer. Meth. Fluids*, 46:533–544, 2004.
- [29] G. Guidoboni, R. Glowinski, N. Cavallini, S. Canic, and S. Lapin. A kinematically coupled time-splitting scheme for fluid-structure interaction in blood flow. *Applied Mathematics Letters*, 22:684–688, 2009.
- [30] J. Janela, A. Moura, and A. Sequeria. A 3d non-newtonian fluid-structure interaction model for blood flow in arteries. *J. Comp. App. Math.*, 234:2783–2791, 2010.
- [31] H.H. Hu, N.A. Patankar, and M.Y. Zhu. Direct numerical simulations of fluid-solid systems using the arbitrary Lagrangian-Eulerian technique. 169:427–462, 2001.
- [32] C. Michler, E.H. van Brummelen, and R. de Borst. An interface Newton-Krylov solver for fluid-structure interaction. *Int. J. Numer. Meth. Fluids*, 47:1189–1195, 2005.
- [33] F.P.T. Baaijens. A fictitious domain/mortar element method for fluid-structure interaction. *Int. J. Numer. Meth. Fluids*, 35:743–761, 2001.
- [34] U.M. Mayer, A. Popp, A. Gerstenberger, and W.A. Wall. 3D fluid-structure-contact interaction based on a combined XFEM FSI and dual mortar approach. *Computational Mechanics*, 46:53–67, 2010.

- [35] A. Gerstenberger and W.A. Wall. An extended finite element method/lagrange multiplier based approach for fluid-structure interaction. *Comp. Meth. Appl. Mech. Eng.*, 197:1699–1714, 2008.
- [36] S.N. Khaderi, M.G.H.M. Baltussen, P.D. Anderson, D. Ioan, J.M.J. den Toonder, and P.R. Onck. Nature inspired microfluidic propulsion using magnetic actuation. *Phys. Review E*, 79:046304, 2009.
- [37] S.N. Khaderi, M.G.H.M. Baltussen, P.D. Anderson, J.M.J. den Toonder, and P.R. Onck. Breaking of symmetry in microfluidic propulsion driven by artificial cilia. *Phys. Review E*, 82:027320, 2010.
- [38] A. Sarhangi Fard, M.A. Hulsen, N.M. Famili, H.E.H. Meijer, and P.D. Anderson. Adaptive non-conformal mesh refinement and extended finite element method for viscous flow inside complex moving geometries. *Int. J. Numer. Meth. Fluids*, accep:–, 2012.
- [39] A. Gerstenberger and W.A. Wall. An embedded Dirichlet formulation for 3D continua. *Int. J. Numer. Meth. Engng.*, 82:537–563, 2010.
- [40] N. Moës, E. Béchet, and M. Tourbier. Imposing Dirichlet boundary conditions in the extended finite element method. *Int. J. Numer. Meth. Engng.*, 67:1641–1669, 2006.
- [41] J. Dolbow and I. Harari. An efficient finite element method for embedded interface problems. *Int. J. Numer. Meth. Engng.*, 78:229–252, 2009.
- [42] M.K. Singh, P.D. Anderson, and H.E.H. Meijer. Understanding and Optimizing the SMX mixer. *Macromolecular Rapid Communications*, 30:362–376, 2009.
- [43] M. Milas and M. Rinaudo. Properties of xanthan gum in aqueous solutions: role of the conformational transition. *Carbohydrate Research*, 158:191–204, 1986.
- [44] J.A. Han and S.T. Lim. Structural changes in corn starches during alkaline dissolution by vortexing. *Carbohydrate Polymers*, 55:193–199, 2004.
- [45] N. Kikuchi and J.T. Oden. *Contact problems in elasticity: a study of variational inequalities and finite element methods*. SIAM, Philadelphia, 8th edition, 1988.
- [46] L.D. Landau, E.M. Lifschitz, and L.P. Pitaevskii. *Electrodynamics of Continuous Media*. Butterworth Heinemann, Oxford, 1984.
- [47] P. Danckwerts. The definition and measurement of some characteristics of mixtures. *Applied Scientific Research*, 3:279–296, 1952.

- [48] C.E. Shannon. A Mathematical Theory of Communication. *Bell Sys. Tech. J.*, 27:379–423,623–656, 1948.
- [49] M. Baltussen, P. Anderson, F. Bos, and J. den Toonder. Inertial effects in a micro-mixer based on artificial cilia. *Lab Chip*, 9:2326 – 2331, 2009.
- [50] R. Glowinski, T.W. Pan, and J. Periaux. A fictitious domain method for Dirichlet problem and applications. *Comp. Meth. Appl. Mech. Eng.*, 111:283–303, 1994.
- [51] R. Glowinski, T.W. Pan, T.I. Hesla, and D.D. Joseph. A distributed Lagrange multiplier/fictitious domain method for particulate flows. *Int. J. Multiphase Flow*, 25:755–794, 1999.
- [52] W.R. Hwang, M.A. Hulsen, and H.E.H. Meijer. Direct simulation of particle suspensions in sliding bi-periodic frames. *J. Comput. Phys.*, 194(1):742–772, 2004.
- [53] J. de Hart, G.W.M. Peters, P.J.G. Schreurs, and F.P.T. Baaijens. A three-dimensional computational analysis of fluid-structure interaction in the aortic valve. *J. Biomech.*, 35(1):699–712, 2003.
- [54] I. Babuška. The finite element method with Lagrangian multipliers. *Numer. Math.*, 20:179–192, 1973.
- [55] HSL (2002). A collection of Fortran codes for large scale scientific computation. <http://www.numerical.rl.ac.uk/hsl>.
- [56] C. Xi, D.L. Marks, D.S. Parikh, L. Raskin, and A. Boppart. Structural and functional imaging of 3D microfluidic mixers using optical coherence tomography. *PNAS*, 101:7516–7521, 2004.
- [57] Y.C. Ahn, W. Jung, and Z. Chen. Optical sectioning for microfluidics: secondary flow and mixing in a meandering microchannel. *Lab Chip*, 8:125–133, 2008.
- [58] G.K. Batchelor. *An Introduction to Fluid Mechanics*. Cambridge University Press, Cambridge, 1967.
- [59] S. Childress and R. Dudley. Transition from ciliary to flapping mode in a swimming mollusc: flapping flight as a bifurcation in Re_ω . *J. Fluid Mech.*, 498:257–288, 2004.
- [60] J.G. Franjione, C. Leong, and J.M. Ottino. Symmetries withing chaos: A route to effective mixing. *Phys. Fluids A*, 1(11):1772–1783, 1989.
- [61] M.G.H.M. Baltussen, Y.J. Choi, M.A. Hulsen, and P.D. Anderson. Weakly-imposed Dirichlet boundary conditions for non-Newtonian fluid flow. *J. Non-Newtonian Fluid Mech.*, 166(17-18):993–1003, 2011.

- [62] Y.J. Choi, M.A. Hulsen, and H.E.H. Meijer. An extended finite element method for the simulation of particulate viscoelastic flows. *J. Non-Newtonian Fluid Mech.*, 165:607–624, 2010.
- [63] M. Heath. *Scientific computing: an introductory survey*. McGraw-Hill, New York, 2nd edition, 2002.
- [64] L. Zhang, T. Cui, and H. Liu. A set of symmetric quadrature rules on triangles and tetrahedra. *J. Computational Mathematics*, 27:89–96, 2009.
- [65] J. Nitsche. Über ein Variationsprinzip zur Lösung von Dirichlet-Problemen bei Verwendung von Teilräumen, die keinen Randbedingungen unterworfen sind. *Abhandlungen aus dem Mathematischen Seminar der Universität Hamburg*, 36:9–15, 1971.
- [66] J. Dolbow, A. Embar, and I. Harari. Imposing Dirichlet boundary conditions with Nitsche’s method and spline-based finite elements. *Int. J. Numer. Meth. Engng.*, 83:877–898, 2010.
- [67] A. Zillian and H. Netuzhylov. Hybridized enriched space-time finite element method for analysis of thin-walled structures immersed in generalized Newtonian fluids. *Computers and Structures*, 88:1265–1277, 2010.
- [68] P. Causin, J.G. Gerbeau, and F. Nobile. Added-mass effect in the design of partitioned algorithms for fluid-structure problems. *Comp. Meth. Appl. Mech. Eng.*, 194:4506–4527, 2005.
- [69] M. von Scheven and E. Ramm. Strong coupling schemes for interaction of thin-walled structures and incompressible flows. *Int. J. Numer. Meth. Engng.*, 87:214–231, 2011.
- [70] H.G. Schuster and W. Just. *Deterministic Chaos*. Wiley-VCH, Weinheim, 4th edition, 1984.
- [71] J.R. Stokes and G.A. Davies. Viscoelasticity of human whole saliva collected after acid and mechanical stimulation. *Biorheology*, 44:141–160, 2007.
- [72] M.D. Kaplan and B.J. Baum. The functions of saliva. *Dysphagia*, 8:225–229, 1993.
- [73] J.R. Stokes and G.A. Davies. Viscoelasticity of human whole saliva collected after acid and mechanical stimulation. *Biorheology*, 44:141–160.
- [74] A.N. Brooks and T.J.R. Hughes. Streamline upwind/Petrov-Galerkin formulations for convection dominated flows with particular emphasis on the incompressible Navier-Stokes equations. *Comp. Meth. Appl. Mech. Eng.*, 32:199–259, 1982.

- [75] R. Guénette and M. Fortin. A new mixed finite element method for computing viscoelastic flows. *J. Non-Newtonian Fluid Mech.*, 60:27–52, 1995.
- [76] F.P.T. Baaijens, M.A. Hulsen, and P.D. Anderson. *The use of mixed finite elements for viscoelastic fluid flow analysis*. John Wiley, New York, 2004. in Encyclopedia of Computational Mechanics.
- [77] R. Kupferman. On the linear stability of plane Couette flow for an Oldroyd-B fluid and its numerical approximation. *J. Non-Newtonian Fluid Mech.*, 127:169–190, 2005.
- [78] V.A. Gorodtsov and A.I. Leonov. On a linear instability of a plane parallel Couette flow of a viscoelastic fluid. *J. Appl. Math. Mech.*, 31:310–319, 1967.
- [79] D.J. Smith, E.A. Gaffney, and J.R. Blake. Mathematical modeling of cilia-driven transport of biological fluids. *Proc. R. Soc. A.*, 465:2417–2439, 2009.
- [80] C.W. Gear. *Numerical Initial Value Problems in Ordinary Differential Equations*. Prentice-Hall, Englewood Cliffs, N.J., 1971.
- [81] G. D’Avino and M.A. Hulsen. Decoupled second-order transient schemes for the flow of viscoelastic fluids without a solvent contribution. *J. Non-Newtonian Fluid Mech.*, 165:1602–1612, 2010.
- [82] M.G.H.M. Baltussen, M.A. Hulsen, P.D. Anderson, and J.M.J. den Toonder. Fluid-structure interaction of viscoelastic fluids. 2012. in preparation.
- [83] M.G.H.M. Baltussen, M.A. Hulsen, P.D. Anderson, and J.M.J. den Toonder. Time dependent effects in flows generated by artificial cilia. 2012. in preparation.
- [84] M.G.H.M. Baltussen, M.A. Hulsen, P.D. Anderson, and J.M.J. den Toonder. A local mesh refinement technique for viscoelastic flow. 2012. in preparation.
- [85] M.G.H.M. Baltussen, M.A. Hulsen, and G.W.M. Peters. Numerical simulation of the fountain flow instability in injection molding. *J. Non-Newtonian Fluid Mech.*, 165:631–640, 2010.
- [86] M.G.H.M. Baltussen, W.M.H. Verbeeten, A.C.B. Bogaerds, M.A. Hulsen, and G.W.M. Peters. Anisotropy parameter restrictions for the eXtended Pom-Pom model. *J. Non-Newtonian Fluid Mech.*, 165:1047–1055, 2010.

Appendix A

Time integration and linearization

The set of governing equations (2.1-2.12) is both time dependent and non-linear. By applying a time stepping procedure for all time dependent equations and linearizing all non-linear terms, a set of linear equations can be solved for each individual time step. First the time dependent terms will be treated, followed by the non-linear terms.

A.1 Time integration

All time dependent terms are either solved with first order implicit Euler scheme, which for

$$\frac{\partial a}{\partial t} + f(a) = 0$$

reads:

$$\frac{\partial a}{\partial t} + f(a) = \frac{a^{i+1} - a^i}{\Delta t} + f(a^{i+1}) + \mathcal{O}(\Delta t), \quad (\text{A.1})$$

where the subscripts $i + 1$ and i indicate the value at the $i + 1$ -th and i -th time step and Δt is the time step. This method is first order accurate and is unconditionally stable for all time steps if $\text{Re}(\frac{\partial f}{\partial a^{i+1}}) > 0$. When higher accuracy is required we choose to use a second order Gear method [80], which requires evaluation of $f(a)$ only at the current time step $i + 1$:

$$\frac{\partial a}{\partial t} + f(a) = \frac{3a^{i+1} - 4a^i + a^{i-1}}{2\Delta t} + f(a^{i+1}) + \mathcal{O}(\Delta t^2). \quad (\text{A.2})$$

This method is also unconditionally stable, for the same condition as mentioned above.

If a variable at time $i + 1$ is required (for instance in the implicit treatment of the viscoelastic stress) implicit Euler is used, yielding:

$$a^{j+1} = a^j + f(a^{j+1})\Delta t + \mathcal{O}(\Delta t^2), \quad (\text{A.3})$$

which is second-order accurate. So even when the time derivatives of a are treated with (A.2), it's update can be taken with (A.3), without losing the accuracy [81].

A.2 Linearization

The fluid-structure interaction problems presented in this thesis requires an iterative solution approach, since the interface position changes in time. No

Several terms in the governing equations of motion are non-linear, more specifically they are quadratic. Since For the linearization of these terms we use a Newton-Raphson scheme, which is second-order convergent. For this the following approximation of ab is used:

$$ab = (a_j + \delta a)(b_j + \delta b) = a_j b_j + a_j \delta b + \delta a_j b_j + \delta a \delta b \quad (\text{A.4})$$

$$a_{j+1} b_j + a_j b_{j+1} - a_j b_j + \delta a \delta b, \quad (\text{A.5})$$

where j indicates the previous iterative step and $j + 1$ the current one, $\langle \rangle_{j+1} = \langle \rangle_j + \delta \langle \rangle$.

Where non-linear terms occur in governing equations of the solid, which has a Lagrangian basis, the appropriate reference frame has to be chosen. Here we use the total Lagrange approach, where all deformations are related to the original configuration.

Appendix B

Intersecting and Delaunay triangulation

The eXtended Finite Element Method presented in this thesis requires the subdivision of fluid elements in a part which belongs to the fluid domain and a part which doesn't. Splitting the domain into two parts consists of two steps, first the intersection of the boundary of the solid with the edges of the fluid element is found and second the intersection points and the nodes of the fluid element are used as input for a Delaunay triangulation. Both steps, and their practical implementation, are discussed in this appendix.

B.1 Intersecting

The intersection points between Γ_{fs} and all edges of the fluid elements are found by starting at the first element of Γ_{fs} and checking if it intersects with any of the edges of the fluid element which contains the first node of the first element. If an intersection is found, the search for intersections is continued in the adjacent fluid element. If no intersection is found, the search is continued with the next element of Γ_{fs} . Both the elements on Γ_{fs} , which are solid element edges, and the edges of the fluid element are parameterized by the shape functions of the elements. In the Finite Element Method, the shape functions are polynomials and the elements are isoparametrically mapped to a reference element. Hence the position \mathbf{x} of a local coordinate (ξ_1, η_1) is given by:

$$\mathbf{x} = \sum_{i=1}^N \phi_i(\xi_1, \eta_1) \mathbf{x}_i, \quad (\text{B.1})$$

where ϕ_i are the shape functions of the element. At an intersection the coordinate along the solid element edge \mathbf{x}_s is equal to the coordinate at the fluid

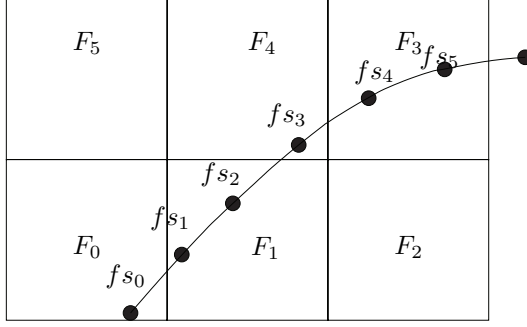


Figure B.1: The method for finding intersections of interface elements f_{s_0-5} with the edges of the fluid elements F_{0-5} . The search starts in f_{s_0} , and the intersection with edge 2 of F_0 is found, and the search for intersections of f_{s_0} with F_1 continues. Since no other intersections of s_0 with F_1 are found, the search continues with f_{s_1} , which has no intersections with F_1 too, so intersections between f_{s_2} and F_1 are sought. This intersection is found and the search continues in F_4 etc..

element \mathbf{x}_f :

$$\mathbf{x}_s - \mathbf{x}_f = \sum_{i=1}^{N_s} \phi_{i,s}(\xi_{\text{int},s}, \eta_{\text{int},s}) \mathbf{x}_{i,s} - \sum_{j=1}^{N_f} \phi_{j,f}(\xi_{\text{int},f}, \eta_{\text{int},f}) \mathbf{x}_{j,f} = \mathbf{0}, \quad (\text{B.2})$$

where $(\xi_{\text{int},s}, \eta_{\text{int},s})$ are the local coordinates of the intersection point at the solid edge and $\xi_{\text{int},f}, \eta_{\text{int},f}$ the local coordinates of the intersection point at the fluid edge. At an element edge either ξ or η is $-1, 1$. Hence Eq. (B.2) reduces to a two equations, one for each spatial dimension of \mathbf{x} , and two unknowns ($(\xi_{\text{int},s}$ or $\eta_{\text{int},s})$ and $(\xi_{\text{int},f}$ or $\eta_{\text{int},f})$). This system can be solved if an intersection exists. The existence of a solution depends on the order of the polynomial and can be determined before computation of the intersection point takes place. If both the shape functions of the fluid and solid are linear, or if both are quadratic and one is not curved, Eq. (B.2) can be solved analytically. In all other cases the resulting system has to be linearized and solved numerically. By solving Eq. (B.2) all intersection points are found, even if they lay outside the reference domain $[-1, 1]$. Hence only intersection points within the reference domain are treated as true intersection points. By following all solid elements along Γ_{fs} , it stays continuous and problems with holes are avoided, which makes this method robust. By using the shape functions of the elements, the method is general. Practical limits due to the linearization of the final equation will probably limit its use to lower order polynomials however, which is fine since we only use Q_2 elements for fluid and solid.

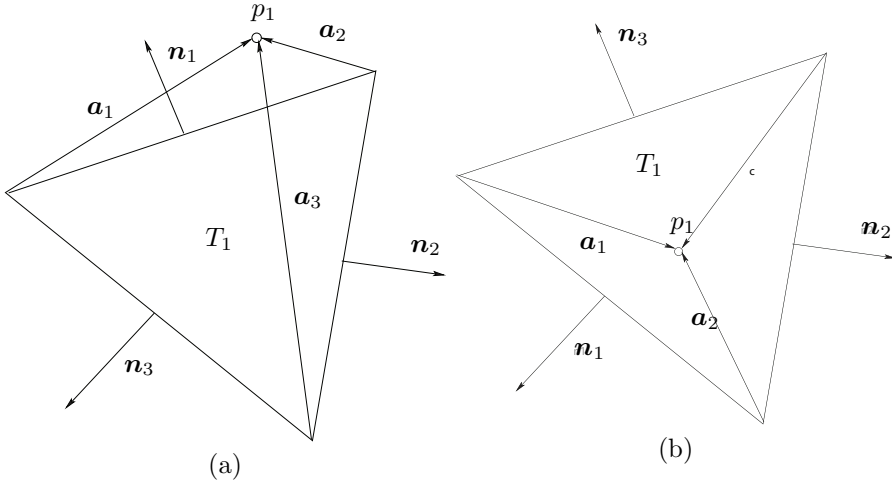


Figure B.2: In Figure (a) not all inner products $\mathbf{n}_i \cdot \mathbf{a}_i$ are negative, hence p_1 lies outside T_1 . In Figure (b), all inner products $\mathbf{n}_i \cdot \mathbf{a}_i$ are negative, which means p_1 lies inside T_1 .

B.2 Delaunay triangulation

All nodes of an intersected fluid element and the intersection points are input for a Delaunay triangulation. A Delaunay triangulation consists of two steps:

- Adding points to the triangulation.
- Making all triangles locally Delaunay.

The first step is performed in the following way:

- Two triangular elements are created from the all nodes of the fluid element except the center node.
- The remaining intersection points are added one by one. At each addition the residing element is determined and this element is subdivided into three new elements.

Point p_1 is residing in triangle T_1 if each inner product of the normal of edge e_i with the vector \mathbf{a}_i connecting p_1 with the starting point of e_i is negative, as shown in Figure B.2.

Appendix C

Weakly-imposed Dirichlet boundary conditions for the Poisson equation

The Poisson equation on the domain Ω with the respective Dirichlet and Neumann boundary conditions is:

$$\nabla^2 \mathbf{d} = \mathbf{0} \quad \text{in } \Omega, \quad (\text{C.1})$$

$$\mathbf{n} \cdot \nabla \mathbf{d} = \mathbf{t}_N \quad \text{on } \Gamma_N, \quad (\text{C.2})$$

$$\mathbf{d} = \mathbf{d}_D \quad \text{on } \Gamma_D, \quad (\text{C.3})$$

where \mathbf{t}_N is the flux on the Neumann boundary and \mathbf{d}_D the value for the displacement on the Dirichlet boundary. By multiplying with test-function \mathbf{w} , applying partial integration, and substitution of the Neumann boundary condition, the weak form of Eq. (C.1) reads:

$$(\nabla \mathbf{w}^T, \nabla \mathbf{d})_\Omega - (\mathbf{w}, \mathbf{t}_N)_{\Gamma_N} - (\mathbf{w}, \mathbf{n} \cdot \nabla \mathbf{d})_{\Gamma_D} = 0. \quad (\text{C.4})$$

The Dirichlet boundary condition is imposed in a weak manner by introducing the projection of $\mathbf{E} - \nabla \mathbf{d}$ as an extra equation to the system and after partial integration the weak form of this additional equation reads:

$$(\mathbf{H}, \mathbf{E})_\Omega + (\mathbf{n} \cdot \mathbf{H}, \mathbf{d})_{\Gamma_N} + (\mathbf{n} \cdot \mathbf{H}, \mathbf{d})_{\Gamma_D} = 0. \quad (\text{C.5})$$

By adding and subtracting the last term it reads:

$$(\mathbf{H}, \mathbf{E})_\Omega + (\mathbf{n} \cdot \mathbf{H}, \mathbf{d})_{\Gamma_N} + (\mathbf{n} \cdot \mathbf{H}, \mathbf{d})_{\Gamma_D} + (\mathbf{n} \cdot \mathbf{H}, \mathbf{d})_{\Gamma_D} - (\mathbf{n} \cdot \mathbf{H}, \mathbf{d})_{\Gamma_D} = 0, \quad (\text{C.6})$$

where the Dirichlet boundary condition can be filled in into the last term:

$$(\mathbf{H}, \mathbf{E})_{\Omega} + (\mathbf{n} \cdot \mathbf{H}, \mathbf{d})_{\Gamma_N} + (\mathbf{n} \cdot \mathbf{H}, \mathbf{d})_{\Gamma_D} + (\mathbf{n} \cdot \mathbf{H}, \mathbf{d})_{\Gamma_D} - (\mathbf{n} \cdot \mathbf{H}, \mathbf{d}_D)_{\Gamma_D} = 0. \quad (\text{C.7})$$

After partially integrating back, the final equation for \mathbf{E} reads:

$$(\mathbf{H}, \mathbf{E})_{\Omega} + (\mathbf{n} \cdot \mathbf{H}, \mathbf{d} - \mathbf{d}_D)_{\Gamma_D} = 0. \quad (\text{C.8})$$

In Eq. (C.4), $\nabla \mathbf{d}$ in the Dirichlet boundary term is replaced by \mathbf{E} by adding $(\mathbf{w}, \mathbf{n} \cdot (\nabla \mathbf{v} - \mathbf{E}))_{\Gamma_D}$ to the system. The final set of equations then reads:

$$\begin{aligned} & (\nabla \mathbf{w}^T, \nabla \mathbf{d})_{\Omega} - (\mathbf{w}, \mathbf{t}_N)_{\Gamma_N} - \\ & (\mathbf{w}, \mathbf{n} \cdot \nabla \mathbf{d})_{\Gamma_D} + (\mathbf{w}, \mathbf{n} \cdot (\nabla \mathbf{d} - \mathbf{E}))_{\Gamma_D} = 0, \\ & (\mathbf{H}, \mathbf{E})_{\Omega} + (\mathbf{n} \cdot \mathbf{H}, \mathbf{d} - \mathbf{d}_D)_{\Gamma_D} = 0. \end{aligned} \quad (\text{C.9})$$

The extra variable \mathbf{E} can be eliminated from the system in a similar way as was done in Section 4.2.3.

Samenvatting

Microfluidische analyse apparaten worden steeds meer gemeengoed in de klinische analyse. Het mengen en transporteren van meerdere vloeistoffen is een veel voorkomende stap in deze apparaten. Omdat vloeistoftransport op micrometerschaal ook in de natuur belangrijk is, kunnen werkingsprincipes uit de natuur bestudeerd en gekopiëerd worden om vloeistoftransport en menging in microfluidische apparaten teweeg te brengen. Een voorbeeld van vloeistoftransport in de natuur zijn de trilhaartjes die men op verschillende micro-organismen en in de longen aantreft. Deze haartjes, cilia genaamd, gedragen zich als micro-actuatoren en verplaatsen de omliggende vloeistof. Dit resulteert in de voortbeweging van het micro-organisme, of in de stroming van de vloeistof. Omdat de cilia klein zijn, wordt de stroming gedomineerd door viskeuze effecten, hetgeen in het algemeen ook geldt voor de microfluidische apparaten. Recentelijk zijn verschillende zogenaamde artificiële cilia ontwikkeld, die allen vloeistoffen verplaatsen [1–8].

In dit proefschrift wordt een numeriek model opgesteld en gebruikt om de werkingsprincipes die ten grondslag liggen aan deze apparaten te bestuderen en te verbeteren. Dit model beschrijft de vloeistof-vaste stof interactie van een cilium met de omringende vloeistof. Aangezien de deformaties van de cilia, die als slanke balken kunnen worden beschouwd, groot zijn, is het een vereiste dat het numerieke model deze grote deformaties ook nauwkeurig beschrijft. Er is daarom gekozen voor een model waar de vloeistof op een vast, Euleriaans, raster wordt beschreven en de vaste stof op een meebewegend, Lagrangiaans, raster. In eerste instantie is een fictitious domain/Lagrange multiplier techniek gebruikt om het vloeistof en vaste stof domein met elkaar te verbinden. Uit simulaties bleek echter dat deze methode te onnauwkeurig was, met name in de nabijheid van het cilium.

Aan deze onnauwkeurigheid liggen twee oorzaken ten grondslag, zijnde het fictieve vloeistofdomein en de discretisatie van de Lagrange multiplier. De eerste bron van onnauwkeurigheid is verholpen door het gebruik van de eX-

tended Finite Element Method (XFEM). De tweede oorzaak is verholpen door het zwak voorschrijven van de randvoorwaarden op de ciliumrand, zonder gebruik te maken van Lagrange multipliers. De combinatie van beiden, levert een nauwkeurige methode op, waarmee vloeistof-vaste stof interactie, voor Newtonse, gegeneraliseerd Newtonse en viscoelastische vloeistoffen. Deze methode heeft als voordeel dat een nauwkeurige oplossing gevonden wordt met optimale convergentie, zonder dat er probleem afhankelijke parameters geïntroduceerd dienen te worden.

Dit nieuwe numerieke model wordt in hoofdstuk 4 gebruikt om de invloed van de actuatiefrequentie op de transport- en mengeffectiviteit te bestuderen. Er wordt aangetoond dat er een optimale frequentie bestaat waarop het debiet maximaal is. Dit optimum wordt veroorzaakt door de intrinsieke tijdsafhankelijkheid van het vloeistof-vaste stof probleem, welke niet veroorzaakt wordt door massa-tragheid van het systeem. De frequentie waarbij het debiet optimaal is, is niet hetzelfde als de frequentie waarbij de hoeveelheid vloeistof verplaatst per cyclus optimaal is. Daarom is het van belang het debiet te optimaliseren en niet de hoeveelheid verplaatste vloeistof per cyclus. Het menggedrag van artificiële cilie is bestudeerd door twee cilie te nemen die een verschillende intrinsieke tijdschaal hebben en deze met een roterende kracht met gelijkblijvende amplitude en frequentie te actueren. Doordat beide cilie een andere tijdschaal hebben, bewegen zij ook anders. Dit leidt tot een faseverschil tussen beiden, hetgeen goed menggedrag tot gevolg heeft [9]. De mengeffectiviteit wordt gekwantificeerd door de vorm van een druppel, die intieel tussen de cilie geplaatst is, in de tijd te volgen. Een exponentiële toename van de omtrek wijst op chaotisch mengen. Een toename van de omtrek, al dan niet exponentieel, is gevonden in alle simulaties. Het veranderen van de dikte van een van de twee cilie heeft een duidelijk positief effect op de mengeffectiviteit. De effectiviteit wordt ook bepaald door de hoeveelheid vloeistof die verplaatst wordt per actuatiefrequentie. Bij lage actuatiefrequenties wordt er meer vloeistof verplaatst en is de menging beter dan bij hoge actuatiefrequenties waar weinig vloeistof wordt verplaatst.

Het numerieke model uit hoofdstuk 4 is aangepast in hoofdstuk 6 om de invloed van niet-Newtonse vloeistofgedrag op de stroming te onderzoeken. Tevens is een methode ontwikkeld om lokale rasterverfijning toe te passen, hetgeen nauwkeurige simulaties toelaat die minder rekentijd vergen. Zowel het viscoelastische vloeistof-vaste stof interactie probleem als de lokale rasterverfijning zijn getoetst en stabiel en nauwkeurig bevonden.

Dit numerieke model is gebruikt in hoofdstuk 7 om stroming van gegeneraliseerd Newtonse en viscoelastische vloeistofstroming geïnduceerd door artificiële cilie te bestuderen. Het debiet van een gegeneraliseerd Newtonse vloeistof laat een grotere afhankelijkheid van de actuatiekracht zien dan het debiet van een Newtonse vloeistof. Dit wordt verklaard door de aanwezigheid van een extra tijdschaal in het niet-Newtonse systeem.

In het laatste hoofdstuk worden de conclusies en aanbevelingen gegeven.

Acknowledgments

After more than four years of work on modeling artificial cilia, this thesis is finally finished. During this time, many people supported, encouraged and helped me.

As my promotor, prof. Jaap den Toonder always had a listening ear and critical remark. I am very grateful to you, Jaap, for the trust you gave me by giving me the freedom to perform my own research. Although my chaotic way of working sometimes clashed with your structured way of working, you were always able to soften the frustrations which I must have caused you. Sorry for giving you even greyer hair and thank you for being patient with me.

The next words I would like to spend on my co-promoters prof. Patrick Anderson and dr. Martien Hulsen. Patrick, I would like to thank you for the stimulating and discussions we had and challenging tasks you gave me. You gave me total freedom, but also pointed out the risks of getting stuck or working on problems of lower importance. Also thanks for inviting me to come along to visit prof. Walls group in March 2010, since this visit was of great importance to the development of the models in this thesis. All simulations in this thesis were performed with the finite element package TFEM, which is the brainchild of Martien Hulsen. So I can rightfully say that without you, Martien, this thesis would not have been there. Apart from providing a very flexible and reliable code, your critical eye always made me rethink my own views.

This work was part of the European research project “ARTIC”. I would like to thank all participants for their helpful comments and discussions, and also for the nice times we had having dinner or going to a local waterhole. I would like to thank prof. Patrick Onck and dr. Syed Khaderi, for all the nice meetings we had in Groningen and Eindhoven, I think the collaboration in work package 1 was nice and successful.

Most of the saliva rheology was measured by René Thijssen, so thank you for handling the loogies for me.

Thank you to all the other committee members, prof. Breurer, prof. Clercx, prof. Westerweel and prof. de Goey for taking place in my defense committee.

Although the topic of my thesis is related to microfluidics, I worked in the group Polymer Technology of prof. Han Meijer. I would like to thank you Han for creating a nice working atmosphere and providing me with short and outright feedback, in your (in)famous way.

A group of guys who had to cope with my bad jokes on a daily basis are “de koekebakkers”, with whom I had lunch the last couple of years. During the lunches and field trips (to Zürich for instance), we have become friends, and I hope this friendship will hold. This also holds for my former roommates and colleagues, I’ve had a nice time at the the TU/e.

For everybody who, out of interest or by mistake, reads these acknowledgments and still has to finish his or hers thesis: good luck and keep on struggling forward, you will succeed in the end.

Finally I would like to thank the support and continuous interest of my family and friends. Without your support, finishing this thesis would have been even more difficult.

Curriculum Vitae

Michiel G.H.M. Baltussen was born on the eighth of January 1983 in Tilburg, the Netherlands. He successfully completed his pre-university education at the Dendron College in Horst in 2001, and started studying Mechanical Engineering at Eindhoven University of Technology in the same year.

During his Master track in the group of professor Han E.H. Meijer at Eindhoven University of Technology, Michiel spent three months at Tokyo University, where he performed injection molding visualisation experiments under the supervision of prof. Hidetoshi Yokoi and dr. Shigeruh Hasegawa. After this internship, he completed his Master thesis “Simulation of Injection Moulding of a Viscoelastic Liquid” in 2007 (Cum Laude). During this period he was supervised by dr. Martien A. Hulsen and prof. Gerrit W.M. Peters.

Immediately after completion, he started working on a PhD project at the same university on the modelling of flow induced by artificial cilia, which was part of the ARTIC program. In ARTIC, several European universities and companies collaborate to develop a microfluidic device capable of transport and mixing based on microfluidic actuators, known as cilia. In this project he closely worked together with dr. Syed N. Khaderi and prof. Patrick R. Onck of the University of Groningen. The work performed in this project resulted in a thesis entitled “Transport and Mixing by Artificial Cilia”, under the supervision of prof. Jaap M.J. den Toonder, prof. Patrick D. Anderson and dr. Martien A. Hulsen. He will defend this thesis on January 26th 2012.

Michiel is active as a voluntary miller in Meterik on the traditional windmill “Eendracht Maakt Macht” since 1994 and passed his exam as official miller in 2002. He is also a member of a traditional fanfare band, both as a musician and as a board member, and he is also co-organizer of a biennial band contest in entertainment music (TEMA).

List of Publications

The following publications were (co)-authored by the author of this thesis within the scope of this thesis:

- M. Baltussen, P. Anderson, F. Bos, and J. den Toonder. Inertial effects in a micro-mixer based on artificial cilia. *Lab Chip*, 9:2326 – 2331, 2009
- S.N. Khaderi, M.G.H.M. Baltussen, P.D. Anderson, D. Ioan, J.M.J. den Toonder, and P.R. Onck. Nature inspired microfluidic propulsion using magnetic actuation. *Phys. Review E*, 79:046304, 2009
- S.N. Khaderi, M.G.H.M. Baltussen, P.D. Anderson, J.M.J. den Toonder, and P.R. Onck. Breaking of symmetry in microfluidic propulsion driven by artificial cilia. *Phys. Review E*, 82:027320, 2010
- M.G.H.M. Baltussen, Y.J. Choi, M.A. Hulsen, and P.D. Anderson. Weakly-imposed Dirichlet boundary conditions for non-Newtonian fluid flow. *J. Non-Newtonian Fluid Mech.*, 166(17-18):993–1003, 2011
- M.G.H.M. Baltussen, M.A. Hulsen, P.D. Anderson, and J.M.J. den Toonder. Fluid-structure interaction of viscoelastic fluids. 2012. in preparation
- M.G.H.M. Baltussen, M.A. Hulsen, P.D. Anderson, and J.M.J. den Toonder. Time dependent effects in flows generated by artificial cilia. 2012. in preparation
- M.G.H.M. Baltussen, M.A. Hulsen, P.D. Anderson, and J.M.J. den Tooder. A local mesh refinement technique for viscoelastic flow. 2012. in preparation

Additionally the following publications were written outside the scope of this thesis:

- M.G.H.M. Baltussen, M.A. Hulsen, and G.W.M. Peters. Numerical simulation of the fountain flow instability in injection molding. *J. Non-Newtonian Fluid Mech.*, 165:631–640, 2010
- M.G.H.M. Baltussen, W.M.H. Verbeeten, A.C.B. Bogaerds, M.A. Hulsen, and G.W.M. Peters. Anisotropy parameter restrictions for the eXtended Pom-Pom model. *J. Non-Newtonian Fluid Mech.*, 165:1047–1055, 2010

